Catalytic activity trends of CO oxidation – A DFT study

Jiang, Tao

Publication date:
2011

Document Version
Early version, also known as pre-print

DTU

Catalytic activity trends of CO oxidation – A DFT study

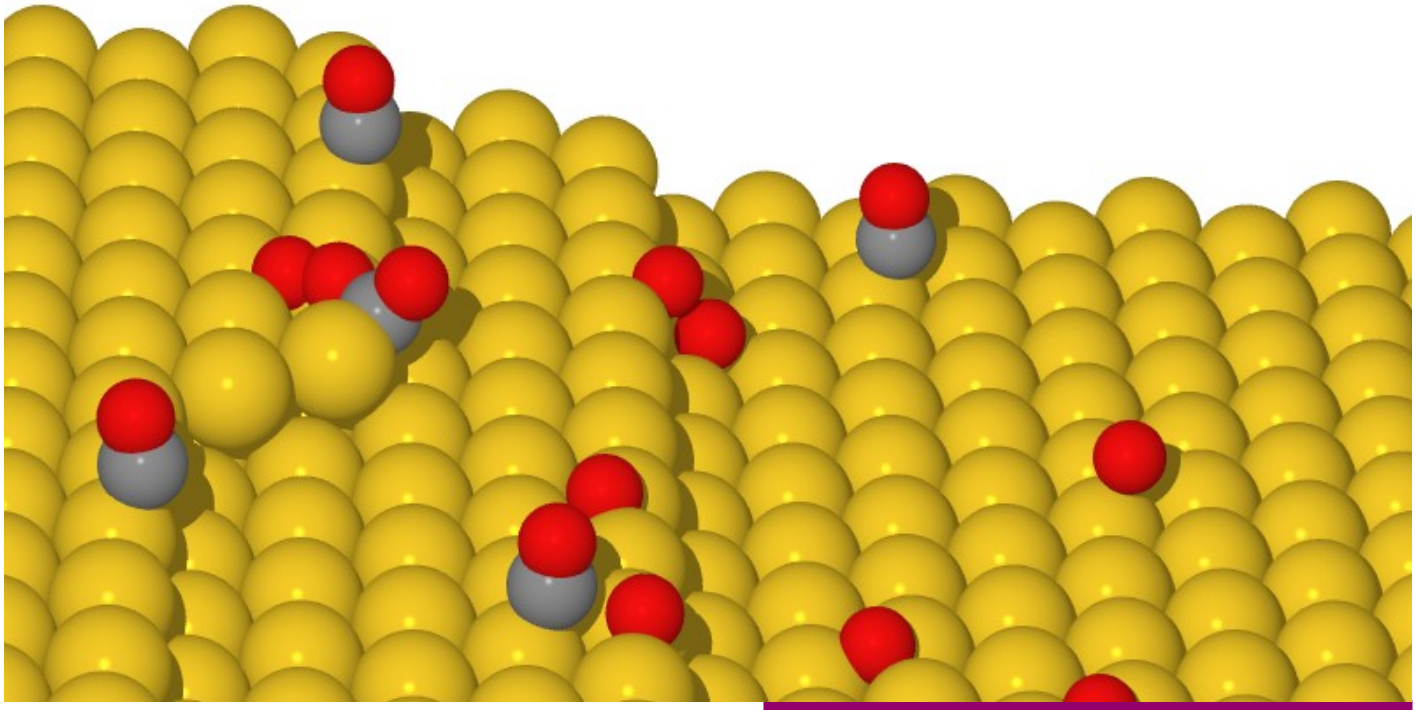

Tao Jiang

PhD thesis

CAMd
Center for Atomic-scale Materials Design

Catalytic activity trends of CO oxidation - A DFT study

Tao Jiang

Kongens Lyngby 2011

Technical University of Denmark
Center for Atomic-scale Materials Design
Building 311, DK-2800 Kongens Lyngby, Denmark
Phone +45 45253224, Fax +45 45882399
www.camd.dtu.dk

Abstract

There are two goals of this thesis, the first one is to understand the reactivity of noble metal nanoparticles for CO oxidation reaction. The second goal is to gain understanding to the second derivative (Hessian matrix) of the potential energy surfaces (PES) of adsorption systems, especially its eigenmodes and eigenvalues, and improving algorithms for geometry optimization in electronic structure calculations.

The catalytic activity of gold nanoparticles has received wide attention since the discovery of their activity on CO oxidation by Professor Haruta in 1987. By using density functional theory (DFT) and microkinetic modeling, we study CO oxidation reaction pathway on a number of transition and noble metals, i.e. Au, Ag, Pt, Pd, Cu, Ni, Rh, Ru, with different surface morphologies, close packed surfaces, stepped surfaces, kinked surfaces, as well as 12-atom corner model of a larger nanoparticle. The upper bound of the catalytic activity (Sabatier activity) is then obtained and shows that at room temperature gold nanoparticle is the best catalyst for CO oxidation among all the metals considered. Under high temperature reaction condition, however, close packed Pt surface become most catalytically active. We show also that the catalytic activity changes with the coordination number of metal atoms at the active sites. This effect is shown to be electronic in nature, since low coordinated metal atoms, which bind reactants most strongly, have the highest energy metal d states.

We compare our theoretical study of CO oxidation with experimental studies. The latter shows promoted catalytic activity when gold particle size decreases to 5 nm. Oxidizing CO by N_2O was found to involve a CO-O transition state, with atomic O adsorbed on the gold B5 sites and CO on the corners. On the other hand, CO oxidation by molecular O_2 occurs via a different reaction

pathway, which instead involves a meta-stable intermediate CO-O_2. However, although the two oxidizing agents used proceeded via different reaction pathways on different active sites, the apparent overall activation barriers obtained from both theory and experiment were found to be the same. The experiment findings are in good agreement with our theoretical calculations.

In the second part of the thesis focuses on improving the convergence property of Quasi-Newton algorithm. The eigenvalues of the Hessian matrix of 54 atoms bulk Cu model are calculated, and the sizes of eigenvalues follow power-law distribution. It is found that the anharmonicity of the weak modes lead to poor Newton step and poor Hessian update in BFGS type Quasi-Newton algorithm, which slow down the geometry optimization. Line search that fulfills Wolff conditions is then applied to improve the quality of Hessian update. We parameterized the optimizer and the parameter spaces for different test cases are scanned to find the optimum parameter set for surface adsorption type of problems. The test cases show that the BFGS algorithm with line search scheme with the optimized parameter set greatly improves the convergences of geometry optimization.

The scanning of the parameter space of the algorithm shows that the value of preconditioner around the middle of the eigenvalue spectrum gives faster convergence rate. An adaptive update method (AUM) for adjusting the preconditioners of the unupdated modes is then proposed, so that they are set to be in the middle of the eigenvalue spectrum dynamically. Test results shown that the AUM is able to adjust poorly set preconditioners in several steps and improve the convergence rate.

Finally, we use a model potential that describes bond stretiching to calculate the Hessian matrix. Comparison with the exact Hessian shows that the model Hessian reproduce the vibrational modes in a decent manner, despite its simplicity. For homogeneous systems, preconditioning the optimizer with the model Hessian reduces the condition number by 14 times and largely improves the convergence rate.

Resumé

Denne afhandling har to mål, det første er at forstå reaktiviteten af ædelmetal nanopartikler for CO oxidations reaktionen. Det andet mål er at opnå forståelse for den anden afledte (Hessian-matricen) af den potentielle energi-overflade (PES) for adsorptions-systemer, specielt dens egentilstande og egenværdier, og at forbedre algoritmer til geometri-optimering i elektronstrukur beregninger.

Den katalytiske aktivitet af guld nanopartikler har fået meget opmærksomhed siden opdagelsen af deres katalytiske aktivitet for CO oxidation af Professor Haruta i 1987. Ved hjælp af tætheds-funktional-teori (DFT) og mikrokinetisk modellering studerer vi her reaktions-vejen for CO oxidation på adskillige overgangsmetaller og ædelmetaller, dvs. Au, Ag, Pt, Pd, Cu, Ni, Rh, Ru med forskellige overflade-morfologier, tætpakkede overflader, overflader med trin og knæk, samt en 12-atoms hjørne-model af en større nanopartikel. Den øvre grænse på den katalytiske aktivitet (Sabatier-aktivitet) er fundet og den viser at ved stue-temperatur er guld nanopartiklen, udaf alle de nævnte metaller, den bedste katalysator for CO oxidation. Ved høj-temperatur reaktions-betingelser bliver den tætpakkede Pt-overflade dog den katalytisk mest aktive. Vi viser desuden, at den katalytiske aktivitet ændres med koordinations-tallet for metal-atomerne ved de aktive sites. Denne effekt vises at være elektronisk af natur eftersom lavt koordinerede metal atomer, som binder reaktanter stærkest, har de mest høj-energetiske metal d-tilstande.

Vi sammenligner vores teoretiske studie af CO oxidation med eksperimentelle studier. De sidstnævnte viser forøget katalytisk aktivitet når guldpartiklernes størrelse formindskes til 5 nm. Vi fandt, at oxidation af CO med N_2O involverer en CO-O overgangs-tilstand med atomart O adsorberet på guld B5 sitet og CO på hjørnerne. På den anden side foregår CO oxidation ved molekylært O_2 via en

anden reaktionsvej, som i stedet involverer et metastabilt CO-O_2 intermediat. Selvom de to oxiderende forbindelser forløber via forskellige reaktionsveje på forskellige aktive sites finder vi dog, at den umiddelbart overordnede aktiveringsbarriere fundet ved teori og eksperiment er den samme. De eksperimentelle resultater er i god overensstemmelse med vores teoretiske beregninger.

I anden del af denne afhandling fokuseres på forbedring af konvergens-egenskaberne for Quasi-Newton algoritmen. Egenværdierne af Hessian-matricen for en model af metallisk Cu, indeholdende 54 atomer, beregnes og distributionen af egenværdiernes størrelse følger en potensfunktion. Vi finder, at anharmoniciteten af de svage tilstande leder til dårlige Newton-skridt og dårlige Hessian-opdateringer i BFGS Quasi-Newton algoritmen, hvilket gør geometri-optimeringen langsommere. En linie-afsøgning som opfylder Wolfe-kriterierne anvendes derefter til at forbedre opdateringen af Hessianen. Vi parametriserede optimerings-algoritmen og gennemsøgte parameterrummet for forskellige test-tilfælde, for at finde det optimale sæt af parametre til problemer af at typen overflade-adsorption. Testtilfældende viser, at BFGS-algoritmen med linieafsøgnings-metoden med de optimerede parametre giver en betydelig forbedring af geometri-optimeringens konvergens.

Det gennemsøgte parameterrum for algoritmen viser, at sættes værdien af forbehandleren til at være midt i egenværdi-spektret opnås en hurtigere konvergens. Vi præsenterer herefter en adaptiv opdaterings-metode (AUM) til justering af forbehandlerne for de ikke-opdaterede tilstande, således at de dynamisk sættes til at være midt i egenværdi-spektret. Test-resultater viser, at AUM-metoden er i stand til at justere dårligt indstillede forbehandlere i adskillige skridt og forbedre konvergens-raten.

Til sidst bruger vi et model-potential, som beskriver strækning af bindinger, til at beregne Hessian-matricen. Sammenligning med den eksakte Hessian viser, at model-Hessianen reproducerer de vibrationelle tilstande på rimelig vis, på trods af dens forenkling. For homogene systemer vises, at forbehandling af optimerings-algoritmen med model-Hessianen reducerer konditions-nummeret med en faktor 14 og i høj grad forbedrer konvergens-raten.

Preface

This thesis is submitted in candidacy for a Ph.D. degree from the Technical University of Denmark (DTU). The work presented has been carried out at the Center for Atomic-scale Materials Design (CAMd) from October 2007 to December 2010 under the supervision of Professor Jens K. Nøskov and Associate Professor Thomas Bligaard from CAMd. The Lundbeck Foundation is gratefully acknowledged for the financial support.

I would like to thank my supervisors, Jens K. Nøskov and Thomas Bligaard for the excellent supervision and enthusiasm. I thank Jens for sharing his vision and great knowledge of the field of catalysis. I would also like to thank Thomas for so many hours of discussion and examining my code.

I would like to thank all my collaborators, Duncan Mowbray, Hanne Falsig, Britt Hvolbæk, Guido Walther and Keld Lungaard for the excellent collaboration, our works together are absolutely smooth and fruitful.

I would like to thank David Landis for all the helps out of the office and being the best flatmate. I would like to thank Ana Sofia Varela Gasque for help me through the most stressful half a year of my Ph.D. study, it was absolutely an amazing experience. I would also like to thank Marcin Dułak for reading through my thesis.

At last, I would like to thank all the friends, especially la gente que habla español, for making my staying in Denmark absolutely wonderful and unforgettable.

Lyngby, December 2010

Tao Jiang

Papers included in the thesis

1 H. Falsig, B. Hvolbæk, I. S. Kristensen, T. Jiang, T. Bligaard, C. H. Christensen, and J. K. Nørskov. Trends in the Catalytic CO Oxidation Activity of Nanoparticles. Angew. Chem. Int. Ed. 2008,47, 4835.

2 G. Walther, D. J. Mowbray, T. Jiang, G. Jones, S. Jensen, U. J. Quaade, and S. Horch. Oxidation of CO and H_2 by O_2 and N_2O on Au/TiO_2 catalysts in microreactors. Journal of Catalysis. 2008, 260, 86.

3 T. Jiang, D. J. Mowbray, S. Dobrin, H. Falsig, B. Hvolbæk, T. Bligaard, and J. K. Nørskov. Trends in CO Oxidation Rates for Metal Nanoparticles and Close-Packed, Stepped, and Kinked Surfaces. J. Phys. Chem. C 2009, 113, 10548.

4 B. D. Chandler, F. Abild-Pederson, T. Jiang, J. K. Nørskov. Tuning Au Surface Chemistry with Heterometals: A Computational Study. manuscript preparing.

Contents

Chapter 1

Introduction

Catalysts with its unique ability of accelerating chemical reactions, have been used widely in industry. Appoximately 85-90% of the chemical industry are facilitated by catalysts[16], providing us a wide range of products such as fertilizers, fuels, plastics and drugs that have made the life of mankind more convenient. Catalysts also play important roles in the applications including environmental protection and energy conversion processes that are of key importance for the future of mankind. Heterogeneous catalysts, being able to work under high temperature and pressure, and easy to be separated from product, are used extensively in all pre-mentioned sections.

A typical reaction promoted by heterogeneous catalyst consists of three major steps. First, reactant molecules adsorb on the catalyst and be dissociated. The reaction is then take place on the surface, forming products. Finally the products desorb, leaving the surface available for the new cycle of reaction.These steps requires catalyst that is able to both adsorb the reactants and cleaves the required bonds, and lets the products desorb back into the surrounding phase when reaction finishes. It is also required for the catalyst to be able to hold the reactants in close proximity so that they can react[62]. Therefore understanding the surface structural dependence as well as the material dependence of each elementary step and the overall reaction, and eventually designing catalysts for specific reactions based on the understanding are of great interests and tremendous challenge to researchers.

To gain fundamental understanding of catalytic reaction we need tools. Density functional theory calculation is proven to be a efficient semi-quantitative method for studying surface reactions, and is used as the main workhorse in this thesis. Study of catalytic reactions involves search for states and paths of minimum energies that requires means of energy minimization. As the size and complexity of the systems in interest in theoretical catalysis are increasing, it is becoming more and more important in the *ab initio* prediction of structures, since a good algorithm can easily save 30 % of time and computational resource.

A large number of minimization algorithms have been developed by mathematicians to deal with general minimization problems. Many of them have been adapted by the theoretical catalysis and computational chemistry community, such as Conjugate Gradient methods (CG) and Quasi-Newton methods (QN), and most of the first principle codes have their own implementations of these algorithms. Despite its great importance, only a small number of the studies of minimization algorithms performance on theoretical chemistry and surface science systems exist. These studies mainly focus on the usage of internal coordinates[71, 4] and model Hessian matrix[78, 23]. In this work the behavior of the BFGS type of Quasi-Newton algorithm on various cases in first-principle calculations is studied. The algorithm is specifically tuned to problems in theoretical catalysis to get an improved performance.

The outline of this thesis is as follows. Chapter 2 and chapter 3 give a brief introduction to Density Functional Theory and an overview of the optimization algorithms used in theoretical catalysis. Chapter 4 and chapter 5 discuss important concepts in catalysis and analytical tool of microkinetic modeling for understanding catalytic reactions. Chapter 6 focuses on the theoretical study of a well known model reaction, CO oxidation, on a variety of transition metals and alloys with different surface geometries – facets, steps, edges and kinks. Together with microkinetic modeling we are able to get atomic level understanding of reaction process, and the trend of the catalytic reactivity on various transition metals with different surface structures. The study gives understanding to the extraordinary activity of Au nanoparticles to CO oxidation found by Professor Haruta[40]. In chapter 7 the catalytic activity change of Au by alloying in the near surface area with other transition metals is studied. Chapter 8 gives the study of eigenvalue spectrum which is a basis of studying minimization algorithm. BFGS type Quasi-Newton algorithm is parameterized and the parameter space is scanned for the optimum set of parameters for theoretical catalysis problems. The last part of chapter 8 proposes two different ways of preconditioning the BFGS algorithm and the test results are given. Finally, chapter 9 presents an overall conclusion and outlook.

Chapter 2

Electronic structure calculation

To study a chemical reaction, we need to get energetic information about bonding in molecules or between molecules and a catalytic surface. This information is determined by the electronic structure of the system being studied. Through experiments or electronic structure calculation, we can obtain this information and study the system of interest. However, obtaining an exact solution of the Schrödinger equation of the system of interest is normally beyond the computational power nowadays. With the improvement of the theoretical methods, we are able to solve the electronic structure problem approximately to get the energetics of model catalytic systems at desirable accuracy level with acceptable computational cost. The aim of this chapter is to give a brief introduction to methodologies used in this thesis for electronic structure calculation as well as geometry optimization.

2.1 The Schrödinger equation

According to quantum mechanics, all the information about a system is contained in its wavefunction $\Psi(r_1, ..., r_N; R_1, ..., R_N; t)$, which is a function of electronic coordinates r_i (including spin coordinates), nuclei coordinates R_i and

time t. The wave function satisfies the time dependent Schrödiner equation

$$\hat{H}\Psi = i\frac{\partial}{\partial t}\Psi, \tag{2.1}$$

where $\hat{H}$ is the Hamiltonian operator. In a catalytic system, the problem we normally deal with is not time dependent, the time dependent Schrödiner equation is then reduced to the time independent Schrödiner equation. As the nuclei are 3 to 4 orders of magnitude heavier than the electrons, the Born-Oppenheimer approximation can be applied to decouple the motion of nuclei and electrons. The problem is then simplified to electronic structure problem and nuclei movement. Assuming the stationary of nuclei, we get the N-electron time independent Schrödiner equation:

$$\hat{H}\Psi = E\Psi. \tag{2.2}$$

With $\Psi = \Psi(r_1, ..., r_N)$ being the N particle wave function and E being the electronic energy of the system. If we adopt atomic units $\hbar = m_e = e = 4\pi/\epsilon_0 = 1$, the hamiltonian $\hat{H}$ can be written as

$$\hat{H} = -\frac{1}{2}\sum_{i=1}^{N}\nabla_i^2 + \sum_{i=1}^{N}\upsilon_{ext}(r_i) + \frac{1}{2}\sum_{i\neq j}^{N}\frac{1}{|r_i - r_j|}. \tag{2.3}$$

The first term on the right hand side is kinetic energy operator for the electrons ($\hat{T}$), the second term is the external potential acting on electrons due to the nuclei ($\hat{V}_{ext}$), and the last term is the electron-electron interaction ($\hat{V}_{int}$). The Hamiltonian in equation 2.3 is then represented by

$$\hat{H} = \hat{T} + \hat{V}_{ext} + \hat{V}_{int}. \tag{2.4}$$

2.2 Density functional theory

The main problem for electronic structure calculation is to find the solution to equation 2.2 with the Hamiltonian in equation 2.3. It is however extremely computational intensive given the high dimension of the problem ($3N$). Due to the development of density functional theory (DFT), we are now able to simplify the electronic problem with ($3N$) variables into one with only 3 variables, while giving results with desirable accuracy. The Core part that resulted in the success of DFT in chemical application are **Hohenberg Kohn theorems**, **Kohn Sham theorems** and **Generalized Gradient Approximations**.

2.2.1 Hohenberg Kohn theorems

It is evident that the ground state is uniquely defined by the external potential which specifies the system, and number of electrons in the potential. In 1964 Hohenberg and Kohn showed that the ground state density $n_0(\boldsymbol{r})$ uniquely determine the external potential, which will further determine the ground state wave function. In other words, ground state wave function $\Psi_0(\boldsymbol{r}_1, r_2, ..., r_N)$ is a functional of n_0, so are all the ground state observables as they are determined by Ψ_0. This is known as the **Hohenberg-Kohn theorem 1** and its corollary. Note now that the $3N$-variable problem is reduced to 3-variable problem.

Considering the total energy functional is uniquely determined by $n(\mathbf{r})$, it can be viewed as functional of $n(\boldsymbol{r})$:

$$E[n] = T[n] + V_{ext}[n] + \int d^3 V_{\mathrm{e}xt}(\boldsymbol{r}) n(\boldsymbol{r}). \tag{2.5}$$

Hence,

Hohenberg-Kohn theorem 2 the ground state energy is the global minimum value of the total energy functional, and the density that minimizes the functional is the ground state density $n_0(\boldsymbol{r})$:

$$E_{\upsilon}[n_0] \leq E_{\upsilon}[n'] \tag{2.6}$$

where n_0 is ground state density in potential υ and n' is a trial density. By minimizing the total energy of the system, 2.5, one would find the exact ground state.

Levy and Lieb provided an alternative minimization scheme, in which a two-step minimization procedure is defined as:

$$E_0 = \min_n \{ \min_{\Psi \to n} [\langle \Psi | \hat{T} + \hat{V}_{int} | \Psi \rangle + \int d\boldsymbol{r} V_{\mathrm{e}xt}(\boldsymbol{r}) n(\boldsymbol{r})] \} \tag{2.7}$$

However, no method has been given to find $T[n] + V_{\mathrm{i}nt}[n]$, a better approach to obtain the functional was proposed by Kohn and Sham in 1965.

2.2.2 Kohn Sham Equations

Kohn and Sham proposed an alternative scheme which maps a system of interacting particles located in an external potential onto a system of non-interacting particles in an effective potential $\upsilon_{\mathrm{e}ff}$ which has the same ground state density. According to **HK** theorem, total energies of the two systems are the same.

In Kohn-Sham auxiliary system, the total energy is

$$E[n(\boldsymbol{r})] = T_{\rm s}[n(\boldsymbol{r})] + V_H[n(\boldsymbol{r})] + E_{\rm xc}[n(\boldsymbol{r})] + V_{ext}[n(\boldsymbol{r})], \tag{2.8}$$

where $T_s[n(\boldsymbol{r})]$ is the kinetic energy of a non-interacting electron gas, $V_H[n(\boldsymbol{r})] = \frac{1}{2}\int\int \frac{[n(\boldsymbol{r}')][n(\mathbf{r})]}{|\boldsymbol{r}-\boldsymbol{r}'|} d\boldsymbol{r}' d\boldsymbol{r}$ is the Hartree energy. In equation 2.8, a correction called exchange correlation energy is introduced to incorporate the electron exchange and correlation. The exact form of the exchange correlation functional is not known, and it is still a big challenge in DFT today to develop an accurate yet efficient approximation to the exact E_{xc}.

To get the T_s we need to solve a single particle Schödinger equation

$$[-\frac{1}{2}\nabla^2 + \upsilon_{eff}(\boldsymbol{r})]\psi_i = \varepsilon\psi_i, \tag{2.9}$$

which subject to

$$n(\boldsymbol{r}) = \sum_{i\in occupied} |\psi|_i^2. \tag{2.10}$$

The effective potential is defined as

$$\upsilon_{eff}(\boldsymbol{r}) = \upsilon_{ext}(\boldsymbol{r}) + \int \frac{n(\boldsymbol{r}')}{|\boldsymbol{r}-\boldsymbol{r}'|} d\boldsymbol{r} + \frac{\delta E_{\rm xc}[n(\boldsymbol{r})]}{\delta n(\boldsymbol{r})}. \tag{2.11}$$

The set of quation 2.9 and 2.11 is called Kohn-Sham equations, and it is solved iterately with the resulting density and total energy given by equation 2.8 and 2.10.

2.2.3 Exchange Correlation Functional

The accuracy of Kohn-Sham approach depends largely on the exchange correlation functional $E_{\rm xc}[n]$, which made it the crucial quantity. Kohn and Sham noticed that electrons in solids can often be considered to be close homogeneous electron gas, meaning that the effects of exchange and correlation are local. This give rise to the local density approximation (LDA),

$$E_{\rm xc}^{LDA} = \int \epsilon_{\rm xc}^{hom}(n(\boldsymbol{r}))n(\boldsymbol{r})d\boldsymbol{r}, \tag{2.12}$$

were $\epsilon_{\rm xc}^{hom}$ is the energy of the exchange-correlation hole in the homogeneous electron gas of density n. By introducing spin density, LDA can be extended to local spin density approximation (LSDA) to treat spin-polarized systems. LDA describes properties of solids surprisingly well, despite its simplicity. The reason

is that it obeys the sum rules of the "exchange-correlation hole" (xc hole) [45] and the E_{xc} depends on the spherical average of the xc hole.

A chemical system normally involve molecules which means bigger change in density. It is hence not until the development of generalized-gradient approximates (GGAs), DFT is widely used in studying chemical reactions. The GGA type of xc energy depends both on the density and its gradient, which gives a big improvement over LDA.

$$E_{\mathrm{xc}}^{\mathrm{GGA}}[n] = \int n(\boldsymbol{r})\epsilon_{\mathrm{xc}}^{\mathrm{GGA}}(n(\boldsymbol{r}), \nabla n(\boldsymbol{r}))d\boldsymbol{r} \tag{2.13}$$

Different flavors of GGA functionals have been developed, most notable ones including PBE[68], PW91[69], revPBE[89] and RPBE[35]. For surface adsorption, RPBE functional gives good adsorption energies with overestimations of around 0.25 eV[35].

Chapter 3

Geometry optimization

In the previous chapter we introduced the methodology of doing electronic structure calculations. However, Solving $H\psi = E\psi$ for the electronic structure is only half the problem of theoretical catalysis. Typically many geometries (or choices of R_is) are needed to derive information of materials properties. Most important geometry in this respect is the ground state. Finding the ground state, however, is not at all a trivial task. By applying Born-Oppenheimer approximation the motion of nuclei and electrons can be decoupled, that leads to a separable Hamiltonian which is parametric dependent on nuclei coordinates R_i. The potential energy part of the Hamiltonian is differentiable, and the force (first order derivative of energy) can be easily calculated by Hellmann-Feynman theorem[44, 25], making it possible for optimization methods using first order derivative. Higher order algorithms are not adapted due to the extra cost for computing higher order derivative.

A number of algorithms are used commonly for geometry optimization. Among these algorithms, Molecular Dynamics Minimization (MDmin), Fast Inertial Relaxation Engine (FIRE), Conjugate Gradient method (CG) and Quasi-Newton (QN) methods are particularly powerful and implemented in many codes.

3.1 Molecular dynamics minimization

Molecular Dynamic (MD) minimizer is a simple algorithm which takes the physics of the problem into account by assuming the system to be optimized moving on the potential energy surface (PES) [81, 46]. Newton's second law of motion is solved numerically, at each time step the velocity of the system is updated by $\nu_i = \nu_{i-1} + a\Delta t$, where a and Δt are the acceleration of the system and the time step. The mass of the system is set to zero, hence the acceleration a equals to the force. At each time step, the projection of force on the momentum is checked, if it equals zero, the local minimum is found and the momentum is set to zero, otherwise continue. The algorithm can be expressed as follows.

Algorithm 3.1 (Molecular dynamics minimizer)
Choose $\Delta t > 0$;
set $i \leftarrow 0$, $\nu_i \leftarrow \nabla f_i \Delta t$;
$\vec{x}_1 \leftarrow \vec{x}_0 + \vec{\nu}_0 \Delta t$;
$i \leftarrow i + 1$;
repeat
  if $\nabla f_i \cdot \vec{\nu}_{i-1} = 0$
    $\vec{x}_* = \vec{x}_i$ and **stop**;
  else
    $\vec{\nu}_i \leftarrow \nabla f_i \Delta t$;
    $\vec{x}_{i+1} \leftarrow \vec{x}_i + \vec{\nu}_i \Delta t$;
    $i \leftarrow i + 1$;
end (repeat)

MD works well in general, however, when the system is located in the vicinity of a local minimum, it is preferable to use algorithms which utilizing the function derivatives more efficiently, such as Conjugate gradient or Quasi-Newton algorithms.

3.1.1 Fast inertial relaxation engine

The Fast Inertial Relaxation Engine (FIRE) is a modification of the standard MD method. The equation of motion is given by:

$$\nabla \vec{\nu} = -\nabla f(x)/m - \gamma(t)(\vec{\nu}(t) - \vec{\nu}(t)\nabla f(x)). \tag{3.1}$$

As is shown in equation (3.1), an acceleration in a "steeper" direction is introduced than the current direction of motion via the function $\gamma(t)$. If the motion leads to a uphill motion, i.e. $P(t) = \nabla f(x) \cdot \vec{\nu}(t)$. The time step Δt is optimized

in a stable manner, that is increase time step Δt when $\vec{\nu}(t)\nabla f(x) > 0$ and decrease Δt when $\vec{\nu}(t)\nabla f(x) < 0$. The algorithm is simply adding couple of lines in algorithm 3.1:

Algorithm 3.2 (Fast Inertial Relaxation Engine)
Choose $\Delta t > 0$, $N_{\min}$, f_{inc}, f_{dec}, α_{start}, f_α and $\Delta t_{\max}$;
set $i \leftarrow 0$, $\nu_i \leftarrow \nabla f_i \Delta t$, $N_{\text{steps}} \leftarrow 0$, $\alpha \leftarrow \alpha_{\text{start}}$;
$\vec{x}_1 \leftarrow \vec{x}_0 + \vec{\nu}_0 \Delta t$;
$i \leftarrow i + 1$;
repeat
  if $\nabla f_i \cdot \vec{\nu}_{i-1} = 0$
    $\vec{x}_* = \vec{x}_i$ and **stop**;
  else
    if $\nabla f_i \cdot \vec{\nu}_{i-1} > 0$
      $\vec{\nu}_i \leftarrow (1-\alpha)\vec{\nu}_{i-1} + \alpha \nabla f_i \frac{|\vec{\nu}_{i-1}|}{|\nabla f_i|}$
      if $N_{\text{steps}} > N_{\min}$
        $\Delta t \leftarrow \min\{\Delta t f_{\text{inc}}, \Delta t_{\max}\}$;
        $\alpha \leftarrow \alpha f_\alpha$;
      $N_{\text{steps}} \leftarrow N_{\text{steps}} + 1$;
    else
      $\vec{\nu}_i \leftarrow 0$;
      $\alpha \leftarrow \alpha_{\text{start}}$;
      $\Delta t \leftarrow \Delta t f_{\text{dec}}$;
      $N_{\text{steps}} \leftarrow 0$;
    $\vec{\nu}_i \leftarrow \nabla f_i \Delta t$;
    $\vec{x}_{i+1} \leftarrow \vec{x}_i + \vec{\nu}_i \Delta t$;
    $i \leftarrow i + 1$
end (repeat)

The FIRE algorithm works surprisingly well, despite its simplicity. Tests on different cases show that it is comparable to the commonly used conjugate gradient (CG) and BFGS Quasi-Newton algorithms. It is also ideally suited for the transition state searching, where competing methods often fail[6].

3.2 Conjugate Gradient Method

The conjugate gradient method (CG) is originally designed as an iterative method for finding the numerical solution of systems of linear equations

$$Ax = b, \tag{3.2}$$

where A is an $n \times n$ matrix that is symmetric and positive definite. The problem (3.2) is equivalent to a problem of minimizing convex quadratic functions

$$\phi(x) = 1/2x^T Ax - b^T x, \tag{3.3}$$

in which the residual of the linear system or the gradient of the quadratic function

$$\nabla\phi(x) = Ax - b \tag{3.4}$$

is reduced. The CG algorithm for solving linear system can be found in various sources [70, 64].

If we use the convex quadratic function ϕ as a fit to general nonlinear function f, the CG method can be adapted as an minimization algorithm to nonlinear systems. By applying a line search to locate an approximate minimum of the nonlinear function f along search direction and replace $\nabla\phi$ by the gradient of the nonlinear objective function f, Fletcher and Reeves created the nonlinear Conjugate Gradient Method. The algorithm is described below

Algorithm 3.2 (Nonlinear Conjugate Gradient Method)
Evaluate $f_0 = f(x_0), \nabla f_0 = \nabla f(x_0)$;
Set $p_0 \leftarrow -\nabla f_0, k \leftarrow 0$;
repeat
Compute α_i and set $x_{i+1} = x_i + \alpha_i p_i$;
Evaluate ∇f_{i+1};
if f_{i+1} or ∇f_{i+1} reaches convergence criteria
$x_* = x_{i+1}$ and **stop**
else
$\beta_{i+1} \leftarrow \frac{\nabla f_{i+1}^T \nabla f_{i+1}}{\nabla f_i^T \nabla f_i}$;
$p_{i+1} \leftarrow -\nabla f_{i+1} + \beta_{i+1} p_i$;
$i \leftarrow i + 1$
end (repeat)

Here the step size α_i is determined by a constrained line search, the detail of constrained line search will be discussed in section 3.5.

The rate of convergence of CG method is satisfactory when comparing to MD-Min. However, when a poor search direction is taken, it is hard for CG algorithm to correct this error, some kind of restart strategy is needed to terminate the bad step and restart along the steepest descent direction.

3.3 Newton's method

Newton's method is a well-known algorithm for finding stationary points for a multi-dimentional function $f(\boldsymbol{x})$[64]. The idea of the algorithm is to use a quadratic model to fit the object function $f(\boldsymbol{x})$ being minimized at the current iterate $\boldsymbol{x}_i$:

$$m_i(\boldsymbol{p}) = f_i + \nabla f_i^T p + \frac{1}{2} p^T B_i p, \tag{3.5}$$

where B_i is the second derivative of the model, which is normally called the Hessian matrix. Note that the value, gradient and the second derivative of the model match f_i, ∇f_i and $\nabla^2 f_i$ at $p = 0$. The minimizer of the convex quadratic model $p = p_i$ is found by setting it to

$$p_i = -B_i^{-1} \nabla f_i, \tag{3.6}$$

and is used as the search direction. The new iterate is then

$$x_{i+1} = x_i + \alpha_i p_i, \tag{3.7}$$

where α_i is the step length along the search direction which will be discussed later.

Newton's method converges to the minimum quadratically, the problem is that the Hessian needs to be calculated. For a system with n atoms, $6 \times n$ function derivatives need to be calculated to get the Hessian matrix, which in many cases is very expensive.

3.4 Quasi-Newton method

Quasi-Newton methods use the same Newton step (3.6) to decide the search direction. The difference is, the exact Hessian is not computed in each step. Instead, the starting B_0 is set to βI, where β is the preconditioning factor and I is the unit matrix. During the iterations the matrix B_i is updated with some scheme so that it approximates the Hessian $\nabla^2 f_i$, while the object function is minimized. By doing so, evaluation of the Hessian is prevented, while keeping the super linear convergence[19, 27]. Since the Hessian is updated during the whole optimization, it is also called the variable-metric method.

To simplify the notation, s_i and y_i are defined as

$$s_i = x_{i+1} - x_i, y_i = \nabla f_{i+1} - \nabla f_i. \tag{3.8}$$

The requirement of the model function to match the gradient of the object function at the latest two iterates x_i and x_{i+1} give rise to the secant equation:

$$B_{i+1}s_i = y_i \tag{3.9}$$

The so called curvature condition

$$s_i^T y_i > 0, \tag{3.10}$$

to ensure the gradient approaching zero then suggest that the B_{i+1} shall be positive definite. The proof can be found simply by premultiplying (3.9) by s_i^T. When the object function f is strongly convex, equation (3.10) will be satisfied for any two points x_i and x_{i+1}. However, in theoretical catalysis, the potential energy surface (PES) is not guaranteed to be convex, and this condition may not always hold. In this case, we need to enforce (3.10) by carrying out line search with restrictions, so that the gradient is ensured to decrease. Further discussion about the line search algorithm will be given in the following section.

There are different ways of deciding the update scheme of B_i, among which the Broyden-Fletcher-Goldfarb-Shanno (BFGS) algorithm is the most effective one[64]. The update formula is

$$B_{i+1} = B_i - \frac{B_i s_i s_i^T B_i}{s_i^T B_i s_i} + \frac{y_i y_i^T}{y_i^T s_i}. \tag{3.11}$$

An alternative way is to update the inverse of Hessian approximation H_i by

$$H_{i+1} = (I - \rho_i s_{iy_i^T})H_i(I - \rho_i y_i s_i^T) + \rho_i s_i s_i^T, \tag{3.12}$$

where

$$\rho_i = \frac{1}{y_i^T s_i}. \tag{3.13}$$

It is normally used in systems in which the size of the Hessian approximations B_i are sufficiently large, that solving the linear system $B_i p_i = -\nabla f_i$ to get p_i can be expensive as this process scales to n^3.

A simple implementation of BFGS Quasi-Newton algorithm with BFGS update scheme is described as follows.

Algorithm 3.3 (BFGS algorithm)
Choose β;
set $i \leftarrow 0$; $B_i \leftarrow \beta I$;
repeat
$x_{i+1} \leftarrow x_i + B_i^{-1}\nabla f_i$;

evaluate f_{i+1}, ∇f_{i+1};
if f_{i+1} or ∇f_{i+1} reaches convergence criteria
$x_* = x_{i+1}$ and **stop**
else
$s_i \leftarrow x_{i+1} - x_i$; $y_i \leftarrow \nabla f_{i+1} - \nabla f_i$;
$B_{i+1} \leftarrow B_i - \frac{B_i s_i s_i^T B_i}{s_i^T B_i s_i} + \frac{y_i y_i^T}{y_i^T s_i}$;
$i \leftarrow i + 1$
end (repeat)

Here I means unitary matrix. In some implementation the inverse of Hessian (H) is updated instead, corresponding lines of the code should be change.

Properties of the BFGS method

The BFGS method is often observed to give superlinear rate of convergence in various problems [12, 21] including theoretical catalysis problems. We listed below the last few iterations of relaxation done by Fire and BFGS method on a typical problem of relaxing a Cu 27 atoms bulk structure with all the atoms randomly displaced by 0.2 Å. The total energy calculator uses effective medium theory to describe the inter-atomic interactions. The FIRE method took 155 iterations to reduce the force down to 1e-3 eV/Å, whereas BFGS requires only 31 iterations.

FIRE	BFGS
2.817e-4	2.503e-2
2.747e-4	5.303e-3
2.662e-4	2.732e-3
2.560e-4	9.069e-4
2.437e-4	3.583e-4
2.290e-4	2.036e-4
2.114e-4	1.210e-4

The BFGS also holds a very effective self-correcting property [63] when the Hessian incorrectly estimates the curvature of the PES and slows down the optimization. However, this self-correcting property only holds when an adequate line search is performed together with BFGS method to capture appropriate curvature information.

3.5 Line search algorithm

3.5.1 The Wolfe conditions

Quasi-Newton methods works well in the vicinity of the minimum where the function landscape can be well described by a quadratic function. However, when the quadratic model does not describe the landscape at the present step well, the Newton step given by (3.6) may not lead us close enough to the minimum, or in a even worse case, direct the system to a place with higher gradient. In the latter case, Hessian will be updated with a negative eigenvalue, which may suggest an uphill direction in the following step. A line search along the search direction is needed to ensure a sufficient decrease in the object function f and the gradient ∇f.

The ideal choice of the line search would be the minimum of the univariate function ϕ defined by

$$\phi(\alpha) = f(x_i + \alpha p_i), \quad \alpha > 0. \tag{3.14}$$

It is however too expensive to locate the exact minimum as it requires too many evaluations of the objective function f. In practice, an inexact line search is performed to achieve adequate reductions in f at minimal cost.

To ensure the inexact line search efficient, conditions should be imposed on the step length α, Wolfe conditions [86] is a very popular one, as illustrated in Figure 3.1 and formulated below:

$$f(x_i + \alpha p_i) \leq f(x_i) + c_1 \alpha_i \nabla f_i^T p_i, \tag{3.15a}$$

$$\nabla f(x_i + \alpha_i p_i)^T p_i \geq c_2 \nabla f_i^T p_i, \tag{3.15b}$$

with $0 < c_1 < c_2 < 1$. These two equations are normally called the sufficient decrease condition and the curvature condition.

As can be seen in Figure 3.1, a step length may satisfy the Wolfe conditions without being particularly close to a minimum, in the case when the gradients are too positive. The curvature condition (3.15b) can be strengthened to

$$|\nabla f(x_i + \alpha_i p_i)^T p_i| \geq c_2 |\nabla f_i^T p_i| \tag{3.16}$$

to enforce α_i to lie in a broad neighborhood of a local minimum or stationary point of ϕ. Equation (3.15a) and (3.16) together are called the strong Wolfe conditions.

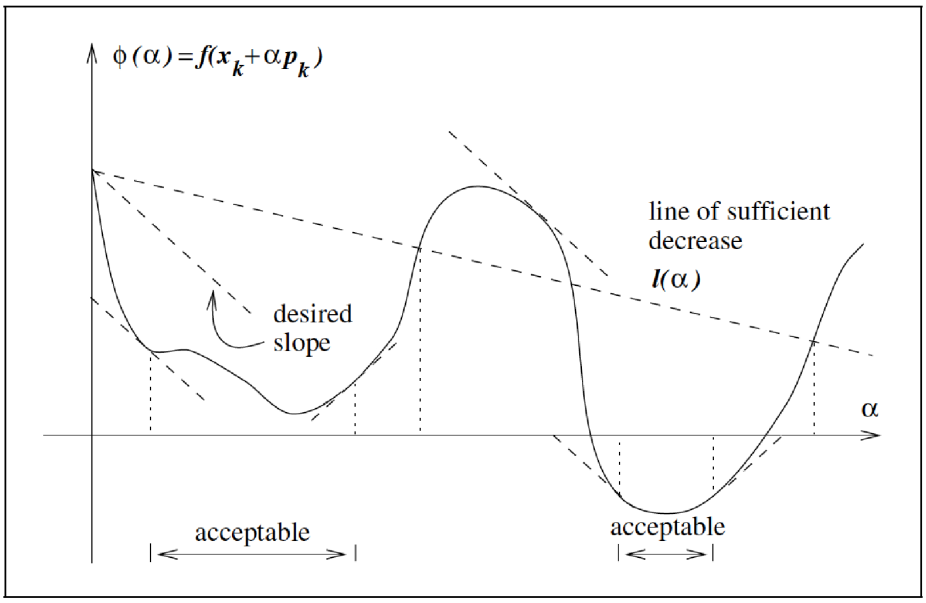

Figure 3.1: An illustration of the strong Wolfe conditions in a line search.

3.5.2 Step size selection algorithms

The step size of a line search (α_i) is a scalar multiplied to the Newton step given by equation (8.6). When line search finishes, the system moves along the search direction by $\alpha_i|p_i|$. We normally choose 1 as the initial guess of the step size α_0, which may or may not fulfill Wolfe conditions. If not, interpolation shall be made to give a new step size by using the function value and function derivative of previous steps.

Interpolation

A popular interpolation scheme is to fit the univariate function in equation (3.14) with a quadratic function

$$\phi_q(\alpha) = a\alpha^2 + b\alpha + c \tag{3.17}$$

since there are three unknown variables a,b and c, we use three pieces of information $\phi(0)$,$\phi'(0)$ and $\phi(\alpha_0)$ to do the interpolation, and the new trial step is given as:

$$\alpha_1 = -\frac{\phi'(0)\alpha_0^2}{2[\phi(\alpha_0 - \phi(0) - \phi'(0)\alpha_0}. \tag{3.18}$$

If 4 pieces of information are available, a cubic function can be fitted. In our case, when we evaluate the function value, the function derivative can be obtained

with limited cost. Hence we have already 4 pieces of information after the first trial step, and the new step towards the local minimum of the cubic function is given by

$$\alpha_{i+1} = \alpha_i - (\alpha_i - \alpha_{i-1})[\frac{\phi'(\alpha_i) + \gamma - \theta}{\phi'(\alpha_i) - \phi'(\alpha_{i-1}) + 2\gamma}], \tag{3.19}$$

where

$$\gamma = \phi'(\alpha_{i-1}) + \phi'(\alpha_i - 3\frac{\phi(\alpha_{i-1}) - \phi(\alpha_i)}{\alpha_{i-1} - \alpha_i},$$
$$\theta = [\gamma^2 - \phi'(\alpha_{i-1}\phi'(\alpha_i)]^{1/2}.$$

Another popular fitting scheme is the secant method which is defined by

$$\alpha_{i+1} = \alpha_i - \phi'(\alpha_i)\frac{\alpha_i - \alpha_{i-1}}{\phi'(\alpha_i) - \phi'(\alpha_{i-1})}. \tag{3.20}$$

In DFT calculations, energies (object function) and forces (derivative of the object function) calculated normally have numerical noise due to limited basis set, that is, the forces may not be the exact derivative of potential energies. In some cases, the line search may not be able to terminate due to this incompatibility. Some termination conditions are therefore needed when line search can not progress.

Chapter 4

Heterogeneous catalysis

Normally a gas phase reaction requires high temperature and pressure which will greatly increase the cost and raise safety issues. Heterogeneous catalysts (normally with large surface area) are used to adsorb the reactants. The interaction between catalytic surface and adsorbate will weaken bond strength within the adsorbate molecule, a easier reaction paths toward produces is then possible, so that reactions happen under mild temperature and pressure. Furthermore, the catalysts should not bind the products too strongly so that the products can easily desorb from the catalyst surface once formed, leaving empty sites ready for the next catalytic cycle. It is important to note that once a chemical reaction reaches equilibrium, it is completely governed by its thermodynamics, no mater if the reaction is catalyzed or not. That is to say, the catalyst can only change the kinetics of a reaction and push is towards equilibrium much faster. In the following of this chapter, important concepts of heterogeneous catalysis used in this thesis will be discussed.

4.1 Reactions on catalyst surface

When a molecule approaches catalyst (often a transition metal) surface, it starts interacting with the surface and form a bond. If the interaction is a long range

one caused by dipoles, we say that the molecule is physisorbed on the surface. More importantly for this thesis, if the molecule goes even closer to the surface, direct interaction between the wave functions of the molecule and the catalyst happens, a much stronger, so called chemisorption takes place.

After adsorbed, if the molecule still has enough kinetic energy, it may bounce back to its original phase (in this thesis, gas phase is the reactant phase), overcome the diffusion barrier and move to a more favorable adsorption site, or overcome the dissociation barrier and form new intermediates. If we consider the energetic diagram of the surface reaction, we can see that the adsorbed molecule and these intermediates site in the local minima of the energetic diagram, and the energy barriers between these minima indicates the energy required to move between adsorbate and intermediates so that specific elementary reactions take place. The pathway between each of these two minima is called reaction path and the coordinate along the reaction path is called reaction coordinate.

Consider a simple dissociation reaction on the catalytic surface

$$\mathrm{A}_2 * + * -> 2\mathrm{A}*, \tag{4.1}$$

where $*$ denotes a catalytic site on the surface. Along the reaction coordinate we define the minima as initial state (IS) and final state (FS), and the top of the barrier between them as transition state (TS). There energies are defined as:

$$E^i = E_{i/\mathrm{substrate}} - E_{\mathrm{A}_{2(\mathrm{g})}} - E_{\mathrm{substrate}}, \tag{4.2}$$

where $E_{i/\mathrm{substrate}}, i = \mathrm{IS}$, TS and FS means the energy of corresponding state on the substrate, and $\mathrm{A}_{2(\mathrm{g})}$ means A_2 in gas phase. The activation energy (E_a) and reaction energy (ΔE) are then:

$$E_\mathrm{a} = E^{\mathrm{TS}} - E^{\mathrm{IS}}, \tag{4.3}$$

$$\Delta E = E^{\mathrm{FS}} - E^{\mathrm{IS}} \tag{4.4}$$

4.2 Chemisorption

If we assume that the majority of the adsorption energy is given by the interactions between adsorbate states and the sp-bands, the coupling to the metal d-bands is only a small perturbation, then the binding energy due to the adsorbate and metal substrate can be considered as the sum of energy gains of adsorbate state interacting with substrate sp bands and d bands [38, 37, 58]:

$$E_{\mathrm{binding}} = E_{sp} + E_{hyb-d} \tag{4.5}$$

A schematic illustration of the adsorbate/surface interaction is shown in figure 4.1

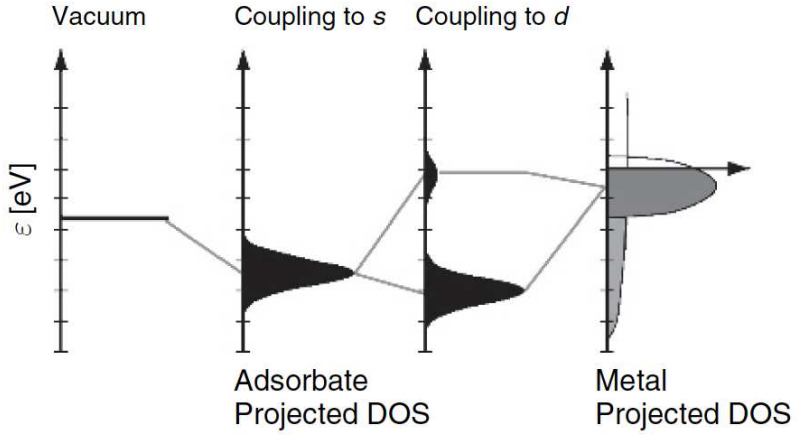

Figure 4.1: Schematic illustration of the formation of a chemical bond between an adsorbate valence level and the s and d states of a transition metal surface. Adapted from Ref. [38]

When adsorbate approaching the surface, adsorbate state first couple to the sp-states of the metal surface leading to a broadening and downshifting of the energy level. The broadened adsorbate state then interact with metal d-band and leads to a splitting of bonding below the adsorbate state and anti-bonding above the filled metal d-states.

Since transition metals all have half filled s bands, the contribution from coupling with sp bands does not change significantly. The chemical properties of the adsorption system are governed largely by the first moment of the d-band (also called the d-band center, ε_d), and the filling of the band, f. According to Hammer and Nørskov[38, 37], the binding energy from adsorbate state coupling to d band is approximately

$$E_{hyb-d} = -(1-f)(\sqrt{V^2 + (\varepsilon_d - \varepsilon_a)^2} - (\varepsilon_d - \varepsilon_a)) - 2(1+f)SV, \qquad (4.6)$$

where V is the coupling matrix element between the adsorbate orbitals and the metal d-states, ε_a is the energy of the adsorbate level, and S is the overlap matrix element. As the filling $f < 1$, the first term in equation (4.6) lowers energy due to the hybridization, while the second term accounts for the Pauli repulsion between adsorbate states and metal d-states.

4.3 Surface reactivity

The reactivity of catalysts varies greatly, for instance, adsorption energy of molecule on a series of transition metals can differ as high as 200 kcal/mol. It is also well known that even for the same transition metal, when the surface morphology changes, its reactivity changes. It has been observed that defect sites on the surface have higher activity than close-packed planar facets. The change of the surface reactivity can be divided into the results of electronic effect and geometrical effect of the catalytic sites.

If the same adsorbate adsorbed on a series of surface with the same binding geometry, the difference in adsorption energies is caused by the electronic structure difference of adsorption sites. Based on the discussion in the last section, we see that the d-band center ε_d of the transition metals is a good measure of the adsorption energy. Varying from one transition metal to another changes the d-band center, hence the adsorption energy. Going from the left side towards the right side of the periodic table, ε_d decreases, d-band filling increases, and the transition metal becomes more noble, meaning weaker catalytic reactivity. Even for the same metal, when stretching the surface or decreasing the coordination number, the overlap between the metal orbitals will be reduced, resulting a more localized d-band. When the d-band filling $f > 0.5$, ε_d will be shifted up by the increased localization of d-band to preserve the same filling f. If d-band filling $f < 0.5$, ε_d shifts toward the opposite direction. When the d-band center moves up in energy, the surface reactivity increases and vice versa.

The nature of the so called geometrical effect lies on the geometry of the transition state. Take N_2 dissociation as an example. When dissociating, the N_2 molecule lies on the surface and use as many surface atoms as possible so that the transition state is stabilized. If the reaction takes place on close-packed surfaces, up to 4 surface atoms can be used and one of the atoms has to interact with both N atoms during the dissociation. While on step surface, since the surface is more open, more atoms can be involved in the dissociation. On fcc(211) surface for example, the reaction takes place on the step, utilizes 5 atoms from both upper and lower terrace in the way that no surface atoms need to help stabilizing more than one N atom. The higher efficiency of using surface atoms on step surface stabilizes the transition state more, enables higher reaction rate.There are also reactions with rather weak geometry-dependence, methane dissociation for example. When breaking the the C-H bond, the transition state sits on top of a single surface atom, however open the surface structure is.

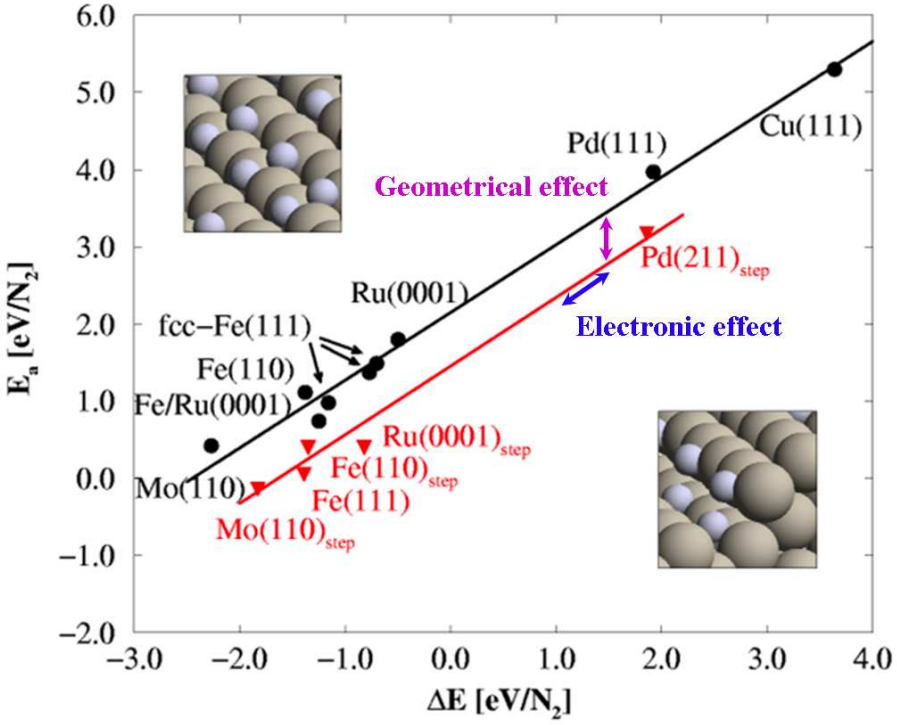

Figure 4.2: Calculated transition state energies for N_2 dissociation shown as a function of the dissociative chemisorption energy of N_2 for both close-packed and stepped metal surfaces. Adapted from [55]

4.4 Brønsted-Evans-Polanyi relation

Dating back to 1928, Brønsted and Evans, and Polanyi ten years later found that there exist linear correlations between activation energies and reaction energies of chemical reactions. The simplicity of Brønsted-Evans-Polanyi (BEP) relation can be described by:

$$E_a = \alpha \Delta E + \beta. \tag{4.7}$$

Where E_a and ΔE are the activation barrier and the reaction energy of the chemical reaction.The BEP relations also hold for heterogeneous catalysis and have been studied quantitavely since DFT calculations being able to provide sufficient accuracy. Figure 4.2 shows an example of BEP relation of N_2 dissociation studied by DFT calculation.

We see that data points fall nicely on two BEP lines. As discussed in previous section, more open step surface provides more atoms to stabilize the transition state, hence the energy of the transition state is lower. This is shown clearly

in figure 4.2 with a low lying BEP line for the step surface, which corresponds normally to a low β in equation (4.7).

For atomic adsorptions, adsorbates prefer sites that gives highest metal coordination number, which means the same local adsorption geometry on different surfaces. The change of the adsorption energy is only due to the electronic structure change from one metal to another or from one type of surface to another for the same metal. The shift along the BEP lines from one metal to another in figure 4.2 is a clear evidence. It is however important to note that it is not alway possible to decouple both effects. Going from close-packed surface to step surface reduces the coordination number of the surface atoms, which as discussed in last section, will change the d-band structure that in most cases determine the adsorption property. A further discussion about the electronic and geometrical effects on CO oxidation will be discussed in Chapter 6.

The α in equation (4.7) can be considered as a descriptor of the structure of the transition state. If the transition state structure is close to final state, the electronic structure change of the surface will influence the adsorption energy of the transition state in the same way that it influences the final state, α is close to 1, ΔE and E_a will move in the same way. Diatomic molecules such as N_2 and CO dissociation on the surface normally have BEP lines with slope close to 1. For elementary reactions such as simple molecule desorption α is normally negative since the transition state resembles the adsorption structure of the molecule on the surface.

4.5 Sabatier's Principle and volcano plot

In a catalytic reaction, the catalyst should bind the reactant sufficiently strong to assist the bond breaking of the reactant. After the reaction takes place, the product should be able to desorb from the surface so that the catalytic site is ready for the next catalytic cycle. The French chemist Paul Sabatier first realized this necessity of binding the adsorbate neither too strong nor too weak for a good catalyst, and this requirement is called Sabatier's Principle.

By plotting the adsorption energy against the catalytic activity we show the Sabatier's Principle in volcano shaped plot as in figure 4.3. Less reactive metals (large ΔE) can not dissociate the reactant easily, hence the catalytic activity is limited by the bond breaking. Reactive metals can easily dissociate the reactant, but they bind adsorbates so strong that the product won't desorb, and the over all reaction rate will be limited. The optimal catalyst should bind the adsorbate "just right", so that the reaction rate goes to the top of the volcano.

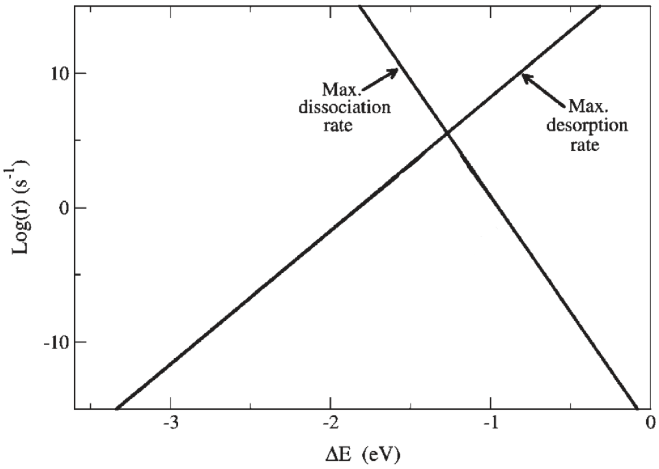

Figure 4.3: An illustration of the Sabatier volcano curve.

Chapter 5

Microkinetic modeling and Sabatier analysis

The main purpose of this thesis is to study the trend of catalytic activity of CO oxidation on transition metals with different surface structures. By combining microkinetic model with Sabatier analysis we have a powerful tool for studying catalytic activity qualitatively. In this chapter, we will use a simple model reaction to illustrate the methodology.

5.1 Microkinetic modeling

We consider a reaction

$$A_2(g) + 2B(g) \rightleftharpoons 2AB(g)$$

catalyzed by a transition metal. To simplify the problem, we assume that the reaction follows Eley-Rideal mechanism, that is, only reactant A adsorb on surface, reactant B approaches adsorbed A and react, without adsorbing on the catalyst first. The elementary steps of the reaction can be written as:

$$(R1) A_2 + 2* \rightleftharpoons 2A*,$$
$$(R2) A* + B \rightleftharpoons AB + *.$$

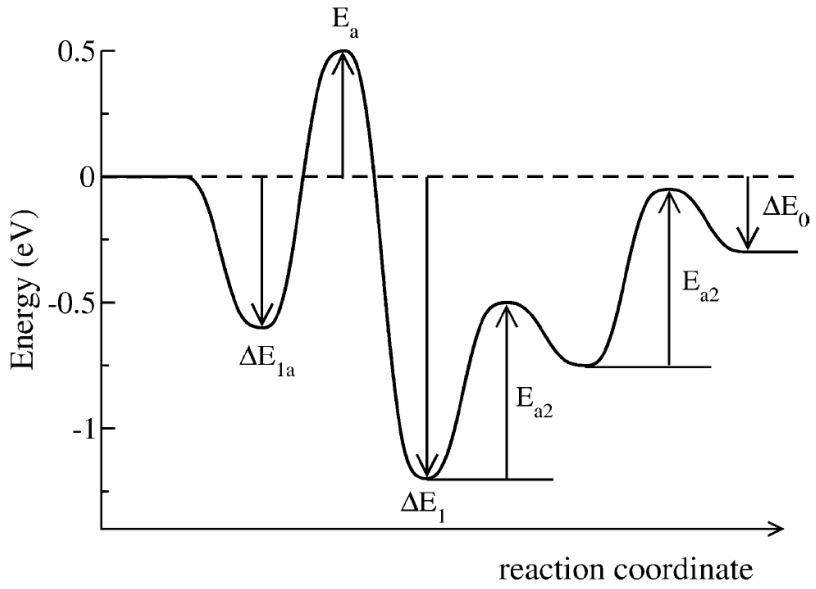

Figure 5.1: Schematic potential energy diagram for a surface reaction involving adsorption of A_2, dissociation of A_2, and two times reaction with B to form two AB molecules from A_2 and 2B. Adapted from [7].

The asterisk denotes active site on catalyst surface, and a species with an asterisk is the species adsorbed on an active site.

The reaction rate of the elementary reactions are given by:

$$r_1 = k_1^+ p_{\mathrm{A}_2} \theta_* - k_1^- \theta_{\mathrm{A}}^2, \tag{5.1}$$

$$r_2 = k_2^+ \theta_{\mathrm{A}} p_{\mathrm{B}} - k_2^- p_{\mathrm{AB}} \theta_*, \tag{5.2}$$

where p_{A_2}, p_{B} and p_{AB} are the partial pressure of each species, θ_* and θ_{A} are the coverage of free sites and atomic adsorbed A. The forward/backward rate constant $k_i^{+/-}$ for step (Ri) is given by:

$$k_i = \nu_i \exp\left[\frac{-\Delta E_{\mathrm{a}}^i - \Delta \mathrm{ZPE}_{\mathrm{a}i} + T\Delta S_{\mathrm{a}}^i}{k_{\mathrm{B}} T}\right], \tag{5.3}$$

where ν_i is the prefactor which is assumed to be metal independent and equals to $k_{\mathrm{B}}T/h$. ΔE_{a}^i is the activation energy of the elementary reaction (Ri), $\Delta \mathrm{ZPE}_{\mathrm{a}i}$ is the zero-point energy change, k_{B} is the Boltzmann constant, T is the temperature and h is the Planck constant. ΔS_{a}^i is the entropy change between the initial state and transition state of the elementary reaction (Ri), when there is gas phase species in initial state, ΔS_{a}^i is approximated by minus gas phase entropy $-S(\mathrm{g})$ since when adsorption takes place, the adsorbate is "frozen" on the active site and loses most of the entropy.

5.2 Sabatier analysis

The first Sabatier analysis was described by Bligaard et al[7]. The goal is to find the best catalyst when the reaction is running at optima, hence we assume that only forward reactions are considered and the coverage of free sites and surface species are assumed optimal for each reaction step in the forward direction. The so acquired upper bound of the reaction rate is called the Sabatier rate.

5.2.1 Descriptor

According to the assumptions for Sabatier analysis, the Sabatier rate of our model reaction depends on the activation energy of both elementary reactions, partial pressure of reactants and reaction temperature, that is, $r_{\text{Sabatier}} = f(E_a^1, E_a^2, p_{\text{A}_2}, p_{\text{B}}, T)$. If the partial pressure of reactants and the temperature are fixed, then $r_{\text{Sabatier}} = f(E_a^1, E_a^2)$.

According to the BEP relation, the activation energy scales linearly with the dissociative chemisorption of diatomic molecules. The activation barriers of the elementary steps are written as:

$$E\text{a}^i = \alpha_i \Delta E_i + \beta_i. \tag{5.4}$$

Here α_i and β_i are constants for the linear BEP relation. Let ΔE_{tot} be the reaction energy for the overall gas-phase reaction, since catalyst does not change the thermodynamics of the reaction, we get

$$\Delta E_2 = \frac{1}{2}(\Delta E_{tot} = \Delta E_1). \tag{5.5}$$

Now both E_a^1 and E_a^2 can be described by ΔE_1, the Sabatier rate only has one variable ΔE_1. We choose ΔE_1 as the descriptor of the whole reaction.

5.2.2 The Sabatier rate

According to the assumption made in the beginning of Section 5.2, reaction (R_1) reaches maximum when the surface is nearly empty ($\theta_* = 1$,,$\theta_{\text{A}} = 0$), the exact upper bound of reaction rate of (R_1) is:

$$r_1 = k_1^+ p_{\text{A}_2} \theta_* - k_1^- \theta_{\text{A}}^2 = k_1^+ p_{\text{A}_2}. \tag{5.6}$$

While reaction (R_2) takes place with the upper bound of its rate when the surface is filled with atomic A ($\theta_A = 1$), the optimal reaction rate of (R_2) is then

$$r_2 = k_2^+ \theta_{\mathrm{A}} p_{\mathrm{B}} - k_2^- p_{\mathrm{AB}} \theta_* = k_2^+ p_{\mathrm{B}}. \tag{5.7}$$

Since the surface coverage of empty sites and atomic A can not be 1 at the same time, the Sabatier rate for the overall reaction must be bounded by equation 5.6 and 5.7:

$$R = \min\{2r_1, r_2\} = \min\{2k_1^+ p_{\mathrm{A_2}}, k_2^+ p_{\mathrm{B}}\}. \tag{5.8}$$

Plotting the Sabatier rate given by equation 5.8, one gets the volcano plot shown in figure 4.3. Normally the catalytic reactions are more complex, and one descriptor may not be enough for describing the overall reaction. In such cases more descriptors should be chosen and high dimensional volcano plots will be generated.

5.3 Structure sensitivity

Further understanding of the geometric and electronic effect on a full catalytic reaction can be acquired by applying the Sabatier analysis to the reaction. For simplicity, we still consider the two step reaction $\mathrm{A_2(g)} + 2\mathrm{B(g)} \rightleftharpoons 2\mathrm{AB(g)}$ in which a single descriptor, adsorption energy ΔE_1, is needed.

Figure 5.2 shows a classification of structural dependency of a complete catalytic reaction. The BEP lines of the dissociation and desorption steps as well as the corresponding volcano plot from the sabatier analysis are shown. Two different surface sites are considered and shown by the solid and dashed lines. Depending on the structural sensitivity of both elementary steps, the structural sensitivity of the overall reaction can be separated into four cases. The low lying dashed lines can be considered as belonging to a step like defect that give stronger binding to the molecules and intermediates, while the solid line may represent a close-packed surface site. This layout is typical for strongly bound diatomic molecules (*e.g.* NO, O_2, CO and N_2). In general, however, the site preference of the reaction determines the line-ordering.

The arrows in figure 5.2 indicate the shift of the rate over a given metal when going from a close-packed surface site to a stepped surface site which gives stronger binding. For metals that site on the right side of the volcano, shifting to a stronger binding site will always increase the rate, because for these metals, the rate limiting step is the dissociation of reactant. For metals on the left side of the volcano, the rate limiting step is the desorption of the product, hence

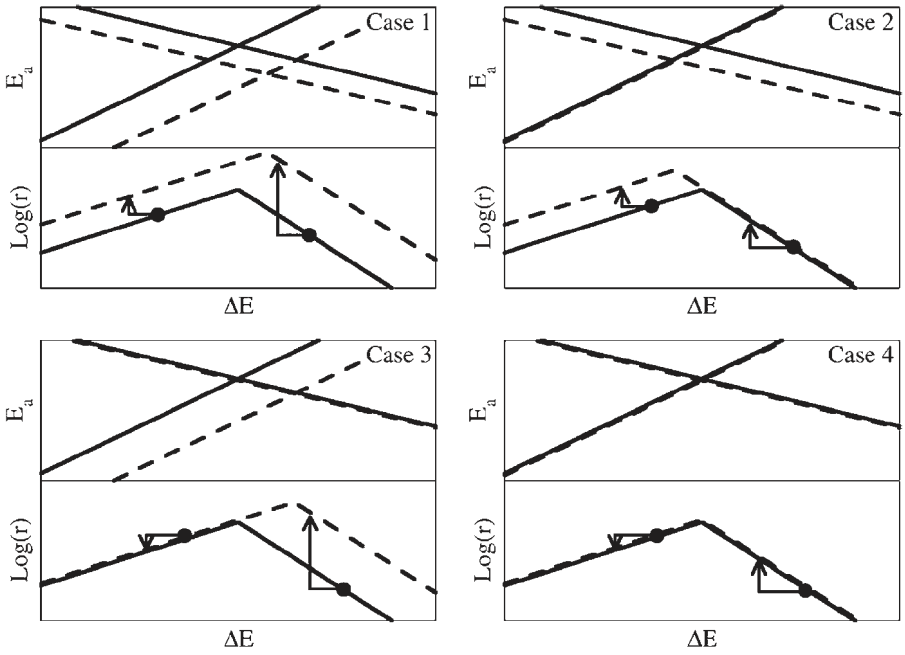

Figure 5.2: Classification of structure dependence for catalytic reactions. The BEP line for dissociation and desorption are shown for two different sites. The corresponding volcano plots are given below. Case 1: both activation and removal exhibit structural dependence. Case 2: only dissociation step is structural dependent. Case 3: only desorption step is structural dependent. Case 4: neither steps are structural dependent. The plot is adapted from [65]

stronger binding to the product will make the desorption even harder and the catalytic rate lower.

Chapter 6

Trends of catalytic activity of CO oxidation on surfaces and nanoparticles

Traditionally, gold was called "the noblest of all the metals"[36]. However, the discovery by Haruta et al. in 1987 showed that nanoparticulate gold is catalytically active for CO oxidation below room temperature. The promoted catalytic activity of gold nanoparticle has been widely debated both experimentally and theoretically, and the discussions mainly focus on charge transfer[73, 75, 28],support interactions[11, 9, 40], surface morphology[59, 57, 33, 80, 52, 88, 20] and quantum size effects[83, 15], however, no consensus about the origin of the nanoeffect has been reached.

Collecting the experimental studies of catalytic activity of gold particles and plotting them against the particle size, Lopez et al.[57] found that the CO oxidation activities at 273K increases significantly when the particle size decreases to less than 5 nm, as shown in figure 6.1. Considering their previous study which shows that the fraction of corner atoms on the surface is proportional to the cube of the average particle size ($\sim d^{-3}$) (shown as the black solid curve in figure 6.1), the finding suggests a strong correlation between the number of under coordinated corner sites and the catalytic activity for CO oxidation of gold nanoparticles.

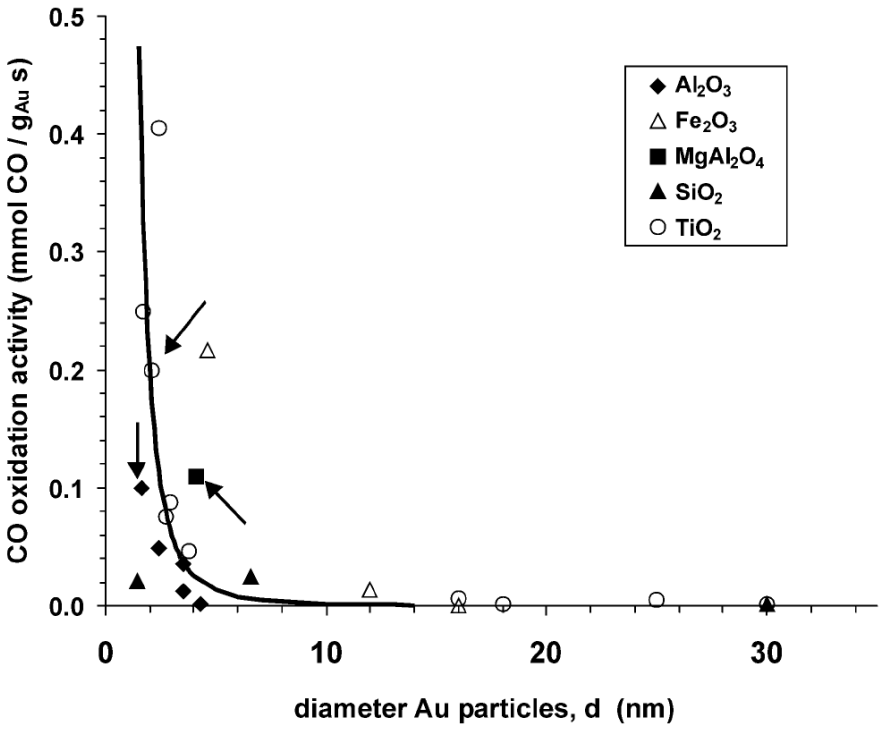

Figure 6.1: Measured activities for CO oxidation at 273 K over different Au-based catalysts as a function of the average particle size. The black solid curve shows the curve of d^{-3} to guide the eye. Adapted from ref. [57], the experimental data in the figure are taken from refs. [39, 10, 33, 32, 76, 79, 41, 51, 54, 67, 87, 77]

6.1 Method

All the total energies have been obtained using the DFT code DACAPO [18]. The Kohn-Sham one-electron valence states were expanded in a plane wave basis set with a 408 eV (30 Ry) kinetic energy cutoff, and a density cutoff of 816 eV (60 Ry). The core electrons were described by Vanderbilt type nonlocal ultrasoft pseudopotentials [84]. The exchange-correlation potential was was described using the RPBE generalized gradient approximation self-consistently. For all surfaces, a $6 \times 6 \times 1$ Monkhorst-Pack k-point sampling was applied in the irreducible Brillouin zone. The occupation of the single electron states was calculated at a temperature of $k_{\mathrm{B}}T = 0.1$eV, and all energies were extrapolated to $T = 0$K.

The (111) surfaces were modeled by (2×2) surface unit cells with slab thicknesses of four layers and the two topmost layers were allowed to fully relax. The

(211) and (532) surfaces were modeled by (2×1) and (1×1) surface unit cells, respectively, with three close packed layer slabs, where only the topmost layer was allowed to relax. For all types of surfaces, the neighboring slabs are separated by more than 10 Å of vacuum. For both cluster structures, Γ point calculations were performed within unit cells with more than 10 Å of vacuum between structures, with a Fermi temperature of $k_{\mathrm{B}}T = 0.01\mathrm{eV}$. All of the atoms in the 12 atom clusters were kept fixed in order to mimic the geometrically constrained corner of a larger particle, with a lattice constant corresponding to the bulk value. On the other hand, the M55 cluster has a realistic nanoparticle structure, so all atomic positions were relaxed.

We have included energy corrections for the adsorption of CO to avoid the overbinding of CO by DFT, which yields lower binding energies on bridge sites than atop sites, in contradiction to experiment [1]. Oxygen adsorption energies are calculated relative to the O_2 energy from H_2O splitting using the experimental reaction energy and that for H_2 and H_2O in the gas phase [66]. This avoids difficulties associated with a DFT treatment of the triplet state of gas phase O_2 [48].

6.2 Microkinetic modeling

In order to calculate the catalytic activity based on adsorption and activation energies from DFT calculation, a simplified microkinetic model will be employed, "Sabatier analysis" will then be used to estimate reaction rates. In this analysis, the coverages of free sites and adsorbed species are assumed optimal for each reaction step, so that the Sabatier rate will be yielded as an exact upper bound of the reaction rate.

We assume the CO oxidation follows Langmuir-Hinshelwood type mechanism, the reaction can hence be described by the following elementary steps:

$$\begin{aligned}
&(\mathrm{R1})\mathrm{CO} + * \rightleftharpoons \mathrm{CO}* \\
&(\mathrm{R2})\mathrm{O_2} + * \rightleftharpoons \mathrm{O_2}* \\
&(\mathrm{R3})\mathrm{O_2} * + * \rightleftharpoons 2\mathrm{O}* \\
&(\mathrm{R4})\mathrm{CO} * + \mathrm{O}* \rightleftharpoons \mathrm{CO_2} + 2* \\
&(\mathrm{R5})\mathrm{CO} * + \mathrm{O_2}* \rightleftharpoons \mathrm{CO_2} + \mathrm{O} * + *
\end{aligned}$$

Here we assume that the adsorption elementary steps (R1) and (R2) reach equilibrium quickly, meaning that the net rate $r_1 \approx r_2 \approx 0$. According to the assumptions of Sabatier analysis, the rates of elementary reactions (R3)-(R5)

maximize, and hence:

$$r_3 = \theta_{O_2}\theta_* k_3^+, \tag{6.1}$$

$$r_4 = \theta_O\theta_{CO}k_4^+ \approx \theta_{CO}k_4^+, \tag{6.2}$$

$$r_5 = \theta_{O_2}\theta_{CO}k_5^+, \tag{6.3}$$

where θ_{CO}, θ_{O_2}, θ_O and θ_* are the coverages of CO, O_2, O and free surface sites respectively. The rate constant k_i for the elementary reaction step, i, is given by

$$k_i = \nu_i \exp[\frac{-\Delta G_{ai}}{k_B T}] \tag{6.4}$$

$$= \nu_i \exp[\frac{-(E_{ai} + \Delta ZPE_{ai} - T\Delta S_{ai}}{k_B T} \tag{6.5}$$

where ν_i is the prefactor, E_{ai} is the activation barrier for the reaction, ΔZPE is the zero-point energy change, ΔS_{ai} is the entropy change, k_B is the Boltzmann constant, and T is the temperature. The prefactors are assumed to be metal independent, so that $\nu_i = k_B T/h$, and the change in zero-point energy is negligible compared to the activation barrier ($\Delta ZPE_{ai} \ll E_{ai}$). The entropy of adsorbed species is assumed to be much smaller than that in the gas phase, so that $\Delta S_{ai} \approx \mp S_{gas}$ for adsorption/desorption, where gas phase entropies are taken from ref. [3].

Overall, the Sabatier rate for CO_2 production is the sum of the rates for reactions R4 and R5. However reaction R4 is limited if no atomic oxygen is present from reactions R3 or R5. On the other hand, reaction R5 will be limited by a poisoning by atomic oxygen of the catalyst, and can therefore not be faster than reaction R4. Hence the overall reaction rate according to the Sabatier analysis is then

$$r_S = \max\{2\min\{r_5^+, r_4^+\}, \min\{2r_3^+, r_4^+\}\} \tag{6.6}$$

As reaction steps (R1) and (R2) are assumed to be in equilibrium, the coverages of CO and O_2 satisfy $\theta_{CO} = K_1 p_{CO}\theta_*$ and $\theta_{O_2} = K_2 p_{O_2}\theta_*$. Considering the conservation of surface sites ($\sum \theta_x = 1$) the coverage of unoccupied adsorption sites is written:

$$\theta_*^{max} = \frac{1}{1 + k_{1p_{CO}} + K_2 p_{O_2}}. \tag{6.7}$$

Here we neglected the coverage of surface oxygen coverage, which provides upper bounds for the respective coverages.

For the close packed 111 surfaces, reaction (R5) is neglected, since the binding of O_2 on platinum and less reactive metals is weak. In this case, reaction (R4)

is the only one that produces CO, and the Sabatier rate is the minimum of the rates of reaction (R3) and (R4):

$$r_{\mathrm{s}} = \min\{2r_3, r_4\}. \tag{6.8}$$

6.3 Results

In this section we present a study of CO oxidation both on close packed surface and a 12-atoms model (M12) of a large nanoparticle for a number of transition metals. We show the scaling relation between adsorption energies, and between adsorption energies and transition state energies (the BEP relation), the linear relations are used to reduce the number of variables that affect the overall reaction rate. Then we show how to construct a volcano plot with the independent variables acquired. The volcano plot shows that platinum is the most active metal at high temperature while at low temperature, gold nanoparticle is the most active catalyst in all the metals considered.

6.3.1 Scaling relations

From the microkinetic modeling we know that the rate of CO oxidation reaction is a function of E_{CO}, E_{O}, $E_{\mathrm{O_2}}$, E_{TS3}, E_{TS4} and E_{TS5}, for close packed 111 surfaces, only the first 4 parameters are needed to describe the reaction rate. We begin by studying trends of these energies. In Figure 6.2 we show scaling relations between different adsorption energies and between activation energies and adsorption energies (BEP relations) for both 111 surfaces and M12 clusters of a series of metals.

The linear relations shown in figure 6.2 mean that of the original six metal-dependent variables (E_{CO}, $E_{\mathrm{O_2}}$, E_{O}, E_{TS3}, E_{TS4}, and E_{TS5}) only two are independent. We choose for these two independent variables E_{CO} and E_{O}. We may thus calculate the Sabatier rate for CO oxidation as a function of these two parameters alone for each of the structures studied. This means that we rely on the linear relations in figure 6.2 in the kinetics. These relations are not exact, but they clearly describe the trends for metals and structures. We suggest that this provides a good basis for a study of trends in the catalytic activity.

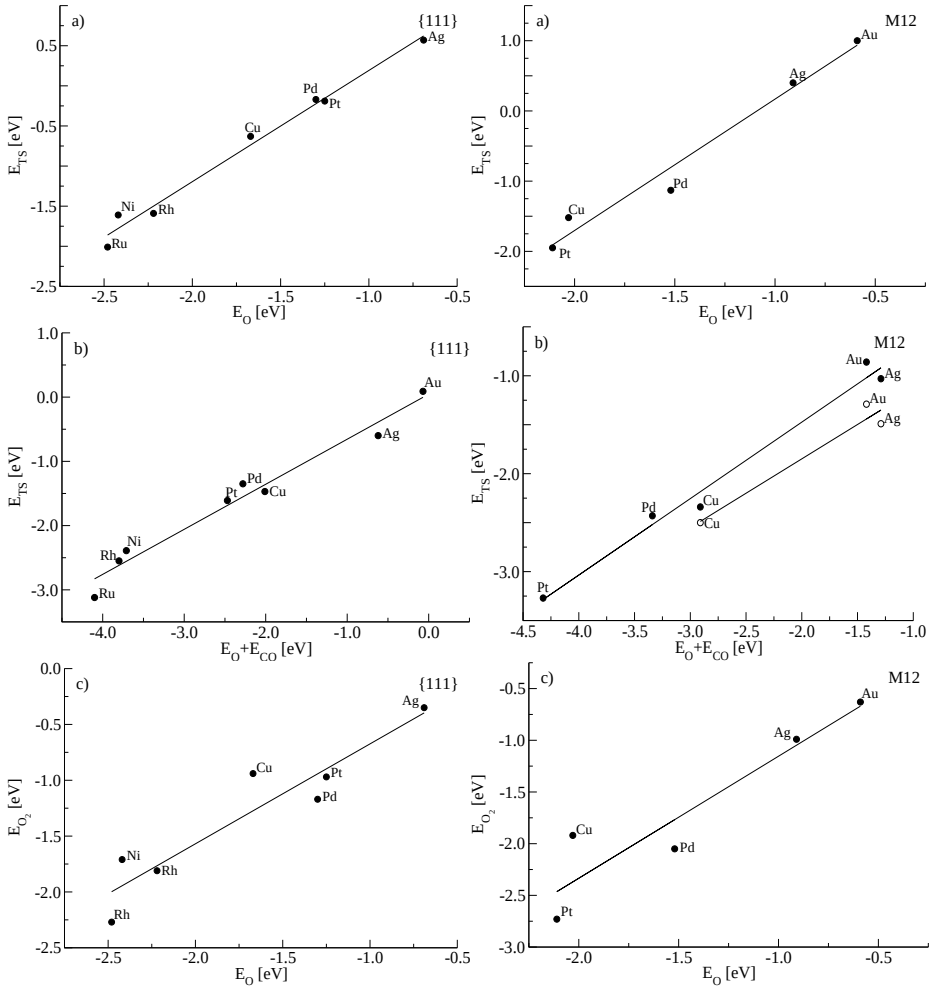

Figure 6.2: The scaling and BEP relations for 111 surfaces and M12 clusters. a) Calculated transition-state energies for adsorbed O_2 dissociation (R3) as a function of oxygenadsorption energy. b) Calculated transition-state energies for adsorbed CO reacting with adsorbed O (R4) and O_2 (R5) as a function of the sum of the O and CO adsorption energies. $E_{\mathrm{O}} + E_{\mathrm{CO}}$. c) The scaling of the O_2 adsorption energy with the O adsorption energy.

6.3.2 Volcanoes

Due to the linear scaling relations of the energies, it is reasonable to assume the overall reaction rate only depend on the adsorption energies of CO and O (E_{CO} and E_{O}), a two dimensional volcano plot can be constructed based on equation (6.8) for close packed surfaces and equation (6.6) for M12 clusters.

We show first a contour plot of the Sabatier activity over close-packed surfaces in figure 6.3. The Sabatier rate is calculated at T=600 K, $p_{\mathrm{O_2}}$=0.33 bar and p_{CO}=0.67 bar, corresponding to high-temperature CO oxidation conditions. The Sabatier activity is given as

$$A_{\mathrm{s}} = k_{\mathrm{B}}T\ln[\frac{r_{\mathrm{s}}h^{-1}}{k_{\mathrm{B}}T}], \tag{6.9}$$

where r_{s} is the Sabatier rate.

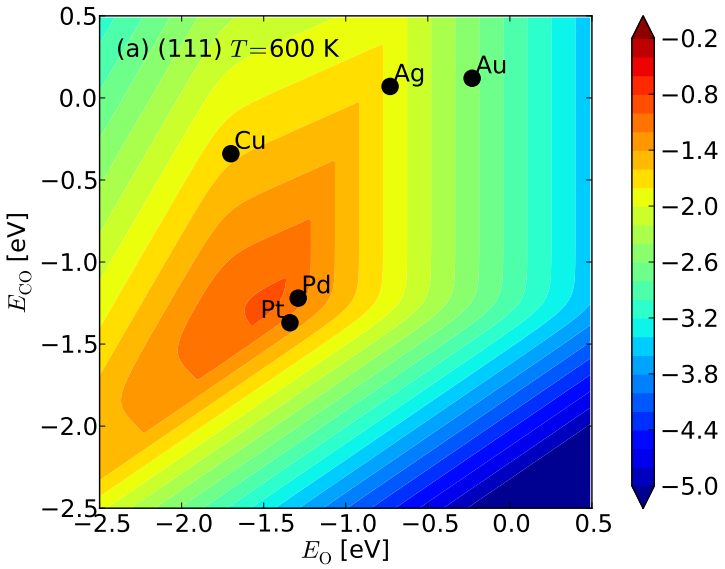

Figure 6.3: Contour plot of the Sabatier rate as a function of the CO and O adsorption energies on close packed 111 surfaces at high-temperature CO oxidation condition.

The two-dimensional volcano plots show that, of the elemental metals, platinum and palladium are closest to the top, which agrees well with experimental evidence [60]. Platinum and palladium are excellent CO oxidation catalysts, used for example in car exhaust after-treatment. Our result is also completely in line with DFT calculations and kinetic modeling by Grabow et al.[31] showing

that at low temperatures, platinum without strain has a higher activity than either compressed (weaker bond energies) or expanded (stronger bond energies) platinum surfaces.

We then investigate the reactivity of nanoparticles. As we mentioned before, there is a large fraction of low-coordinate corner atoms to surface atoms on nanoparticles, it is therefore safe to focus on the reactivity of corner atoms, and model these by carrying out calculations for metal clusters containing twelve atoms. The corresponding structure is shown in figure 6.5d . Sabatier activity for CO oxidation on M12 clusters are presented in figure 6.4. We see that when reaction occurs at low temperature condition (T = 273K, P_{O_2} = 0.21bar and P_{CO} = 0.01bar), gold nanoparticle sits on the top of the volcano, followed by palladium and silver.

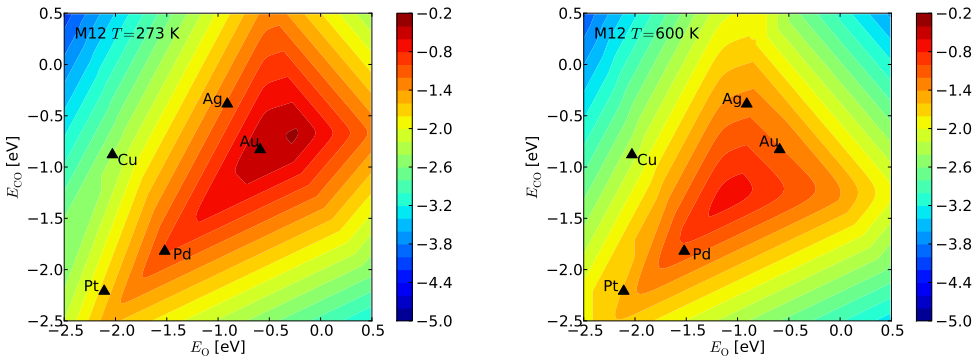

Figure 6.4: Contour plot of the Sabatier rate as a function of the CO and O adsorption energies both on 12-atom clusters.

Combining figure 6.3 and 6.4 we find that the position of the maximum in terms of adsorption energies depends slightly on the structure, which is related to the fact that the relationship between adsorption energy and activation energy is somewhat structure dependent. More importantly, for all the metals considered it can be seen that the metals corresponding to a particular adsorption energy shift substantially depending on the coordination number of the metal atom, and it is the dominant reason for gold becoming the best elemental catalyst for the low-coordinate sites. The shift is of the same order of magnitude as the difference between neighboring metals in the periodic table, explaining why it appears as if the top of the volcano has shifted by a little less than one place to the right in the periodic table from Figure 6.3 to Figure 6.4.

Taking a close look at the Sabatier activity in figure 6.3 and 6.4, we see that changing from close packed surface to nanoparticle, the Sabatier rate increases many orders of magnitude, suggesting that even for large gold particles the

corner atoms will dominate over the close-packed facets on the particle. While for platinum, the difference of Sabatier rate is only about an order of magnitude. We should point out that for platinum, small particles could still be more active as the per mass surface area is much larger (scaling as d^{-1}).

The above analysis suggests that less reactive metals which locate at the top right corner of the pinnacle may move to the maximum in the reactivity volcano when lower-coordinated metal atoms becomes dominant of the active sites. If a reaction involves less reactive molecules, such as N_2, we would expect that the best nanoparticle catalysts would be metals just to the right in the periodic table of the most active metals (ruthenium, iron) for this reaction, for example, cobalt or nickel. It is therefore possible that pronounced nanoeffects in catalysis is not restricted to gold.

6.4 A complete picture of catalytic activity dependence on surface structure

Previously we presented how to estimate the trend of catalytic activity of CO oxidation by combining DFT energetics and microkinetic modeling. We showed that for CO oxidation, changing from close packed surface to under-coordinated corner model, gold binds reactants significantly stronger, which further results in a orders of magnitude increase of reaction rate at low temperature (273 K).

We now include the stepped and kinked surfaces, to give a systematic study of catalytic activity of a series of surfaces/clusters with a gradually decreased coordination number of the active sites, as shown in figure 6.5. To describe the influence of decreasing size on adsorption energies we have used a “magic size” 55 atom cuboctahedral cluster model,which for both Au and Pt, have been found experimentally[2, 85, 82]. We use again the well studied CO oxidation as model reaction to give a complete picture of effect of surface structure on catalytic activity.

6.4.1 Scaling relations

The scaling relations obtained for CO oxidation reaction on different surfaces of transition and noble metals are shown in figure 6.6. In general, the data falls into families of linear relations, with one approximately linear relation for each structure of the catalyst. The differences in the lines reflect the structure-dependence of the different adsorption energies and reaction barriers. For O_2 dissociation

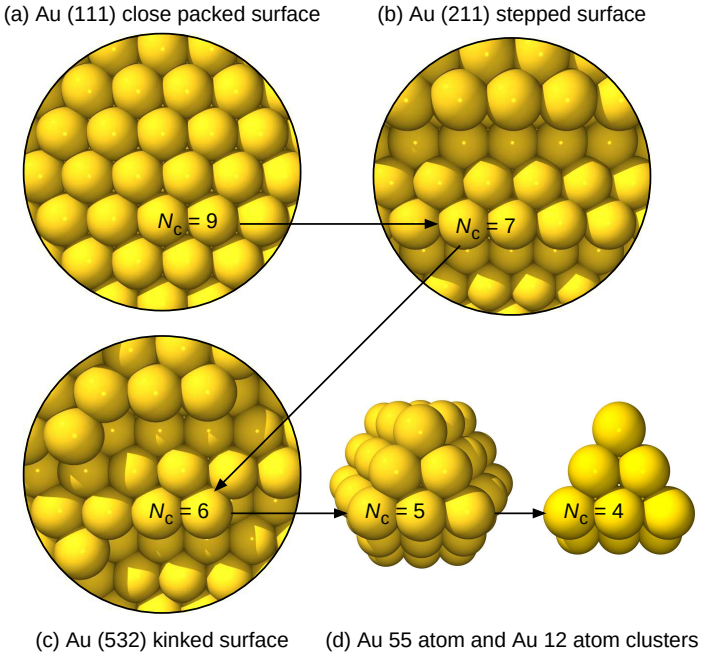

Figure 6.5: Structural schematics and lowest coordination number N_c for the (a) Au(111) close-packed surface, (b) Au(211) stepped surface, (c) Au(532) kinked surface and (d) Au 55-atom cuboctahedral cluster and Au 12-atom cluster corner model.

reaction (figure 6.6b), the BEP lines for (211) and (532) surfaces are close to each other, but far from that of (111) surface. It is easily understandable since the dissociations of O_2 on (211) and (532) both benefit from the B5 sites which have 5 metal atoms stabilizing the molecular transition state. For the CO+O and CO+O_2 reaction the different BEP lines are nearly indistinguishable. This implies that geometrical effects may be neglected. Note that even if there is only one BEP line for a particular elementary reaction for all structures, there are still large differences in the adsorption and hence the activation energy for a given metal from one structure to the next. For instance, for Au the CO adsorption energy varies by ≈ 1.0 eV from the (111) surface to the M12 cluster. The linear relations suggest again that only two independent variables E_{CO} and E_O are needed to describe the overall reaction rate.

6.4.2 Volcanoes

Figure 6.7a-d shows the Sabatier activity $A_S = k_B T \ln\left(r_S / k_B T h^{-1}\right)$ as a function of the adsorption energies of CO and O for the close-packed (111), stepped

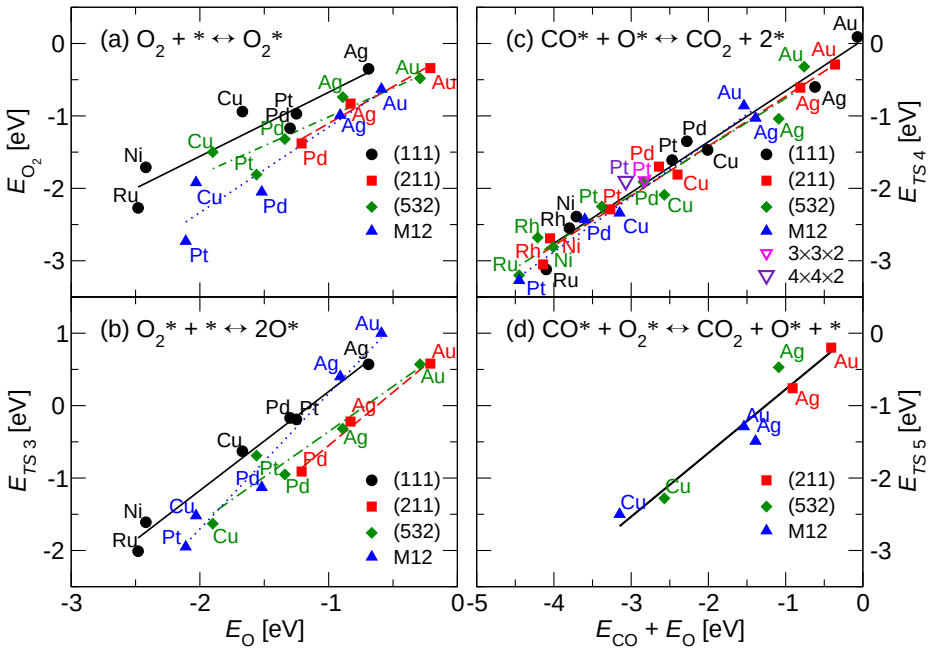

Figure 6.6: The scaling and BEP relations for (111)-surfaces (•,—), (211)-surfaces (■,– – –), (532)-surfaces (♦,– · – ·), and M12-clusters.(▲,· · · · · ·) (a) The scaling of the O_2 adsorption energy E_{O_2} with the O adsorption energy E_O. (b) Calculated transition state energies for O_2 dissociation E_{TS3} (R3) as a function of O adsorption energy E_O. (c) Calculated transition state energies for adsorbed CO reacting with adsorbed O E_{TS4} (R4) as a function of the sum of the O and CO adsorption energies, E_O and E_{CO}. Results for the Pt 3×3×2 slab (▽) and Pt 4×4×2 slab (▽) model are provided for comparison. (d) Calculated transition state energies for adsorbed CO reacting with adsorbed O_2 E_{TS5} (R5) as a function of the sum of the O and CO adsorption energies, E_O and E_{CO}, with surface averaged BEP relation (—).

(211), and step-kinked (532) surfaces as well as for the M12 cluster. Note that comparing to volcanoes of (211), (532) sufaces and M12 cluster, the volcanoes of (111) surfaces don't have the shoulder on the right side of the volcanoes and the overall reaction rates on (111) surfaces are about 1 order of magnitude lower than other volcanoes. These differences are due to the missing of elementary step (R5) since O_2 adsorption is weak on close packed surfaces. In particular, the position of the maximum in terms of E_{CO} and E_O hardly changes from one structure to the next. One reason for this structure independence is related to the relevant energy scale. It may be seen in figure 6.7 that the maxima are quite broad. The width of the maximum, defined as the width of the contour where the rate is one order of magnitude lower than the maximum, is on the order of 0.5 eV. This gives a certain insensitivity of the results to the details of the

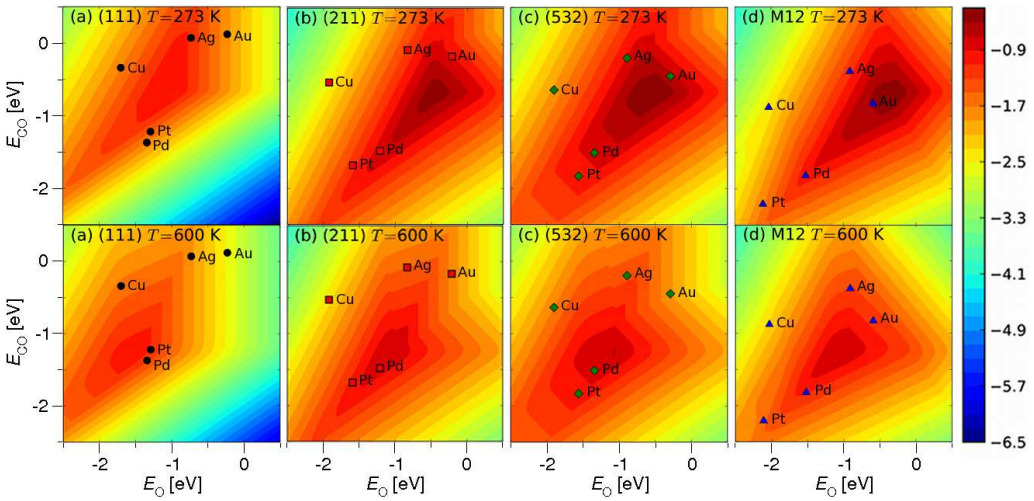

Figure 6.7: Contour plot of the Sabatier activity $A_S = k_B T \ln\left(r_S/k_B T h^{-1}\right)$ in eV at (top) low temperature ($T = 273$ K, $p_{O_2} = 0.21$ bar, $p_{CO} = 0.01$ bar) and (bottom) high temperature ($T = 600$ K, $p_{O_2} = 0.33$ bar, $p_{CO} = 0.67$ bar), as a function of the CO and O adsorption energies on the (a) (111)-surfaces (●), (b) (211)-surfaces (■), (c) (532)-surfaces (♦), (d) M12-clusters (▲). The values for several elemental metals are shown. The activity is calculated under typical experimental conditions for gold nanoparticles.

energetics. An other reason is when oxygen adsorption energy is low, reaction (R5) dominates over (R3), since there is only electronic effect on reaction (R5), the shape of the volcano should remain the same.

For each structure we have shown in 6.7, the position of the different metals is defined by their (E_{CO}, E_O) coordinate. It should be observed that the Au point moves closer to the maximum in the order (111)→ (211)→(532)→(M12), while the Pt and Pd points move away in the same order. This is made even clearer in 6.8, where we show how the (E_{CO}, E_O) points for different structures wander on an average of the different volcanoes. Here we have also added (E_{CO}, E_O) for the Pt55 and Au55 clusters. They clearly agree very well to the same trends.

Summing up the above analysis, we conclude that the rate of CO oxidation is clearly a function of the local geometry. At low temperature condition, the calculated rates on Au steps, kinks and small particles are higher than that of close packed surface, as shown in figure 6.7. This is in good agreement with experimental observations. Our calculation suggest that there is an intrinsic size dependence relating to the availability of the most reactive structures involving low-coordinated Au atoms. For the other metals the size dependence also exist. For Pd and Pt the trend is that the intrinsic activity decreases with decreasing

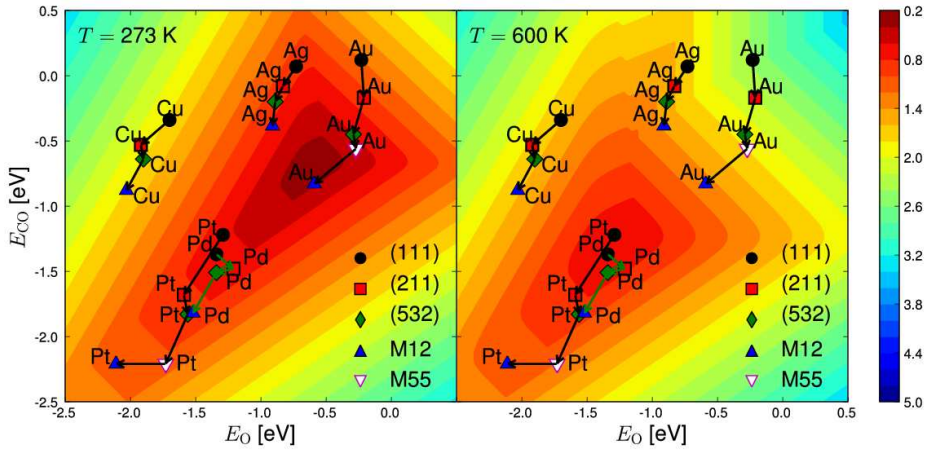

Figure 6.8: Contour plot of the "average" Sabatier activity $A_S = k_B T \ln\left(r_S/k_B T h^{-1}\right)$ in eV at (top) low temperature ($T = 273$ K, $p_{O_2} = 0.21$ bar, $p_{CO} = 0.01$ bar) and (bottom) high temperature ($T = 600$ K, $p_{O_2} = 0.33$ bar, $p_{CO} = 0.67$ bar) from 6.7 as a function of the CO and O adsorption energies on (111)-surfaces (●), (211)-surfaces (■), (532)-surfaces (♦), M12-clusters (▲), and M55-clusters (▽). The values for several elemental metals are shown. The activity is calculated under typical experimental conditions for gold nanoparticles.

particle size. At higher temperatures the CO oxidation rate is largest on these metals. The increased temperature shifts the top of the volcano to stronger adsorption energies, hence in the direction of the platinum. Such effects have been observed both experimentally and theoretically[72, 5, 34, 43]. The effect of local geometry on the reactivity per site is weak, but the reaction rate may still increase as the particle size decreases due to the increase of surface area per unit mass of catalyst. We note that the main effect behind the structure variation is not geometrical since the volcanoes for different structures are not very different. It is rather the variation of bond strength of the different adsorbates as the structure is changed.

6.4.3 Electronic effects

According to the previous analysis, the structure induced change in the intrinsic catalytic activity for CO oxidation on a number of metals is not due to the geometric effect. It should be the electronic structure changes that effected the adsorbate-surface interactions, which further change the catalytic activity.

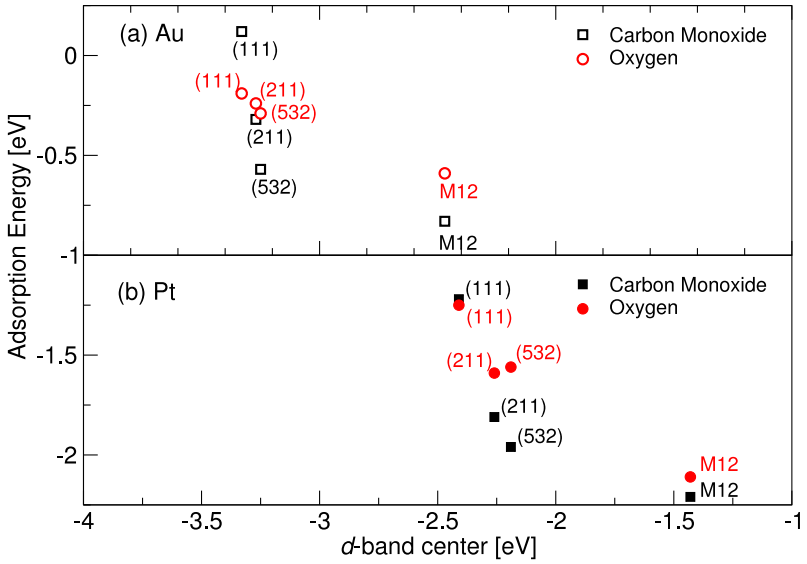

Figure 6.9: Adsorption energy E_{CO} and E_O versus d-band center for (111)-surfaces, (211)-surfaces, (532)-surfaces and M12-clusters of (a) Au (□, ○)and (b) Pt (■, ●).

In figure 6.9 we show the adsorption energy of O and CO plotted against the d-band center of the atoms on the active sites. According to the d-band model mentioned in chapter 4 the strength of the adsorption bond should increase as the d states are shifted up in energy. The results illustrate the simple rule of thumb that the lower the metal coordination number, the higher the d states are in energy, and the stronger they interact with adsorbates.

6.5 Comparison with experimental results

In this section comparison with experimental results on CO oxidation is presented. N_2O is chosen experimentally as one of the oxidation agent since N_2O is known to readily dissociate into adsorbed atomic O and gas phase N_2 in the presence of CO, the oxidation of CO by N_2O involves atomic O.

6.5.1 Experimental results

CO oxidation both by N_2O and O_2 were performed on three gold catalysts with different particle sizes (2.0 nm, 3.3 nm and 5.0 nm) supported on TiO_2. Detailed description of the preparation of the catalysts and the microreactors can be found in Paper 2.

Table 6.1: Apparent activation energies in kJ·mol^{-1} for CO and H_2 oxidation by O_2 and N_2O, with an uncertainty of ± 2 kJ·mol^{-1}. Theoretical values obtained using the microkinetic model in the low temperature regime are also provided in parentheses for Catalyst A.

E_a(kJ·mol^{-1})	Catalyst A	Catalyst B	Catalyst C
CO+1/2O_2	36 (36.4)	38	60
CO+N_2O	37 (37.5)	40	60

Figure 6.10a shows Arrhenius plots for (R1) and (R2) on Catalyst A. For both reactions, the activation energies obtained were all approximately 37 kJ·mol^{-1}, as may be seen from the parallel linear fits. Table 6.1 summarizes these and the following activation energies. However, when comparing the different oxidation agents with each other, CO oxidation the reaction rate differs by a factor of 2.7.

For CO oxidation by O_2 on Catalyst B, the reaction rate was found to reach a maximum at about 80 °C, cf. figure 6.10b. One reason for this may be due to CO or O_2 desorption. Despite this, the parallel running fits of the Arrhenius plots again indicate similar activation energies of around 39 kJ·mol^{-1}, as shown in table 6.1. On the Au particles of Catalyst B, which were sintered to 5.7 nm, the trend depicted on Catalyst A continues, but is even more distinct, as shown in figure 6.10b. There is approximately one order of magnitude between the rates of CO oxidation using N_2O and O_2.

These two catalysts where active even at room temperature, although O_2 was a significantly better oxidizing agent. For (R1), N_2 released from N_2O could be balanced with the CO_2 formed, indicating that the CO_2 does not originate from other sources.

Arrhenius plots for Catalyst C is shown in Figure 6.10c. To the contrary of Catalyst A and Catalyst B, N_2O is the better oxidizing agent for CO. A very similar apparent activation energy of about 60 kJ·mol^{-1} was again found for both reactions. On these large particles an onset of conversion could not be observed below 80 °C.

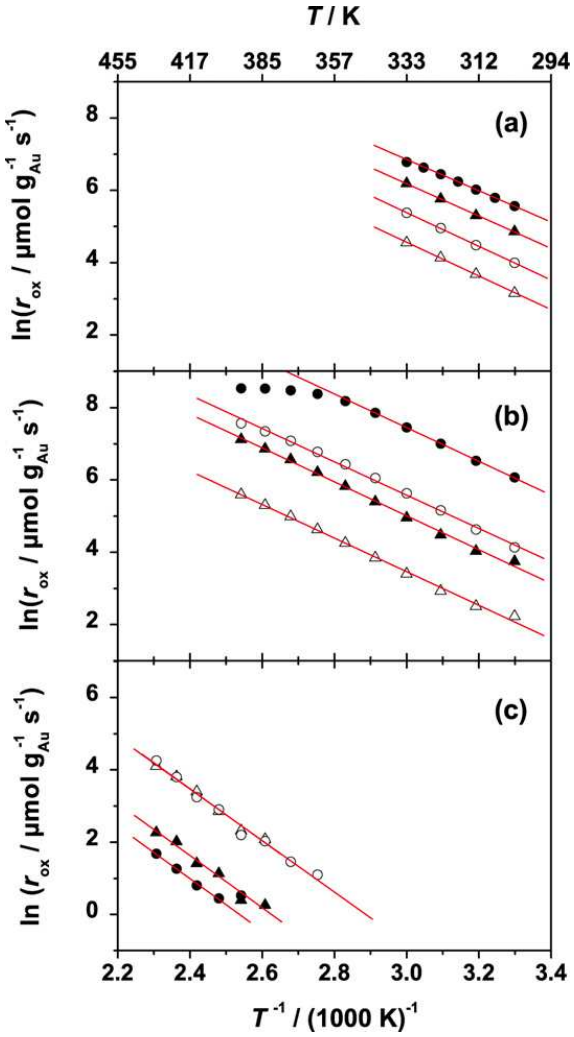

Figure 6.10: Arrhenius plots of the activation energies for the four reactions on TiO_2 supported gold particles of Catalyst A (a), Catalyst B (b) and Catalyst C (c): CO + 1/2 O_2(•), CO + N_2O (▲). An overview of the activation energies is given in table 6.1

6.5.2 Theoretical results

The overall oxidation reactions using two different oxidizing agents O_2 and N_2O are:

$$\text{(R1)} CO + N_2O \rightleftharpoons CO_2 + N_2$$
$$\text{(R2)} CO + 1/2O_2 \rightleftharpoons CO_2$$

We begin by first considering CO oxidation using N_2O. It has been generally accepted that the reaction kinetics for CO oxidation over a metal surface follow the Langmuir-Hinshelwood mechanism. According to this, the elementary steps of adsorption and desorption are assumed to be in equilibrium, reaction (R1) can then be written in terms of the following elementary steps:

$$\text{(R1a)} CO(g) + * \rightleftharpoons CO*,$$
$$\text{(R1b)} N_2O(g) + * \rightleftharpoons N_2O*,$$
$$\text{(R1c)} CO* + N_2O* \xrightarrow{rds} CO_2(g) + 2*.$$

Adsorption steps (R1a) and (R1b) are assumed to be in quick equilibrium, and oxidation step (R1c) is considered as the rate determing step. In our experimental study, we found N_2 does not dissociate spontaneously on gold, as has also been reported by Gluhoi et al.[29], we assume this reaction requires adsorbed CO as a reducing agent. However, the overall barrier should still be the same as for CO oxidation with atomic O. On the other hand, the desorption of both N_2 and CO_2 should occur spontaneously.

To model the corner sites of a gold nanoparticle for reaction (R1c), we have chosen a Au (532) surface, which consists of both B5 and kink sites. This allows atomic O to adsorb on the preferred B5 sites while CO adsorbs on the kink sites. This is depicted in the Au (532) transition state for (R1c), shown in the lower inset of Fig. 4. Since the Au12 corner model does not include B5 sites for atomic O adsorption, it yields an activation barrier for (R1c) twice that found for the Au (532) surface. For this reason, the Au12 model should not be used to model (R1c).

By employing microkinetic modeling, the turnover frequency for the rate determining step (rds) f_{rds} in s^{-1}, may be approximated by

$$f_{\mathrm{rds}} \approx \frac{k_B T}{h} \frac{K_{CO*} K_{N_2O*} p_{CO} p_{N_2O}}{(1 + K_{CO*} p_{CO})(1 + K_{N_2O*} p_{N_2O})} \exp[-\frac{E_a[\mathrm{rds}] - T(S_{CO_2(g)} + S_{N_2(g)})}{RT}], \tag{6.10}$$

where K_{CO*} and K_{N_2O*} are equilibrium constants of CO and N_2O adsorptions. The temperature dependent gas phase entropies are interpolated using data from Ref. [53].

When using O_2 as oxidizing agent for CO, based on the study in section 3.4, the overall rate depend mainly on the $CO + O_2$ elementary step, the elementary steps for (R2) can be simplified to

$$\begin{aligned}
&(\text{R2a})\text{CO(g)} + * \rightleftharpoons \text{CO}*,\\
&(\text{R2b})\text{O}_2\text{(g)} + * \rightleftharpoons \text{O}_2*,\\
&(\text{R2c})\text{CO}* + \text{O}_2* \xrightarrow{rds} \text{CO}_2* + \text{O}*,\\
&(\text{R2d})\text{CO}* + \text{O}* \Rightarrow \text{CO}_2\text{(g)} + 2*.
\end{aligned}$$

Here we note that to enable reaction (R2d), the existence of surface adsorbed atomic O is needed, which means that reaction (R2d) can not be faster than reaction (R2c), making (R2c) the rate determining step.

To model the gold nanoparticle corner sites for reaction (R2c), the Au12 cluster model from Chapter 5 is used. We see from figure 6.6a that O_2 adsorption energy is much higher on Au12 cluster than on Au (532) surface. This is necessary to correctly model (R2c) on gold nanoparticles. As shown in the upper inset of figure 6.11, the transition state for (R2d) on the Au12 cluster model has the O_2 molecule strongly adsorbed on the corner site, while CO is adsorbed on the edge.

Again employing microkinetic model, f_{rds} for (R2) may be approximated by

$$\begin{aligned}
f_{\text{rds}} \approx & \frac{k_B T}{h} \frac{K_{O_2*} K_{CO*} p_{CO} p_{O_2}}{(1 + K_{O_2*} p_{O_2})(1 + K_{CO*} p_{CO})} \\
& \exp[-\frac{E_a[\text{rds}] - T S_{CO_2(g)}}{RT}],
\end{aligned} \tag{6.11}$$

where K_{O_2*} is the equilibrium constants of O_2 and the temperature dependent gas phase entropies are interpolated using data from Ref. [53].

The DFT energies for the adsorbed species as well as the activation barriers are given in Table 1. For the N2O adsorption energy, we have used the experimental value given in Ref. [61].

Plugging the calculated adsorption energies and activation energies in to equation 6.10 and 6.11, we get the temperature dependence of the turnover frequency f_{rds}, for the rds of CO oxidation by N_2O on Au (532) and on Au12 cluster, as shown in figure 6.11. It is found that f_{rds} for CO oxidation by N_2O on Au(532) follows an Arrhenius-like behavior in the low temperature regime ($T < 350$ K).

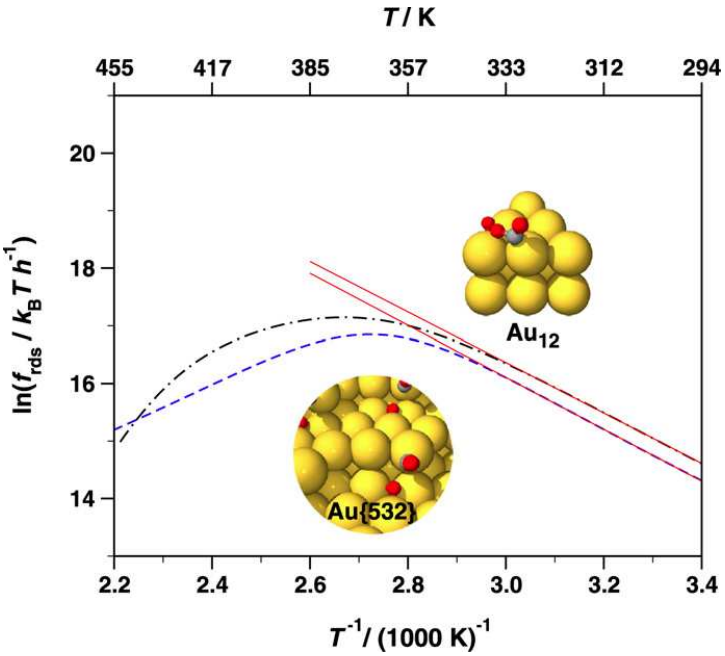

Figure 6.11: Arrhenius plot of the rds turnover frequency f_{rds} in $k_{\mathrm{B}}T/h \approx 10^{13}$ for CO oxidation by N_2O on Au (532) (blue dashed line) and by O_2 on a Au12 cluster (black dash-dotted line) as obtained from the microkinetic model using the DFT transition state structures depicted in previous section.

However, at higher temperatures the turnover frequency decreases with increasing temperature, with an apex at $T \approx 360$ K. For CO oxidation by O_2 on Au12, the Arrhenius behavior of f_{rds} in the low temperature regime ($T < 350$ K) was also found. An apex at $T \approx 370$ K of the turnover frequency is observed as temperature increases.

6.5.3 Discussion

The activation energies for the reactions measured on Catalysts A, B and C shown in table 6.1 show clear size dependence trend from large gold particles with less reactivity to the significantly more reactive smaller ones for both reactions studied. There is very little difference in the apparent overall activation barrier for CO oxidation, irrespective of the oxidizing agent used. This is seen for both experimental and theoretical apparent activation barriers, which are in quantitative agreement for Catalyst A ($d < 5$ nm), in the low temperature regime ($T < 350$ K), as shown in table 6.1. For larger Catalyst C ($d < 10$ nm), however, little correlation between the experimental reaction rate and theoret-

Table 6.2: Activation barriers E_a and adsorption energies E_{ads} in eV for CO oxidation by N_2O and O_2.

E(eV)	Au(532) surface	Au12 cluster
$E_{ads}[O_2]$	-0.28	-0.63
$E_{ads}[CO]$	-0.77	-0.95
$E_{ads}[N_2O]$	-0.08*	-0.08*
$E_a[CO+O_2 \rightarrow CO_2+O$	-	0.28
$E_a[CO+O \rightarrow CO_2$	0.28	-

*Ref. [61]

ical turnover frequency were found. This may be expected, as for larger Au nanoparticles ($d < 10$ nm), the bulk gold properties may begin to dominate, so that a cluster-based theoretical model is no longer applicable. A direct comparison between measured rates and calculated turnover frequencies requires atomic resolution characterization of the particles in question. Given the large dispersity in particle size for our catalysts we are unable to provide such experimental detail. However, it should be born in mind that the trends for the theoretical turnover frequency should match those of the experimental rate, as shown in Table 3.

First focusing on CO oxidation using N_2O according to (R1). From the preliminary investigations it may be concluded that in the absence of a reducing agent, the dissociation of N_2O is inhibited. This may be accounted for by the very weak Au-N_2O bond which leads to rapid desorption of N_2O [29]. However, since one diatomic and one triatomic species both adsorb and desorb from the surface in (R1), this reaction changes the overall entropy of the system only slightly. This means that although there is only a small N_2O coverage, for high CO coverage experiments the reaction rate should be significant. When temperature gets higher ($T > 350$ K) CO begins to desorb from the surface and the turnover frequency begins to decrease, as seen in figure 6.11. It is however unable for us to verify this experimentally since gold particle sintering began to occur in this temperature range.

For the case of CO oxidation by O_2 however, there is a significant loss of entropy in the overall reaction, as three diatomic species adsorb, but two triatomic species desorb. High O_2 adsorption energy is required for the reaction rate to be significant. As this is the case for small gold nanoparticles and the Au12 cluster model for a corner site, we employ this model for (R2). Even so, we find at higher temperatures ($T > 370$ K) the reaction rate decreases significantly as both O_2 and CO begin to desorb from the gold nanoparticle. This may be seen in the reaction rate plots for CO oxidation by O_2 on Catalyst B, shown in figure 6.10. Here, the reaction rate begins to flatten at about 370 K, in agreement

with the theoretical turnover frequency shown in figure 6.11.

6.6 Conclusion

In this chapter, the trend of catalytic activity of CO oxidation over a range of metal surfaces was studied by combining DFT and microkinetic modeling. The linear relations between different adsorption energies and between activation energiew and adsorption energies were shown. The number of variables of the overall reaction was reduced down to only adsorption energies E_{O} and E_{CO}. By studying different close-packed, stepped and kinked surfaces, as well as very small clusters, we have shown that the main difference in catalytic activity between different surface geometries is related to the "openness" of the surface. More precisely, the coordination number of metal atoms at active sites provides this structure dependence. By including the stepped and kinked surfaces, we have filled the gap between close packed surfaces and nanoparticles discussed in ref 35. Further, the activity is found to be a quasicontinuous function of the openness of the surface. We have also provided detailed evidence that this effect is electronic in nature: the low coordinated metal atoms that bind the reactants most strongly have the highest energy metal d states.

More specifically, we found the CO oxidation reaction rate catalyzed by gold increases as the coordination number of surface gold atoms decreases. The finding agrees with the observed high CO oxidation reactivity of gold nanoparticles, however, other effects such as charge transfer, metal- support interactions and quantum size effect merits further discussion.

Finally, CO oxidation by N_2O and O_2 were studied and compared with experiments. Although the two oxidizing agents used proceeded via different reaction pathways on different active sites (kink defect sites and B5 sites), the apparent overall activation barriers were found to be the same and agree well with the experiment on small gold nanoparticles below 5 nm.

Chapter 7

Tuning Au Surface Chemistry with Heterometals

Gold nanoparticles (NPs) are now well established as important nanoscale building blocks and are being examined for a wide variety of applications in nanotechnology and nanomedicine[8]. Besides CO oxidation studied extensively and also in Chapter 6, Au NPs have also been shown to have outstanding catalytic activity and selectivity for other oxidation reactions[42, 17]. Given the broad, general interest in Au NPs, there is a substantial need for fundamental studies to expand and tune Au chemistry for new applications. Incorporating other metals into Au-based bimetallic NPs is one important yet largely unexplored means of tuning Au. However, most transition metals are insoluble in bulk gold at room temperature (Cu, Ag, and Pd are notable exceptions)[24]. Although NPs can be prepared within bulk miscibility gaps[50, 13], substantial synthetic efforts are required to develop preparation methods for individual metal compositions. In this chapter, we will explore the possibility of tuning Au chemistry with transiition metals before synthetic efforts are made.

7.1 Calculation details

Density functional theory (DFT) calculations on Au-M metal slabs may provide insight into these questions and guide the efforts of synthetic chemists. Accordingly, we investigated a series of Au(111) surfaces where the subsurface monolayer is replaced with another metal. The strong surface segregation energies calculated for Au-M binary mixtures indicate a strong thermodynamic driving force for moving Au to the surface of such materials[74], which makes the calculated structures reasonable models for nanoscale materials. This approach probes electronic effects without inducing structural effects (lattice expansion/ compression, surface roughening) which can mask the nascent electronic influences of the hetrometal[13]. Accordingly, the top three layers of Au-M-Au(111) slabs, where M = 3d, 4d, or 5d transition metal, were allowed to relax in an energy minimization calculation. Adsorption energies were then calculated for a variety of molecules interacting with the optimized slabs.

7.2 Results

In figure 7.1a we show calculated adsorption energies for CO and O (the product of dissociative O_2 chemisorption) on the 3d and 5d subsurface monolayer slabs (data for 4d slabs are omitted for clarity). All energies plotted are relative to that species on the pure Au(111) surface. We see that all the transition metals introduced increase the adsorption energies for both CO and O. Periodic trends of the adsorption energies based on the heterometals are found, with earlier transition metals inducing stronger adsorption on the Au surface. Further, 5d metals (filled symbols) more effectively increase the strength of the Au-adsorbate interaction than 3d metals (open symbols). These changes can be large, with Re and W increasing Au-O interaction by nearly 1 eV relative to pure Au. These results are in stark contrast to previous computational and experimental work on Pt-M-Pt(111) surfaces, where incorporating earlier transition metals results in weaker substrate binding[47, 14].

It is noticed that the 2^{nd} layer metal impacts O adsorption more strongly than CO adsorption as shown in figure 7.1a. We therefore investigated several other representative adsorbates. In order to facilitate comparing the adsorption energy sensitivity to the 2nd layer, the range of adsorption energies for each adsorbate and heterometal period are shown in Figure 7.1b.A clear trend observed is that the heterometal period affects the adsorption energies, with an order of 5d>4d>3d metals. This is perhaps not surprising as elements of the same row have similar frontier orbital energies and sizes are therefore more likely to

interact more strongly.

The second trend of note is that electron withdrawing adsorbates (CO, O) show much greater sensitivity to the 2nd layer than does NH_3, a more traditional electron donating adsorbate / ligand. Adsorption of water and methanol is essentially insensitive to the 2nd layer. It is also noteworthy that there is no clear correlation between the adsorption sensitivity and the adsorption strength: water, methanol, ammonia, and atomic O have roughly the same adsorption energy on Au(111), with a relatively small variance ($\pm$0.08 eV), while CO adsorbs about 0.4 eV stronger.

A primary goal of the study in this chapter was to evaluate the potential to tune gold chemistry through doping with other transition metals, and the results have important implications for Au NP chemists. First, the stronger binding of electron withdrawing adsorbates suggests it may be possible to alter the surface chemistry of Au by doping with appropriate heterometals. If appropriate nanostructures can be prepared, this may aid in imparting substrate specificity. Additionally, the calculations suggest that employing some colloid stabilizers with electron withdrawing properties may help to stabilize new bimetallic Au-based NPs.

The results also have obvious implications for CO oxidation catalysis. Our studies from Chapter 6 suggests that CO oxidation rates over a variety of metals can be described in terms of CO and O adsorption energies. We expanded the average volcano plot from Chapter 6 to include the current data, as shown in figure 7.2. Most of the bimetallic combinations increase the Sabatier activity of Au surfaces, and several approach the activity of the Au(532) surface. The various bimetallic combinations also cover a fairly large section of the volcano plot, suggesting that further tuning might be possible. Although real supported catalysts are almost certainly more complicated than the computational models, recent experimental studies support these general conclusions from these computational studies. For example, both supported Ni-Au NP catalysts[13] and Au/Ni(111) surfaces[49] show increased low temperature CO oxidation activity relative to pure Au.

The weak binding of O_2 to Au NPs[56] limits a number of potential applications, particularly in oxidations employing O_2 as the terminal oxidant[42, 17]. Given that heterometal incorporation induces stronger O binding and faster Sabatier CO oxidation rates, other Au catalyzed oxidations may be similarly affected. Further, since O_2 is more sensitive to the 2nd layer than other adsorbates, it may be possible to increase O_2 binding relative to oxidizable substrates and solvents, potentially reducing unwanted side reactions.

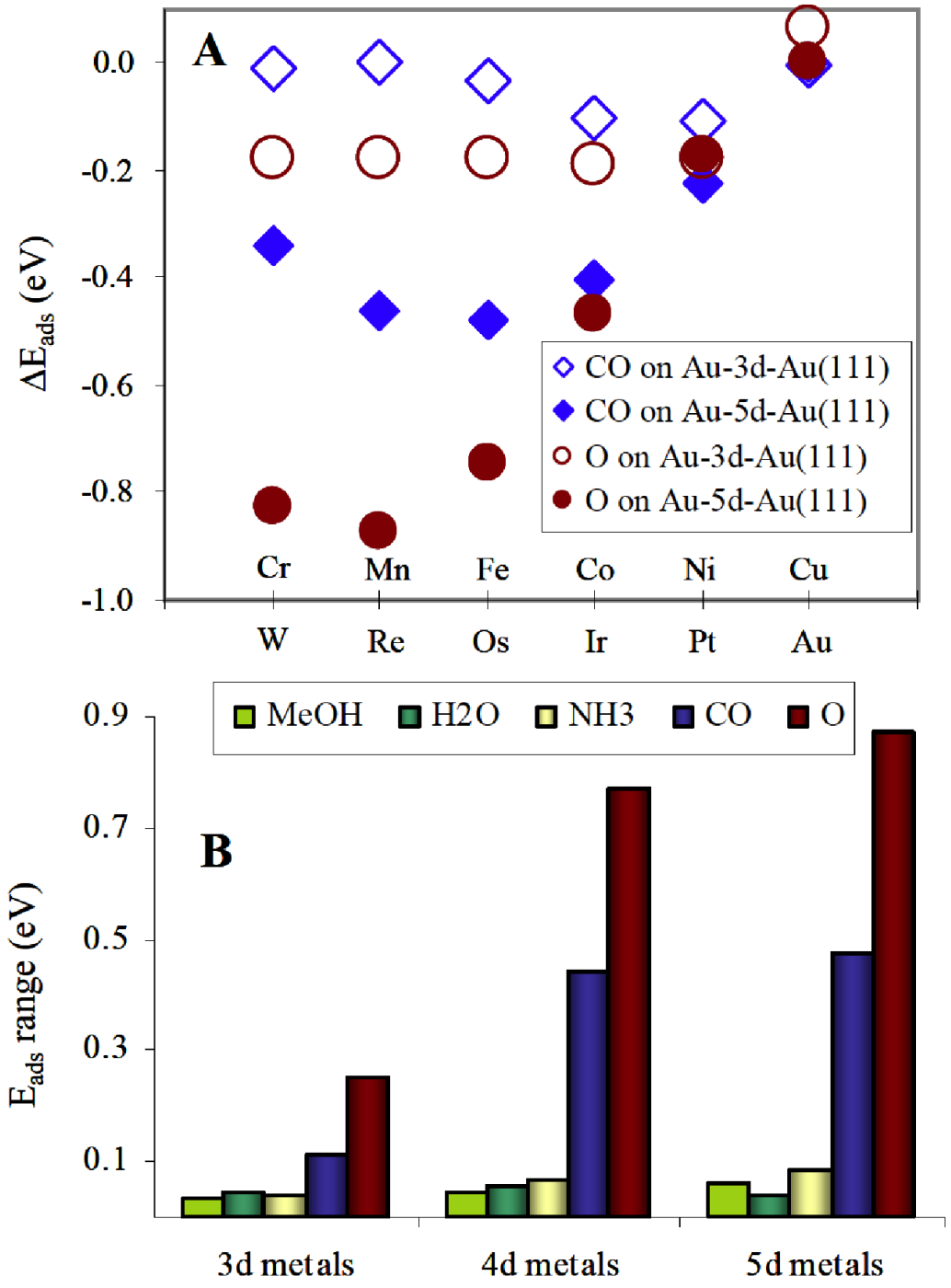

Figure 7.1: Adsorption data for Au-M-Au(111) slabs. (a) Adsorption energies for CO and O, relative to pure Au(111). (b) Adsorption energy ranges (sensitivity) for CH_3OH, H_2O, NH_3, CO, and O. The sensitivity represents the range in adsorption energies of each adsorbate for each series of heterometals in the 2^{nd} layer. For water and methanol, no clear trend was observed, so the standard deviation is reported.

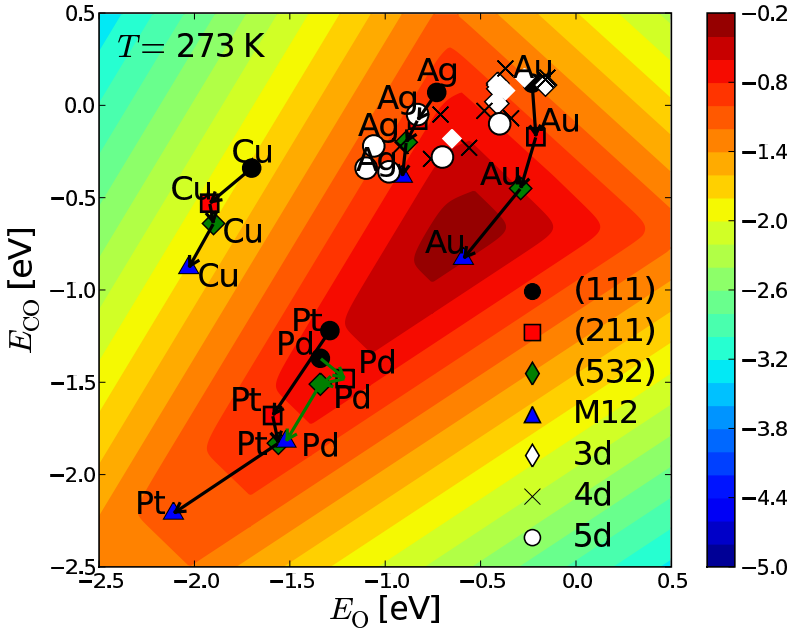

Figure 7.2: Contour plot of the Sabatier activity in eV as a function of CO and O adsorption energies at T = 273, P_{O_2} = 0.21 bar, P_{rmCO} = 0.01 bar. Activities for several pure metals (Au, Ag, Cu, Pt, Pd), various surfaces ((111), (211), (532)), and a 12-atom cluster (M12) are presented in filled symbols. Activities for the Au-M-Au(111) slabs are presented with open symbols and show the calculated changes in CO oxidation activity relative to the pure Au(111).

7.3 Conclusion

In summary, DFT calculations on bimetallic Au-M-Au(111) slabs suggest that there is a large potential for tuning Au chemistry by incorporating other transition metals. Adsorption by electron withdrawing substrates is sensitive to the heterometals, with more electron rich earlier transition metals giving rise to stronger adsorption of O and CO on the Au surface. This trend is in stark contrast to Pt based alloys[47, 14], which show weaker adsorption with heterometals incorporation. The results indicate that there may be substantial opportunities to tune Au based oxidation catalysts. Further, the results may provide some guidance to synthetic chemists as they suggest that moderately electron withdrawing stabilizers may assist in preparing new Au based bimetallic NPs.

Chapter 8

Improving structural optimization in electronic structure calculations

In theoretical chemistry and in condensed matter physics, an important problem is to locate the minimum energy structure in the vicinity of the given initial structure. In theoretic catalysis study particularly, an estimation of about 90% of the computational power is dedicated to structure optimization of the adsorption state of some molecules on solid surfaces and searching the transition state of a chemical reaction by dragging method. Thus it is of great importance to use an efficient optimization algorithm in these applications. Most commonly used algorithm nowadays include quasi-Newton type methods (QN), among which rank two Broyden-Fletcher-Goldfarb-Shanno (BFGS) update scheme is considered to be the most efficient update scheme, and has been widely implemented in DFT codes. Despite the standard update formula, different implementation of the algorithm can give very different convergence rate.

It is theoretically proved that quasi-Newton type algorithm gives a super linear convergence rate to the minimum of the objective function[64]. When applied with electronic structure calculation, however, it is not flawless. Following is a sequence of typical convergence of quasi-Newton steps with BFGS update scheme:

Iteration	Energy (eV)	Force (eV/Å)
0	4.940476	3.4251
1	3.435473	1.9749
2	1.065691	0.9166
3	0.725099	0.7348
4	0.553567	0.6526
	...	
15	-0.008041	0.0602
16	-0.009779	0.0496
17	-0.010688	0.0386
18	-0.011713	0.0369
19	-0.012716	0.0338
	...	
40	-0.029619	0.0486
41	-0.029267	0.0414
42	-0.030918	0.0346
43	-0.031517	0.0303
44	-0.031860	0.0253
45	-0.032000	0.0191

Here the convergence criterion is the force should be lower than 0.02 eV/Å. We see that in the beginning the force (derivative of the objective function, energy) decreases quickly. However, after 15 steps the convergence of force becomes slower, and we even observed the increasing of the energy. It took another 25 steps for the force to decrease from 0.0338 eV/Åto less than 0.02 eV/Å. It seems that the quasi-Newton algorithm becomes less efficient when the derivative of the objective function becomes small, and the direction given by quasi-Newton algorithm leads the structure optimization "wandering" around the local minimum of the potential energy surface, and slows down the rate of convergence.

In this chapter, we will try to understand the origin of the problem of the slow convergence, and then give a solution so that the robustness of the BFGS algorithm can be improved. For understanding the convergence problem, we compute the total energy and force of our test system with potentials given by effective medium theory, which provides total energy and analytical force with negligable computational effort compared to DFT calculation. In the end, we also performed calculation to test the performance of our revised optimizer with DFT calculations.

8.1 Eigenvalue spectrum

We start by applying harmonic approximation to the vicinity of a minimum of the potential energy surface, which means that the potential part of the hamiltonian can be written as the linear combinations of vibrational modes that are orthogonal to each other. The total energy can then be expressed in a simple form:

$$E = 1/2 \sum_i k_i (x - x_0)^2 \tag{8.1}$$

where k_i is a generalized force constant for each eigen mode. We note that there are no cross terms in equation (8.1). A simple yet costy way of minimizing the energy surface can be done by successive minimizations along the modes until the minimum is found. The eigenvalue shows the steepness of its corresponding eigenmode. The condition number defined as the largest eigenvalue divided by the smallest eigenvalue, shows how difficult the problem to be minimized is. It is therefore natural to study the eigenvalue distribution of representative system as the first step.

In figure 8.1 we plotted the size of the eigenvalue of a Cu bulk system including 54 atoms with small perturbation on the the coordinates of each atom. One atom is fixed to remove the translational modes, thus the total number of eigenvalues is 159. We see that the eigenvalues are power-law distributed, and there are only few high eigenvalues and low eigenvalues. The majority of the eigenvalues lays between 20 and 2.

Based on this approximation, re-analyzing the slow convergence mentioned in the beginning of the chapter, we notice that at step 15, the energy has decreased more than 99% comparing to the converged energy, the rest 30 steps only reduced less than 1% of the energy. This phenomenon suggest that among all the normal modes, strong modes converges quickly at the beginning of the optimization. It is not surprising since strong modes are more harmonic and the quadratic model used in quasi-Newton method gives good estimation of these modes. The anharmonicity arises when modes get weaker, and the quadratic model of the quasi-Newton method may not be able to describe these modes good enough to give a reasonable prediction of the location of the minimum. Since the new search step is given by

$$dr = \sum_i \frac{\vec{v_i} \cdot (\vec{f} \cdot \vec{v_i})}{\lambda_i}, \tag{8.2}$$

where $\vec{v_i}$ is the eigenmode and λ_i is its corresponding eigenvalue, f is the force. We see from equation (8.2) that since there is eigenvalue in the denominator, for

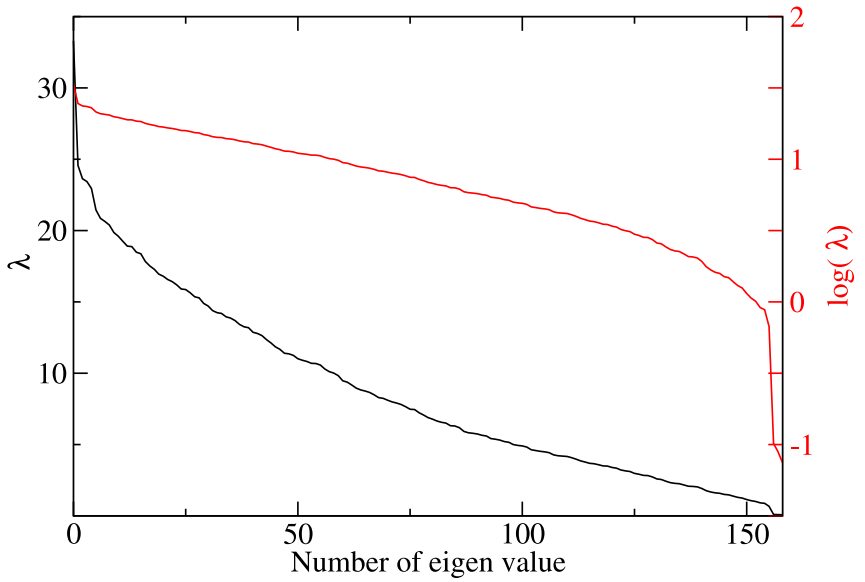

Figure 8.1: Eigenvalue spectrum of the normal modes of 54 atoms Cu bulk structure. The black line is the original eigenvalues, while the red line is the logarithm of the eigenvalues.

an eigenmode with small eigenvalue at for instance around 0.01, the uncertainty due to the anharmonicity will be amplified 100 times.

Another possible reason is related to the updating of the Hessian matrix. As mentioned in chapter 3, it is important that the Hessian matrix is kept positive definite so that the curvature condition (3.10) is fulfilled and the force will be reduced along the optimization. We see in the example, however, after step 15, the energy and force are not monotonically decreasing, which may results in equation (3.11) giving negative update to the Hessian matrix. In DFT calculations particularly, there exist numeric noise in force and energy since the electronic structure can not be perfectly converged. The noise is not obvious in the beginning of the optimization since it is negligible when moving along strong modes. Starting from the middle of the minimization, since strong modes are relaxed, the size of the noise can be comparable to the energy change when moving along weak modes. The quality of the updating of the Hessian matrix may decrease and therefore influence the rate of convergence of the optimization algorithm.

One would naturally think that by reducing the portion of step projection on low modes may solve or at least mitigate the problem. We set a threshold to the low eigenvalues, and set the eigenvalues lower than this threshold (t) to it. Equation (8.2) is now formulated as

$$dr = \sum_i \frac{\vec{v_i} \cdot (\vec{f} \cdot \vec{v_i})}{\max\{t, \lambda_i\}}. \tag{8.3}$$

In table 8.1 we listed the convergence properties of optimization with different low eigenvalue threshold (t). The convergence criterion is that the maximum force on any atom in the system should be smaller than 0.02 eV/Å. It is noticed that the convergence is not affected when t is lower than 2.0. The convergence become faster when t gets higher than 2.0. On the other hand, however, the final energy become higher when the optimization reaches convergence. This observation suggest that limiting the movement along the weak does help improve the convergence speed. However, by doing this, the weak modes can not be fully relaxed before the convergence criterion is reached and the final structure can still be rather different from the structure at energy minimum. It is possible to get the energy correct by setting more strict convergence criterion, and will in turn increase the number of iterations since the system is forced to take small steps along the weak modes.

Table 8.1: Convergence properties of optimization with different low eigenvalue threshold(t)

t	Iteration	Energy	t	Iteration	Energy
-	183	-0.0324	2.5	74	-0.0319
0.1	183	-0.0324	3.0	24	-0.0264
0.5	183	-0.0324	5.0	11	-0.0167
1.0	188	-0.0320	10.0	13	-0.0134
2.0	165	-0.0324			

8.2 BFGS with line search

We see from the previous sections that the anharmonicity of the weak modes may suggest poor Newton steps. Taking these steps may lead to poor updates that breaks the semi-positive definition of the Hessian matrix.

To solve this problem, a line search which fulfills Wolfe conditions should be incorporated for determining the step size along the direction given by BFGS

algorithm instead of just taking the Newton step. By doing so, both the energy and the force along the search direction are ensured to decrease and the Hessian matrix is forced to be positive definite as discussed in chapter 3.

The incorporation of line search is simple. Any Quasi-Newton optimizer can be used and the change is only passing the Newton step to the line search algorithm as the search direction $\vec{p}$ and the initial guess of the step size α_0. The procedure can be described as follow:
QN: Update the Hessian matrix **B** or the inverse of the Hessian matrix **H** using any update scheme and calculate $\vec{p}$ by equation (8.6), α_0 is set to 1.
L1: set 0 to α and evaluate the energy and force at α_0, then check if α_0 fulfills Wolfe conditions. If it does, return to QN with α_0.
L2: Calculate the new step by interpolating the forces and energies of α and α_0. Set α to α_0 and the new step to α.
L3: Check if α fulfills Wolfe conditions. If so, return to QN with α, otherwise go back to **L2**.
QN: Evaluate the energy and force at $\alpha \cdot \vec{p}$ and check for convergence.

We adapted the line search scheme (SciPyBFGS) from Scientific Python as starting point. The line search includes two phases, the bracketing phase and the interpolation phase. In the bracketing phase, two points (α_{lo} and α_{hi}) are used to bracket the minimum. α_{lo} is defined as the step length among all step lengths generated before the current step that satisfy the sufficient decrease condition giving the smallest energy; and α_{hi} is chosen to be the step that fulfill $\phi'(\alpha_{\mathrm{lo}})(\alpha_{\mathrm{hi}} - \alpha_{\mathrm{lo}}) < 0$ and its energy shall be as low as possible. When the minimum is bracketed by α_{lo} and α_{hi}, the line search enters the second phase in which interpolations are made with the energy and force information of α_{hi} and α_{lo} to generate the new trail step. Detailed description of the line search algorithm can be found in figure 8.2. Different interpolation scheme such as cubic fit, quadratic fit and secant fit are used for different situations.

To demonstrate the performance of SciPyBFGS, we compared it to other popular optimization algorithms, molecular dynamics minimizer (MDMin), fast inertial relaxation engine (FIRE), conjugate gradient (CG), and three flavor of BFGS algorithm: BFGS algorithm with no line search (BFGS), limited memory implementation of BFGS algorithm (L-BFGS) and BFGS with trust region method for step determining (BFGSTR). Since in DFT calculation, the force is calculated by Hellmann-Feynman theorem with nearly no extra cost when getting the ground state energy of the system, the number of "force calls" can by use to demonstrate the cost of the minimizations with different algorithms.

We show in table 8.2 the cost of relaxing a set of representative systems in solid state physics and theoretical catalysis studies with the above mentioned optimizers. The "ERR" in the table means the optimizer failed to converge

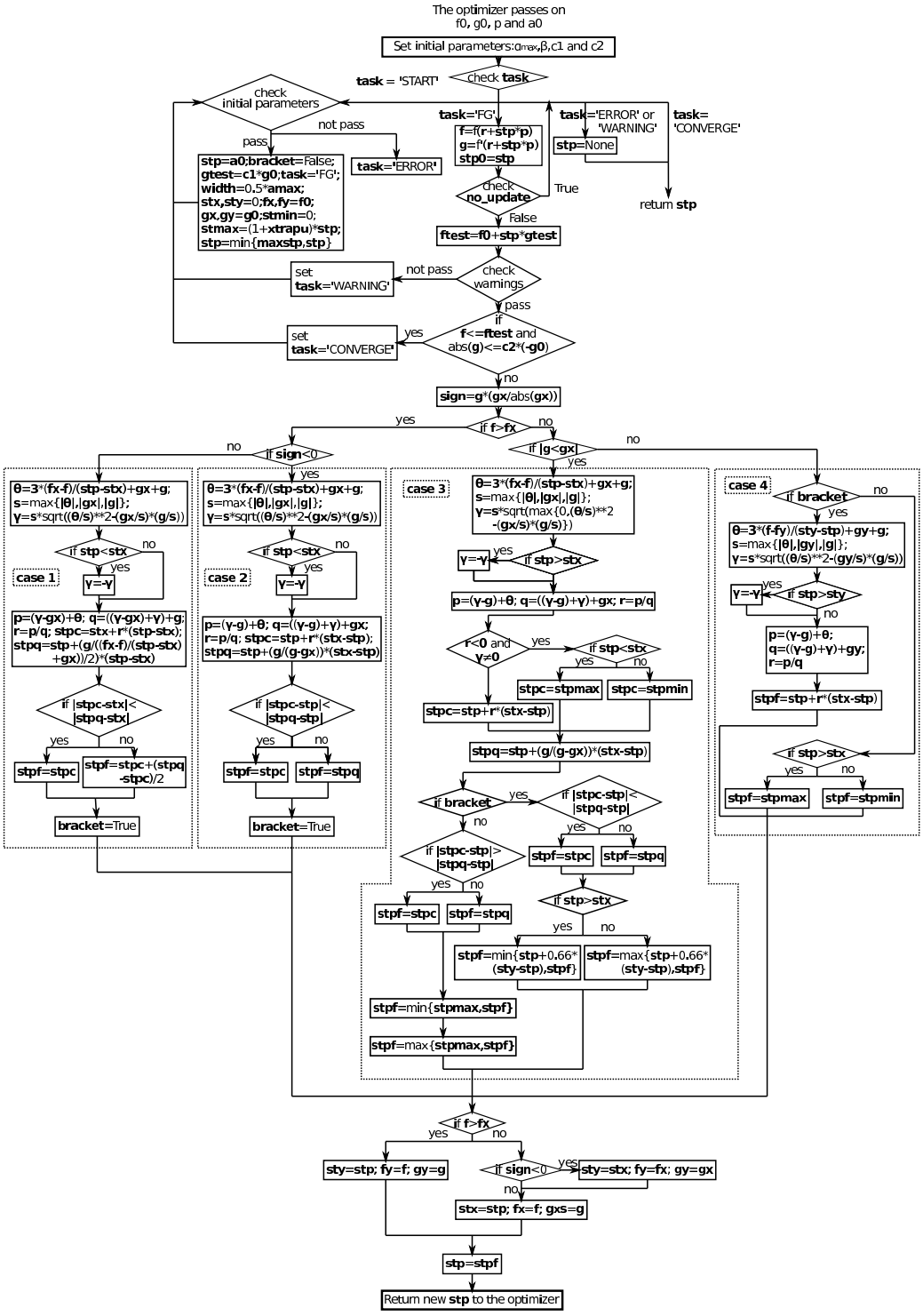

Figure 8.2: Schematic drawing of the line search scheme applied in BFGSLS.

Table 8.2: Number of force calls required by different optimization algorithms to reach convergence for the relaxation of different test systems. The convergence criteria were the maximum force on any atom in the test system shall be lower than 0.02 eV/Å. EMT and LCAO represent total energy calculations based on effect media theory and linear combination of atomic orbitals.

System	MDMin	FIRE	CG	BFGS	SciPyBFGS
N_2@Cu(EMT)	40	ERR	149	86	73
Cu bulk(EMT)	12	46	23	22	22
CO@Au(EMT)	ERR	153	66	58	37
C_5H_{12}(LCAO)	21	38	141	10	ERR
NH@Pd nano-partical(LCAO)	44	75	118	93	ERR

within the maximum number of iterations for the test system. From the test result we see that CG and BFGS converged all test cases, showing robustness since the test cases differs very much, as well as the total energy calculators. Another observation is that for the systems that are converged, the SciPyBFGS optimizer works better than the BFGS optimizer with no line search. Given the SciPyBFGS optimizer is designed for general optimization problem and the parameters in its line search scheme are not optimized for surface/molecule systems, the performance is reasonably good. The observation shows the possibility that by tuning the line search parameters, the SciPyBFGS optimizer may be able to give better performance on surface adsorption type of problems.

We parameterized the SciPyBFGS optimizer, and scanned for the optimum set of parameters for three representative systems in solid state physics and theoretical catalysis studies. The parameterized optimizer is called BFGSLS so that it is differentiated from the SciPyBFGS optimizer. After scanning, we noticed that most of the parameters are not sensitive to different systems, leaving only four parameters that affect the performance of the optimizer. These four parameters are β, $\alpha_{\max}$, c_1 and c_2. β is the preconditioner of the initial matrix H_0 mentioned in section 3.4. $\alpha_{\max}$ is maximum distance an atom can move in one step. It is important to note that if the maximum distance of the movement of any atom in the system $r_{\max}$ exceeds $\alpha_{\max}$, the movements of all the atoms shall be scaled down by $\alpha_{\max}/r_{\max}$ so that the the direction of movement of system suggested by Hessian matrix is preserved. Finally c_1 and c_2 are parameters in the Wolfe conditions mentioned in section 3.5.

In figure 8.3, 8.4 and 8.5 we show the rate of convergence of BFGSLS optimizations on CO adsorption on Au(111) surface, a gold cuboctahedron nanoparticle with 55 atoms and N_2 adsorption on Ru(0001) surface. The parameters of the BFGSLS algorithm are scanned to find the optimum set of parameters for

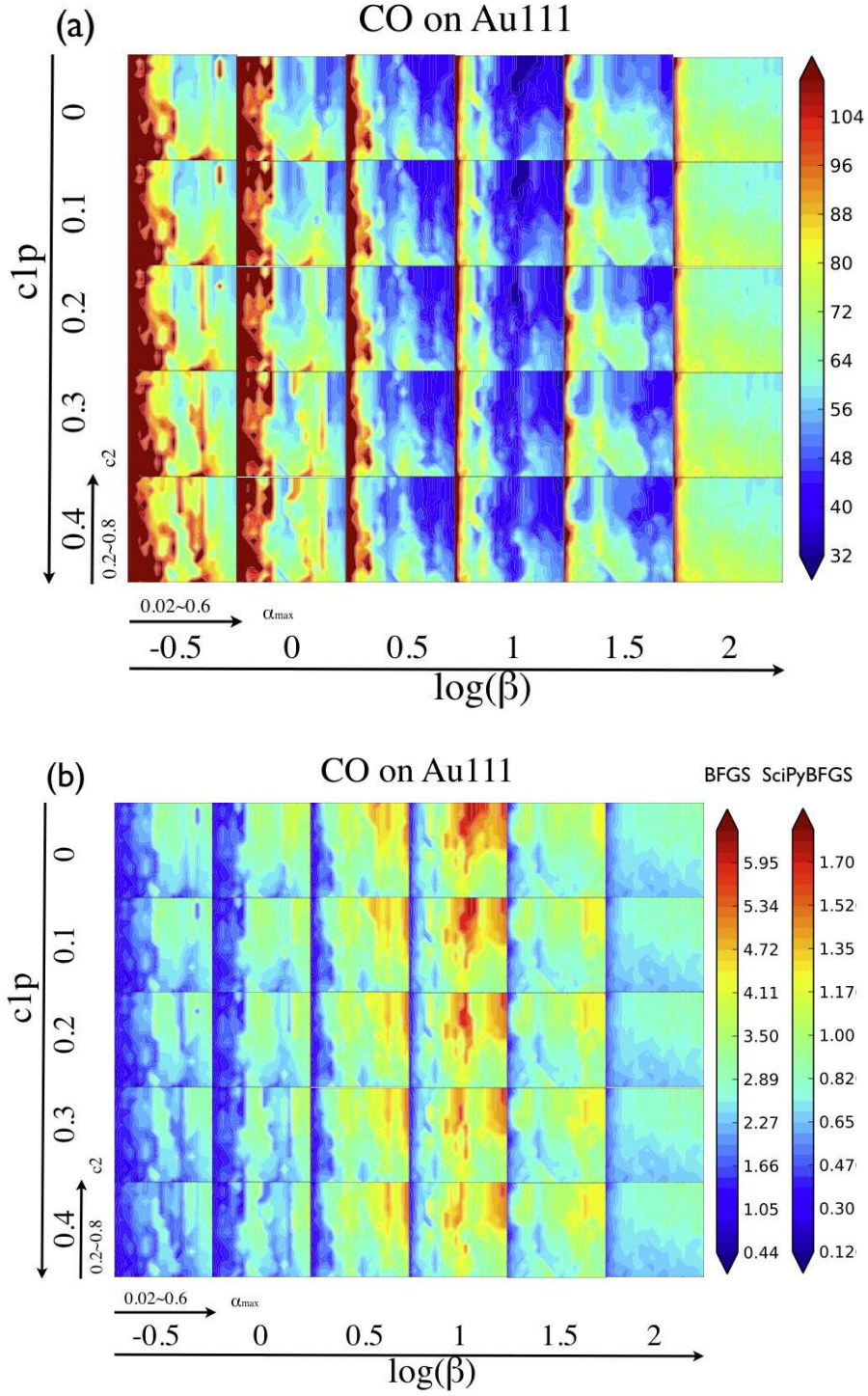

Figure 8.3: (a)The number of force calls needed to relax CO adsorption on Au111 surface plotted against the changing of parameters of the optimizer.(b) The speedup with reference to BFGS and SciPyBFGS

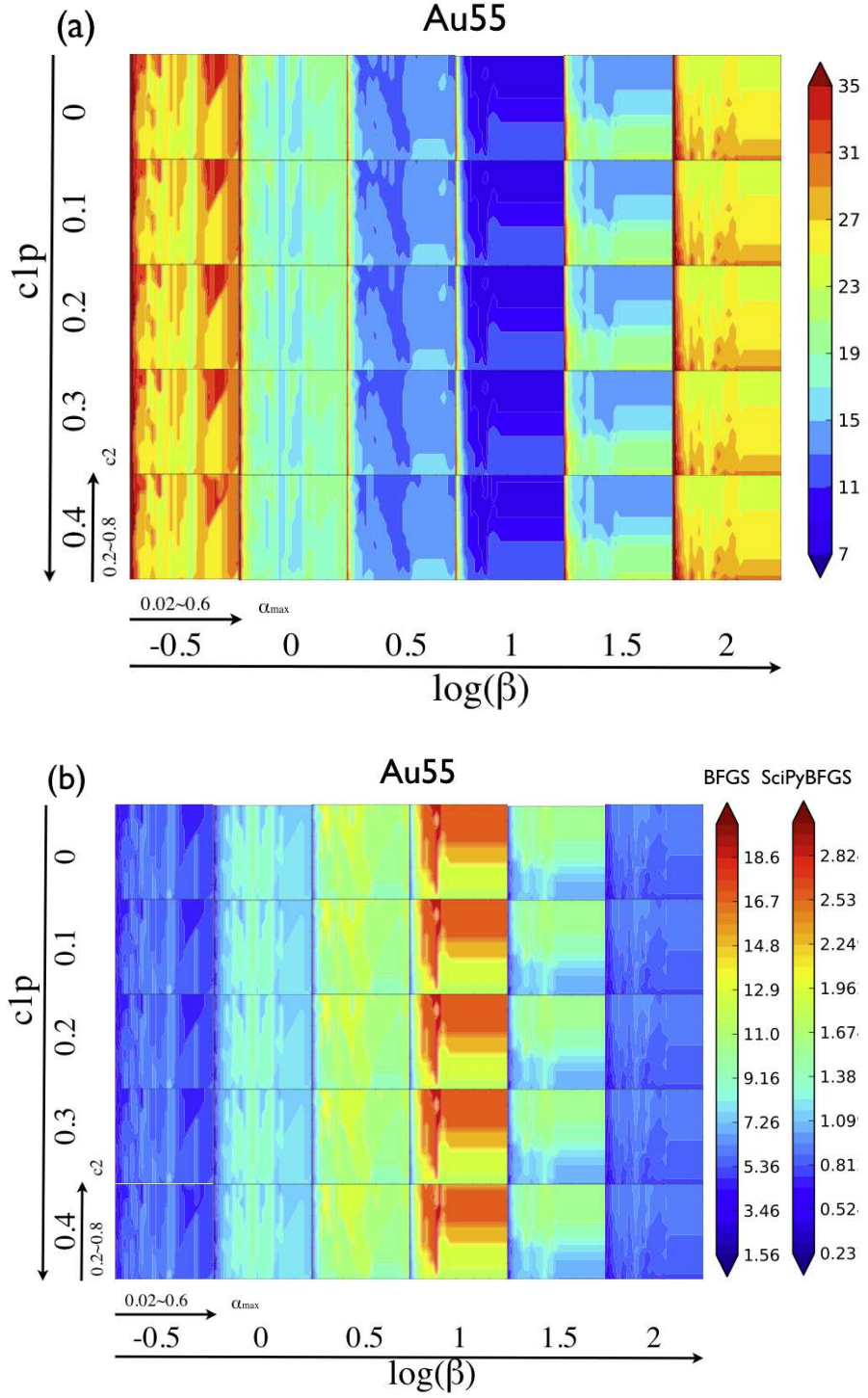

Figure 8.4: (a) The number of force calls needed to relax a gold cuboctahedron nanoparticle with 55 atoms plotted against the changing of parameters of the optimizer. (b) The speedup with reference to BFGS and SciPyBFGS

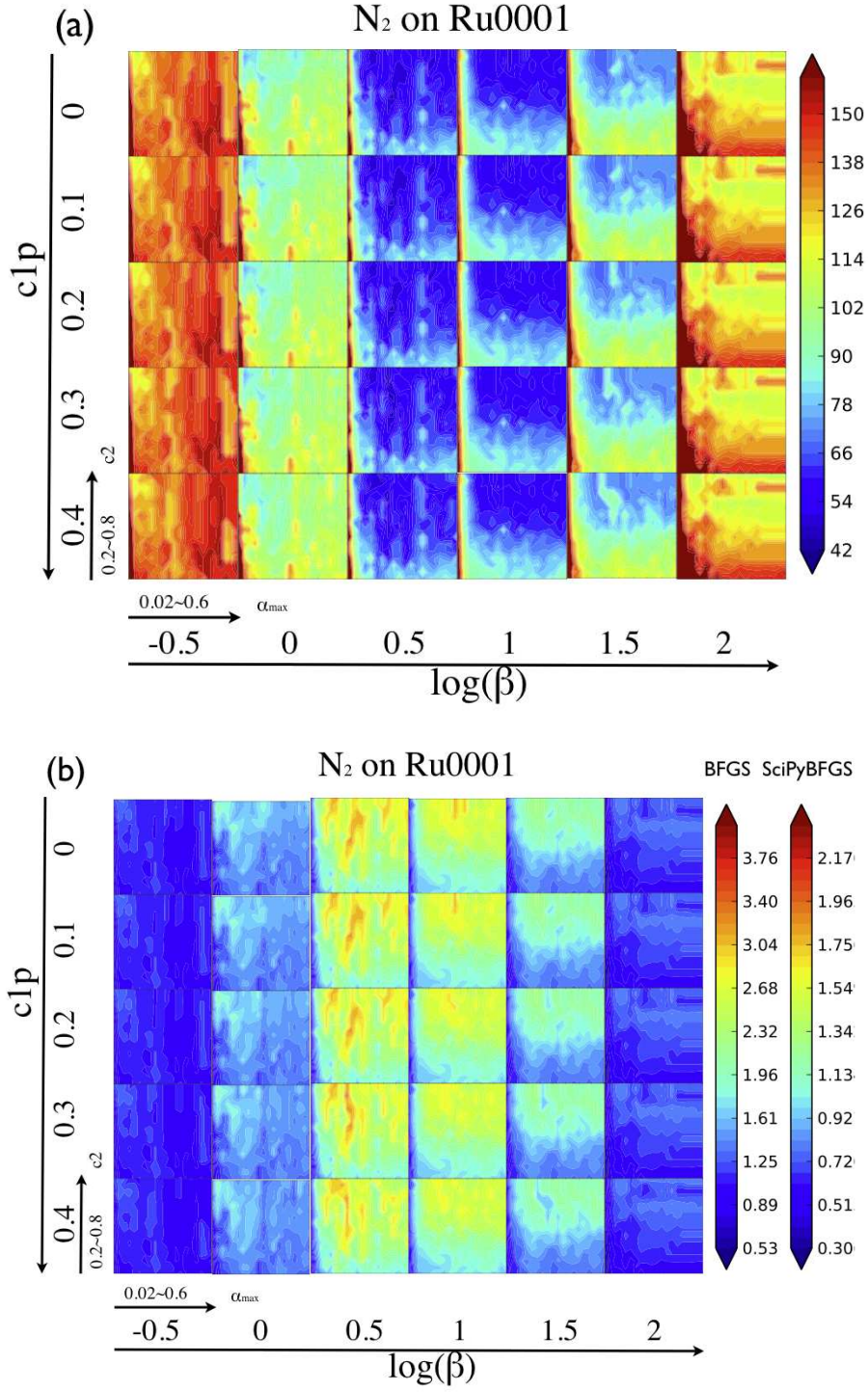

Figure 8.5: (a) The number of force calls needed to relax N_2 adsorption on Ru0001 surface plotted against the changing of parameters of the optimizer. (b) The speedup with reference to BFGS and SciPyBFGS

molecule/surface systems. EMT calculator is used for calculating the total energies and analytical forces. In figure 8.3a, 8.4a and 8.5a the numbers of force calls needed to converge a set of parameters on a given system are plotted, while in In figure 8.3b, 8.4b and 8.5b the speedups with reference to BFGS with no line search and SciPyBFGS are plotted. In each small block $c2$ and $\alpha_{\max}$ are varied from 0.2 to 0.8 and from 0.02 to 0.6, keeping $c1p$ and β fixed. In the whole plot, $c1p$ and $log(\beta)$ are varied blockwise perpendicularly and vertically. Here we used $c1p = c1/c2$ instead of $c1$ so that $c1$ will be in the range of $0 < c1 < c2$.

We see in the plots that for all three systems we considered, same trend of the optimizer performance over the parameter change is found. For any $c1$ and β, the optimizer converges faster when the $\alpha_{\max}$ is higher than 0.15 Å. It is easy to understand since when $\alpha_{\max}$ is set to too low, the step size change in the line search can not be taken completely, more steps are then needed. On the other hand, when $\alpha_{\max}$ is high enough, the trail step can always be taken fully, therefore the performance of the optimizer does not change much. It is also observed that the higher the value of $c2$, the less force evaluations are needed to reach convergence. Since lower $c2$ value means more strict line search criteria, the results suggest that given other parameters set properly, as long as the force is reduced by the line search the Hessian matrix will get a proper update and the convergence is guaranteed. Over strict line search criteria will waste computational power on unnecessary convergence of the line search. The changing of $c1$ value seems to have minor influence on the convergence. It is not a surprising result as $c1$ is defined to be smaller than $c2$, in the vicinity of a local minimum the curvature condition (equation (3.15b)) is naturally more strict than the sufficient decrease condition (equation (3.15a)).

The influence from varying the preconditioner (β) of the Hessian matrix is significant. By varying $log(\beta)$ from -0.5 to 2, the convergence rate can differ 3 to 5 times, too high and too low β will both hinder the convergence. Reformulating equation (8.2) we get

$$dr = \sum_i c_i \vec{v}_i, \tag{8.4}$$

where the coefficient $c_i = \vec{f} \cdot \vec{v_i}/\lambda_i$. The Hessian matrix is set to be a diagonal matrix with preconditioner on the diagonal entries. The BFGS update is a second order update scheme, which means after each update up to two eigenmodes of the Hessian matrix will be updated, and the rest of the eigenmodes are forced to be orthogonal to the updated modes however with no information about these modes is collected. The step is the sum of steps along all modes, known or unknown. The benefit of preconditioning the hessian matrix is to adjust the size of the first step in the line search. If β is too small or too big, the trail step will be poorly chosen and many function evaluations may be required to find a suitable step length to fulfill the Wolfe conditions ((3.15)). The effect

comes from the regulation of the aggressiveness on the unknown modes by the preconditioner. It is rational to set the preconditioner to be in the middle of the eigenvalue spectrum of the real hessian matrix which is unknown in general, so that a reasonable step size along the search direction shall be taken. From the scanning we found that the optimizer perform better when β is around 3-30, which is right in the middle of the eigenvalue spectrum of the Cu bulk we studied. For different systems, i.e. different elements and different type of bonding, the eigenvalue spectrum may differ significantly, however, $\beta = 10$ remains a reasonable choice since there always exist rather weak phonon modes or bending modes of the molecules that a well below 10.

Table 8.3: Number of force calls required by different optimization algorithms to reach convergence for the relaxation of different test systems. The convergence criteria were the maximum force on any atom in the test system shall be lower than 0.02 eV/Å. EMT and LCAO represent total energy calculator based on effect media theory and linear combination of atomic orbitals.

System	MDMin	FIRE	CG	BFGS	SciPyBFGS	BFGSLS
N_2@Cu(EMT)	40	ERR	149	86	73	50
Cu bulk(EMT)	12	46	23	22	22	8
CO@Au(EMT)	ERR	153	66	58	37	63
C_5H_{12}(LCAO)	21	38	141	10	ERR	15
NH@Pd nano-partical(LCAO)	44	75	118	93	ERR	64

After the scanning, we chose the optimum setting of the parameter, $\beta = 10$, $\alpha_{\max} = 0.2$, $c1 = 0.23$ and $c2 = 0.46$ and compare the performance of the optimized parameter (BFGSLS) with other optimizers on the same test system set again. The result is shown in table 8.3. We see that the BFGSLS out perform all other optimizers both on robustness and speed.

8.3 Preconditioning the Hessian matrix

8.3.1 Adaptive update of the preconditioner

The idea of preconditoning the hessian is to place the initial eigenvalues of the unknown eigenmodes in the possible middle of the eigenvalue spectrum of the real hessian matrix to be approximated. $\beta = 10$ is a general good choice for optimization problems in theoretical catalysis and solid state physics, however, may not be the best choice for every system.

Nocedal and Wright suggested a heuristic way of preconditioning the Hessian[64]. After the first step is taken but before the first BFGS update is performed, the initial inverse of Hessian $H_0 = I$ is changed to

$$H_0 = \frac{y_0^T s_0}{y_0^T y_0} I. \tag{8.5}$$

By doing so, the size of H_0 is set to be close to $[\nabla^2 f(x_0)]^{-1}$. Since in the beginning of a relaxation the major contribution of the gradient comes from strong modes, and equation (8.5) describes largely the curvature information of strong modes. We should expect this precondition scheme to set the preconditioner close to one of the big eigenvalues of the real Hessian.

A possibly better way is to adjust the preconditioner for the unknown eigenmodes dynamically with the information acquired along the update of the Hessian matrix. This will ensure the trail step given by equation (3.6) is neither too short nor too long. One property of the update we observed is that in the beginning of the update procedure, each step updates two eigenvalues, the eigenvalues vary from the preconditioner, towards the directions away from the middle of the eigenvalue spectrum of the real Hessian matrix, that is, one being raised and one being lowered. It is therefore possible to design an adaptive update scheme to keep the preconditioner in the middle of the eigenvalue spectrum of the real Hessian matrix by utilizing this property.

The implementation of the adaptive update method (AUM) is simple. Normal Quasi-Newton procedure is taken, the only difference is that after each update of the Hessian matrix B, an adjustment of B is taken. In the adjustment, an eigenvalue decomposition is done to B to get the eigenvalues λ_i and corresponding eigenvectors ν_i. The eigenvalues are then sorted in to two groups, the ones that are updated, and the ones not yet updated that are still equal to the preconditioner β. Then the log10 of the updated eigenvalues are taken and the average of them Ω_a is calculated, β and the not yet updated eigenvalues are set to 10^{Ω_a}. We then calculate the adjusted Hessian matrix by $B_{ad} = V\Lambda V^{-1}$, in which V is the square $(N \times N)$ matrix whose i^{th} column is the eigenvector ν_i of B, and Λ is the diagonal matrix whose diagonal elements are the corresponding eigenvalues that are adjusted. The idea behind this adjustment is the power-law distribution of the eigenvalue spectrum we observed in section 8.2.

Convergence test of the adaptive update method (AUM) is done on two types of systems, two bulk (Cu and Au) structures and two adsorption systems N_2 adsorption on Cu and CO adsorption on Au, the results are listed in table 8.4.We see that for all the systems, AUM tends to give similar convergence rate. For bulk systems, AUM gives faster convergence rate comparing to QN without AUM. While for adsorption systems, the AUM is less efficient. When

Table 8.4: Numbers of function evaluation needed to minimize the force of different systems to be lower than 1e-5 eV/ Å. In the bulk systems, the atoms were randomly displaced from the equilibrium for 0.1 Å. The tests are done with the preconditioner β set to 0.1, 1, 10 and 100, both with and without adaptive update method (AUM). NW stands for the preconditioning method from Nocedal and Wright mentioned in this section.

System	$\beta = 0.1$		$\beta = 1$		$\beta = 10$		$\beta = 100$		NW
	with AUM	w/o AUM	with AUM	w/o AUM	with AUM	w/o AUM	with AUM	w/o AUM	
Cu bulk (64 atoms)	28	67	27	53	27	30	39	80	42
Au bulk (27 atoms)	22	55	21	38	22	38	45	69	30
N_2@Cu	149	170	172	133	148	113	139	213	197
CO@Au	94	99	89	56	97	72	102	107	124

preconditioner is 1 or 10, the convergence rate is slower with AUM than without. We also listed the test results with the preconditioning method proposed by Nocedal and Wright (NW) for comparison. We see that in almost all cases, the AUM out perform the NW method.

In figure 1.6 we plot the change of Ω_a during the relaxation. We see that for bulk systems in the first row, when β is no larger than 10, Ω_a converges to the average of the exact eigenvalues in around 10 iterations. When $\beta = 100$, Ω_a is also reduced to less than 10 with 10 iterations. As for adsorption systems in the second row, with any β, in the beginning of the relaxation, Ω_a is raised to high values, and reduced to the exact average slowly. This is because in the beginning of the relaxation, the strong modes from molecular stretching (on the order of 100) dominates Ω_a and it takes more iterations of updates to bring down the influence of these high eigenvalues, therefore the convergences are slower.

8.3.2 Preconditioning the BFGSLS with model Hessian

Quasi-Newton methods move system towards the neighbor local minimum of the potential energy surface (PES) by applying the Newton step

$$p_k = -B_k^{-1} \nabla f_k. \tag{8.6}$$

If the vicinity of the local minimum of the PES is quadratic and given the exact Hessian matrix, only one step would locate the minimum. Generally speaking, the PES are not perfectly quadratic, and the exact Hessian will not lead the optimization to the minimum in one step and further update of the Hessian for the true force change that obeys equation (8.6) is needed. Since acquiring

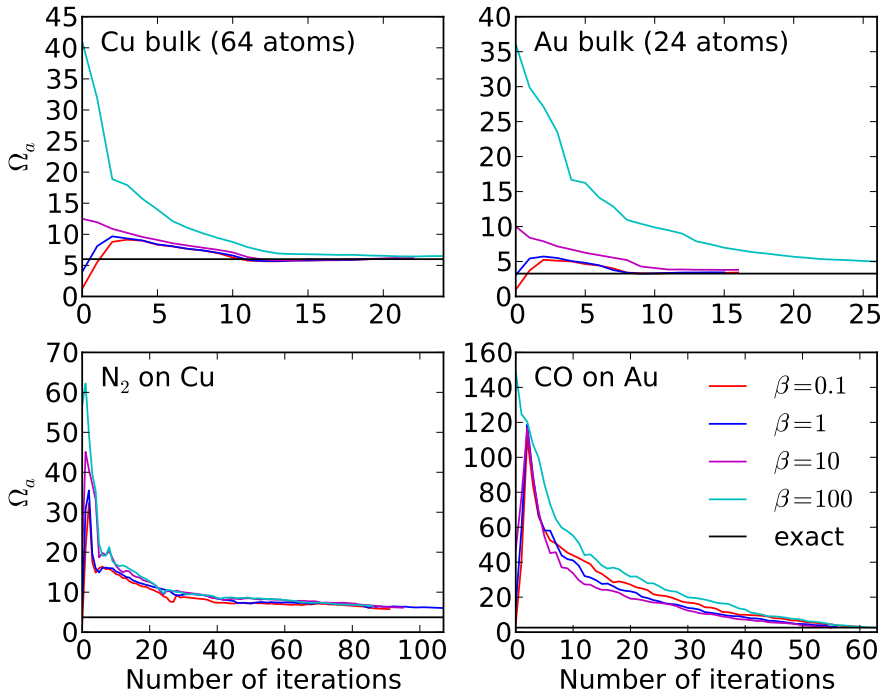

Figure 8.6: Change of Ω_a during the relaxation with different preconditioner β on different systems. Ω_a of the exact Hessian for the final structures are plotted for comparison.

the exact Hessian is sometimes computational more intense than optimizing the system with a unitary matrix as initial Hessian, it would be more practical to calculate the Hessian matrix with computational less intense method so that the modes are qualitatively captured. This matrix may generate better search direction and provide faster convergence rate. The idea has been carried out in literature [26, 30, 22] and shown significant improvement of the convergence rate comparing to using unitary matrix as initial Hessian.

We adapted the simple universal potential that describes bond bending and stretching suggested by Fernandez-Serra et al.[22]. After test, we find the part of the potential that describes bond bending is rather expensive to compute. Since the goal is to find a simple potential to generate a qualitatively correct Hessian that suggests better search direction that unitary matrix, we decided to drop the complexity and only use the stretching part of the potential defined as

$$U = \frac{1}{2}\sum_{i<j} k_{ij}^{s}(r_{ij} - r_{ij}^{0})^2, \tag{8.7}$$

$$k_{ij}^{s} = A(\frac{R_i + R_j}{r_{ij}^{0}})^P, \tag{8.8}$$

where R_i and R_j are the covalent radii of the atoms connected. The sums in equation (8.7) are limited to neighbors within n$\times$ max$[R_i]$, tests show that increasing the value of n to higher than 4 gives negligible change on the Hessian.

The Hessian with the spring model potential is then calculated with finite different methods for calculating second derivative numerically. Since the spring potential is defined to be zero at r^0 and increases when going away for it, the Hessian is guaranteed to be positive definitive. After computing the Hessian, a new coordinate system can be constructed by

$$y_n = \omega_n(\mathbf{x} \cdot \nu), \tag{8.9}$$

where ω_n and ν are the square root of the eigenvalues and the normal modes of the Hessian matrix, and $\mathbf{x}$ are the cartesian coordinates. The force on the new coordinate system can be calculated by

$$f_n = \frac{\mathbf{F} \cdot \mathbf{n}}{\omega_n}, \tag{8.10}$$

where $\mathbf{F}$ is the force in Cartesian coordinate system.

At this point some more words are needed to explain the convergence property of problem to be optimized. The condition number of a problem is defined as the ratio between the highest and lowest curvature $\lambda_{max}/\lambda_{min}$. The number of steps needed to optimize the system is related to the condition number, the higher the condition number, the more steps needed. Transforming the problem from Cartesian system to the new coordinate system will change its condition number. If, for instance, the new coordinate system is derived from the exact Hessian of a perfectly quadratic the system, the condition number on the new coordinate system is 1, and the exact minimum shall be found in one step. The idea of preconditioning the optimization in this section is to give a good approximation of the real Hessian by using a simple spring model, so that after the coordinate transformation the condition number can be decreased.

From equation (8.7) we see that the only parameter that may change the condition number is P, since A is a scalar that change all the curvatures with the same ratio. In figure 8.7a we plot the change of condition number of a copper

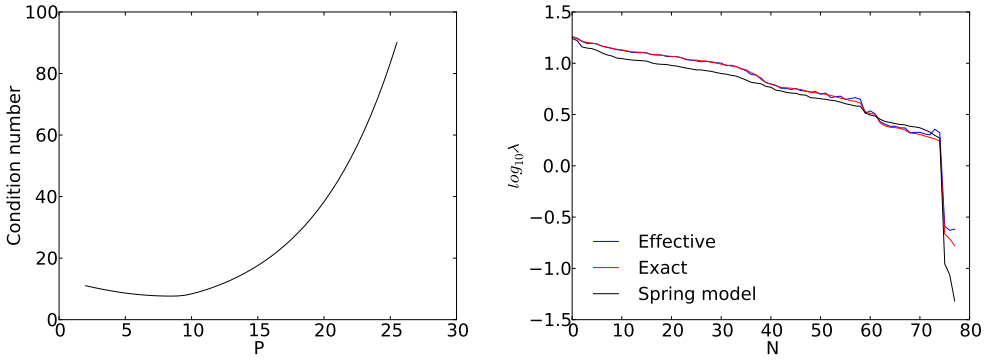

Figure 8.7: Left:Condition number of the exact Hessian matrix transformed to the new coordinates, the new coordinates are established by Hessian matrix from spring model with different P. Right: Spectrum of eigenvalues of the exact Hessian and Hessian from the spring model, as well as effective eigenvalues defined in equation (8.11) with $A = 0.79$ and $P = 8.5$.

27 atoms bulk structure with all the atoms randomly displaced from the equilibrium for 0.1 Å, when P is altered. We find the minimum of the condition number (7.66) locates at around $P = 8$, which agrees well with the P value chosen in [22]. The condition number in the original Cartesian coordinate system is 109.41, the coordinate transformation reduced the condition number by a factor of 14.28. In Figure 8.7b we plot the eigenvalue spectrum of the exact Hessian and the Hessian from spring model with A=0.79 and P=8.5 in Cartesian coordinates, as well as the effective eigenvalues of the spring model defined as:

$$\lambda_i^{Eff} = \sum_j c_{ij}^2 \lambda_j^E, \tag{8.11}$$

$$c_{ij} = \nu_i^S \cdot \nu_j^E, \tag{8.12}$$

where ν^S and ν^E are the normal modes of the spring model Hessian and the exact Hessian, λ^E are the eigenvalues of the exact Hessian. Despite its simplicity, the spring model reproduces even the details of the shape of the exact spectrum, suggesting the model potential represents a good initial approximation to the real one.

In figure 8.8 we plot the number of force evaluations needed to converge the copper system to reach a force tolerance of 1e-5 eV/Åfor a range of A and P values. The least number of force evaluations locates at the vicinity of $log_{10}A = 0.2(A = 1.58), P = 7.5$, with only 15 force evaluations. The change of convergence rate agrees well with the condition number analysis shown in

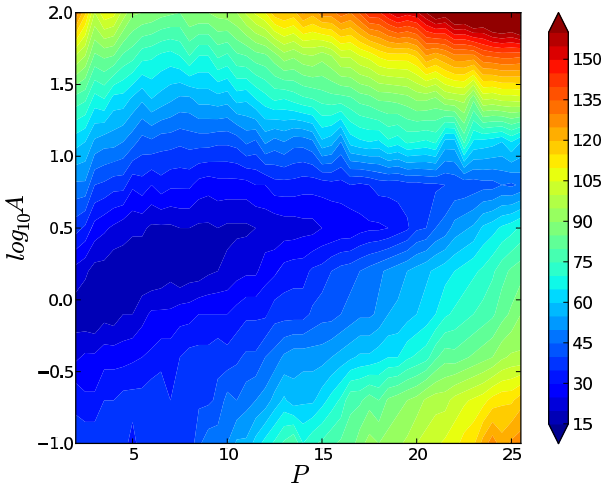

Figure 8.8: Number of force evaluations needed to reduce the force of Cu 27-atom bulk structure to be less than 1e-5 eV/Å, plotted against the changes of A and P.

figure 8.7a, that is, the smaller the condition number, the faster the rate of convergence. The influence of A is mainly on the size of the eigenvalues, and therefore the trail step size for each line search. For comparison same optimizations are done starting with the conventional unit-matrix Hessian and with the preconditioner $\beta = 10$, the number of force evaluations are 51 and 31.

Our result shows the potential improvement of the rate of convergence in homogeneous systems such as bulk metal, despite the simplicity of the spring model. When the system to be optimized includes different types of bonding, N_2 adsorption on gold surface for instance, the spring model is too simple. The universal parameters A and P can not separate the strong bonding in the molecule from the relatively weaker molecule-surface interaction and the Hessian fails in decouple the molecular stretching and the surface relaxing in the normal modes. A possible solution is to make A and P element dependent so that the strong molecular bond can be described.

8.3.3 Conclusion

In this chapter we studied the eigenvalue spectrum of the Hessian matrix of homogeneous bulk metal system, a power-law distribution was observed, with the majority of the eigenvalues locate in between 2 and 20. Setting a low eigenvalue

limit will reduce the influence of the anharmonicity of the weak eigenmodes to the rate of convergence. However, weak eigenmodes may not be fully relaxed after convergence criterion is reached, giving relative high energy and structure different from that of the minimum.

We adapted line search algorithm that fulfill Wolfe conditions and applied it within the BFGS algorithm to prevent the update of negative eigenvalues and therefore provides better rate of convergence. The new BFGS algorithm was scanned to find parameter set that works well on theoretical catalysis type of problems.The optimized BFGSLS algorithm outperforms all other optimizers tested.

An adaptive update method (AUM) was proposed for adjusting the preconditioners of the modes of the Hessian that are not updated during the minimization. The AUM set the preconditioners to be in the middle of the eigenvalue spectrum dynamically. Tests show that the AUM is able to adjust poorly set preconditioners in several steps and improve the convergence rate.

Finally, we use a model potential that describes bond stretching to calculate the Hessian matrix. Comparison with the exact Hessian shows that the model Hessian reproduce the vibrational modes qualitatively, despite its simplicity. For homogeneous systems, preconditioning the optimizer with the model Hessian reduces the condition number by 14 times and largely improves the convergence rate.

Chapter 9

Conclusion

In the present work, CO oxidation on various transition metals with different surface geometries were studied with density functional theory combined with microkinetic modeling. Adsorption state for different surface species and transition state for each elementary reaction were found and their total energies were calculated. Linear scaling between adsorption energies of intermediates and between adsorption energies and activation energies were established, enabling us to describe the overall reaction rate with only two parameters, adsorption energies of atomic oxygen and CO.

Microkinetic modeling was then applied with the Sabatier analysis, volcano plots that describe the upper bound of the reaction rate were constructed. From this analysis we found that the rate of CO oxidation is a clear function of the local geometry. For gold, when going from (111) $\rightarrow$ (211) $\rightarrow$ (532) $\rightarrow$ M12, the overall Sabatier rate increases at low temperature (273 K) as the coordination numbers of the surface active sites decreases, and gold M12 cluster sits right on top of the volcano. While for Pt and Pd points move away in the same order. As the temperature increases, the top of the volcano shifts to stronger adsorption energies, hence in the direction of the platinum.

We have also shown that the main effect behind the structure variation is related to the strength of the adsorbate-metal bond at different structures. As the coordination decreases, the d-band center of the active site gets higher and the

adsorbate-metal bond strength increases.

Adsorption energies of O and CO on Au-M-Au(111) bimetallic slabs were calculated, and show periodic trends based on the heterometals, with earlier transition metals inducing stronger adsorption on the Au surface. The results suggest that there is a large potential for tuning Au chemistry by incorporating other transition metals.

In the second part of the thesis, eigenvalue spectrum of the Hessian matrix of a homogeneous bulk metal system was calculated, a power-law distribution of the eigenvalues was observed, with the majority of the eigenvalues locate between 2 and 20. By setting a low eigenvalue limit, it is possible to increase the rate of optimization. However, weak eigenmodes may not be fully relaxed after convergence criterion is reached, giving relative high energy and structure different from that of the minimum.

We adapted line search algorithm that fulfill Wolfe conditions and applied it within the BFGS algorithm to prevent the update of negative eigenvalues and therefore provides better rate of convergence. The overall algorithm was parameterized and the parameter space is scanned to find parameter set that works well on theoretical catalysis type of problems.The optimized BFGSLS algorithm outperforms all other optimizers tested on respective.

We proposed an adaptive update method (AUM) for adjusting the preconditioners of the modes of the Hessian that are not updated during the minimization. The AUM set the preconditioners to be in the middle of the eigenvalue spectrum dynamically and improve the convergence rate generally.

Finally, we use a model potential that describes bond stretching to calculate the Hessian matrix. Despite its simplicity, the model Hessian reproduce the vibrational modes qualitatively. Applying the model Hessian as preconditioning matrix to homogeneous systems reduces the condition number by 14 times and largely improves the convergence rate.

Bibliography

[1] F. Abild-Pedersen and M. P. Andersson. Co adsorption energies on metals with correction for high coordination adsorption sites - a density functional study. *Surface Science*, 601(7):1747 – 1753, 2007.

[2] B. L. Abrams and J. P. Wilcoxon. Nanosize semiconductors for photooxidation. *Critical Reviews in Solid State and Materials Sciences*, 30(3):153–182, 2005.

[3] P. Atkins and J. de Paula. *Physical Chemistry*. Oxford University Press: Oxford, 8 edition, 2006.

[4] J Baker, A Kessi, and B Delley. The generation and use of delocalized internal coordinates in geometry optimization. *Journal of Chemical Physics*, 105(1):192–212, JUL 1 1996.

[5] C. Becker and C. R. Henry. Cluster size dependent kinetics for the oxidation of co on a pd/mgo(100) model catalyst. *Surface Science*, 352-354:457 – 462, 1996. Proceedings of the 15th European Conference on Surface Science.

[6] E. Bitzek, P. Koskinen, F. Gähler, M. Moseler, and P. Gumbsch. Structural relaxation made simple. *Physical Revew Letters*, 97(17):170201, Oct 2006.

[7] T. Bligaard, J. K. Nørskov, S. Dahl, J. Matthiesen, C.H. Christensen, and J. Sehested. The br¿nsted-evans-polanyi relation and the volcano curve in heterogeneous catalysis. *Journal of Catalysis*, 224(1):206 – 217, 2004.

[8] E. Boisselier and D. Astruc. Gold nanoparticles in nanomedicine: preparations, imaging, diagnostics, therapies and toxicity. *Chemical Society Reviews*, 38(6):1759–1782, 2009.

[9] G. C. Bond, C. Louis, and D. T. Thompson. *Catalysis by Gold*. Imperial College Press, 1. edition, 2006.

[10] G. C. Bond and D. T. Thompson. Catalysis by gold. *Catalysis Reviews-Science and Engineering*, 41(3-4):319–388, 1999.

[11] G. C. Bond and D. T. Thompson. Gold-catalysed oxidation of carbon monoxide. *Gold Bulletin*, 33(2):41–51, 2000.

[12] R. H. Byrd, J. Nocedal, and Y. Yuan. Global convergence of a class of quasi-newton methods on convex problems. *SIAM Journal on Numerical Analysis*, 24:1171–1190, 1987.

[13] B. D. Chandler, C. G. Long, J. D. Gilbertson, C. J. Pursell, G. Vijayaraghavan, and K. J. Stevenson. Enhanced oxygen activation over supported bimetallic au-ni catalysts. *The Journal of Physical Chemistry C*, 114(26):11498–11508, 2010.

[14] J. G. Chen, C. A. Menning, and M. B. Zellner. Monolayer bimetallic surfaces: Experimental and theoretical studies of trends in electronic and chemical properties. *Surface Science Reports*, 63(5):201 – 254, 2008.

[15] M. S. Chen and D. W. Goodman. The Structure of Catalytically Active Gold on Titania. *Science*, 306(5694):252–255, 2004.

[16] I. Chorkendorff and J. W. Niemantsverdriet. *Concepts of Modern Catalysis and Kinetics*. WILEY-VCH, 2003.

[17] A. Corma and H. Garcia. Supported gold nanoparticles as catalysts for organic reactions. *Chemical Society Reviews*, 37(9):2096–2126, 2008.

[18] Dacapo. http://wiki.fysik.dtu.dk/dacapo.

[19] W. C. Davidon. Variable metric method for minimization. *IAM Journal on Optimization*, 1:1–17, 1991.

[20] X. Y. Deng, B. K. Min, A. Guloy, and C. M. Friend. Enhancement of o2 dissociation on au(111) by adsorbed oxygen: Implications for oxidation catalysis. *Journal of the American Chemical Society*, 127(25):9267–9270, 2005. PMID: 15969608.

[21] J. E. Dennis and J. J. More. Quasi-newton methods, motivation and theory. *SIAM Review*, 19:46–89, 1977.

[22] M. V. Fernández-Serra, E. Artacho, and J. M. Soler. Model hessian for accelerating first-principles structure optimizations. *Physical Review B*, 67(10):100101, Mar 2003.

[23] M.V. Fernandez-Serra, E. Artacho, and J.M. Soler. Model Hessian for accelerating first-principles structure optimizations. *Physical Review B*, 67(10), MAR 1 2003.

[24] R. Ferro, A. Saccone, D. Maccio, and S. Delfino. A survey of gold intermetallic chemistry. *Gold Bullentin*, 36(2):39–50, 2003.

[25] R. P. Feynman. Forces in molecules. *Physical Review*, 56:340–343, 1939.

[26] T. H. Fischer and J. Almlof. General methods for geometry and wave function optimization. *The Journal of Physical Chemistry*, 96(24):9768–9774, 1992.

[27] R. Fletcher and M. J. D. Powell. A rapidly convergent descent dethod for minimization. *Computer Journal*, 6:163, 1963.

[28] P. Frondelius, A. Hellman, K. Honkala, H. Hakkinen, and H. Gronbeck. Charging of atoms, clusters, and molecules on metal-supported oxides: A general and long-ranged phenomenon. *Physical Review B*, 78(8), AUG 2008.

[29] A.C. Gluhoi, M.A.P. Dekkers, and B.E. Nieuwenhuys. Comparative studies of the n2o/h2, n2o/co, h2/o2 and co/o2 reactions on supported gold catalysts: effect of the addition of various oxides. *Journal of Catalysis*, 219(1):197 – 205, 2003.

[30] S. Goedecker, F. Lançon, and T. Deutsch. Linear scaling relaxation of the atomic positions in nanostructures. *Phys. Rev. B*, 64(16):161102, Sep 2001.

[31] L. Grabow, Y. Xu, and M. Mavrikakis. Lattice strain effects on co oxidation on pt(111). *Physical Chemistry Chemical Physics*, 8(29):3369–3374, 2006.

[32] J. D. Grunwaldt and A. Baiker. Gold/titania interfaces and their role in carbon monoxide oxidation. *The Journal of Physical Chemistry B*, 103(6):1002–1012, 1999.

[33] J. D. Grunwaldt, C. Kiener, C. Wögerbauer, and A. Baiker. Preparation of supported gold catalysts for low-temperature co oxidation via "size-controlled" gold colloids. *Journal of Catalysis*, 181(2):223 – 232, 1999.

[34] S. Guerin, B. E. Hayden, C. E. Lee, C. Mormiche, J. R. Owen, A. E. Russell, B. Theobald, and D. Thompsett. Combinatorial electrochemical screening of fuel cell electrocatalysts. *Journal of Combinatorial Chemistry*, 6(1):149–158, 2004. PMID: 14714999.

[35] B. Hammer, L. B. Hansen, and J. K. Nørskov. Improved adsorption energetics within density-functional theory using revised perdew-burke-ernzerhof functionals. *Physical Review B*, 59(11):7413–7421, Mar 1999.

[36] B. Hammer and J. K. Nørskov. Why gold is the noblest of all the metals. *Nature*, 376(6537):238–240, JUL 20 1995.

[37] B. Hammer and J. K. Nørskov. *Theory of adsorption and surface reactions*. Kluwer Academic Publishers, The Netherlands, 1997.

[38] B. Hammer and J. K. Nørskov. *Theoretical surface science and catalysis–calculations and concepts*, volume 45 of *Advances in Catalysis*. Academic Press, 2000.

[39] M. Haruta. Size- and support-dependency in the catalysis of gold. *Catalysis Today*, 36(1):153 – 166, 1997. Copper, Silver and Gold in Catalysis.

[40] M. Haruta, T. Kobayashi, H. Sano, and N. Yamada. Novel gold catalysts for the oxidation of carbon-monoxide at a temperature far below 0-degrees-C. *Chemistry Letters*, 2:405–408, 1987.

[41] M. Haruta, N. Yamada, T. Kobayashi, and S. Iijima. Gold catalysts prepared by coprecipitation for low-temperature oxidation of hydrogen and of carbon monoxide. *Journal of Catalysis*, 115(2):301 – 309, 1989.

[42] A. S. K. Hashmi and G. J. Hutchings. Gold catalysis. *Angewandte Chemie-International Edition*, 45(47):7896–7936, 2006.

[43] B. E. Hayden, D. Pletcher, J.-P. Suchsland, and L. J. Williams. The influence of pt particle size on the surface oxidation of titania supported platinum. *Physical Chemistry Chemical Physics*, 11(10):1564–1570, 2009.

[44] H. Hellmann. *Einfuhrung in die Quantumchemie*. Franz Duetsche,Leipzig, 1937.

[45] R. O. Jones and O. Gunnarsson. The density functional formalism, its applications and prospects. *Reviews of Modern Physics*, 61(3):689–746, Jul 1989.

[46] H. Jónsson, G. Mills, and K. W. Jacobsen. *Classical and Quantum Dynamics in Condensed Phase Simulations*. World Scientific, Singapore, 1998.

[47] J. R. Kitchin, J. K. Nørskov, M. A. Barteau, and J. G. Chen. Modification of the surface electronic and chemical properties of pt(111) by subsurface 3d transition metals. *The Journal of Chemical Physics*, 120(21):10240–10246, 2004.

[48] S. Kurth, J. P. Perdew, and P. Blaha. Molecular and solid-state tests of density functional approximations: LSD, GGAs, and meta-GGAs. *International Journal of Quantum Chemistry*, 75(4-5):889–909, NOV-DEC 1999. International Symposium on Atomic Molecular and Condensed Matter Theory, ST AUGUSTINE, FLORIDA, FEB 27-MAR 05, 1999.

[49] D. L. Lahr and S. T. Ceyer. Catalyzed co oxidation at 70 k on an extended au/ni surface alloy. *Journal of the American Chemical Society*, 128(6):1800–1801, 2006.

[50] H. F. Lang, S. Maldonado, K. J. Stevenson, and B. D. Chandler. Synthesis and characterization of dendrimer templated supported bimetallic pt-au nanoparticles. *Journal of the American Chemical Society*, 126(40):12949–12956, 2004. PMID: 15469292.

[51] S. J. Lee and A. Gavriilidis. Supported au catalysts for low-temperature co oxidation prepared by impregnation. *Journal of Catalysis*, 206(2):305 – 313, 2002.

[52] C. Lemire, R. Meyer, S. Shaikhutdinov, and H. J. Freund. Do quantum size effects control CO adsorption on gold nanoparticles? *Angewandte Chemie-International Edition*, 43(1):118–121, 2004.

[53] D.R. Lide. *Handbook of Chemistry and Physics*. C&C Press, Noca Raton, 87 edition, 2006-2007.

[54] S. D. Lin, M. Bollinger, and M. A. Vannice. Low temperature co oxidation over au/tio2 and au/sio2 catalysts. *Catalysis Letters*, 17:245–262, 1993. 10.1007/BF00766147.

[55] A. Logadottir, T. H. Rod, J. K. Nørskov, B. Hammer, S. Dahl, and C. J. H. Jacobsen. The brønsted-evans-polanyi relation and the volcano plot for ammonia synthesis over transition metal catalysts. *Journal of Catalysis*, 197(2):229 – 231, 2001.

[56] C. G. Long, J. D. Gilbertson, G. Vijayaraghavan, K. J. Stevenson, C. J. Pursell, and B. D. Chandler. Kinetic evaluation of highly active supported gold catalysts prepared from monolayer-protected clusters: An experimental michaelis-menten approach for determining the oxygen binding constant during co oxidation catalysis. *Journal of the American Chemical Society*, 130(31):10103–10115, 2008.

[57] N. Lopez, T. V. W. Janssens, B. S. Clausen, Y. Xu, M. Mavrikakis, T. Bligaard, and J. K. Nørskov. On the origin of the catalytic activity of gold nanoparticles for low-temperature co oxidation. *Journal of Catalysis*, 223(1):232 – 235, 2004.

[58] B. I. Lundqvist, O. Gunnarsson, H. Hjelmberg, and J. K. Nørskov. Theoretical description of molecule-metal interaction and surface reactions. *Surface Science*, 89(1-3):196 – 225, 1979.

[59] M. Mavrikakis, P. Stoltze, and J. K. Nørskov. Making gold less noble. *Catalysis Letters*, 64:101–106, 2000. 10.1023/A:1019028229377.

[60] B. E. Nieuwenhuys. Chemistry on single crystal surfaces of Pt and Pd alloys. *Surface Review and Letters*, 3(5-6):1869–1888, OCT-DEC 1996. Physics and Chemistry of Alloy Surfaces Seminar, KURORT RATHEN, GERMANY, APR 17-21, 1994.

[61] B.E. Nieuwenhuys, A.C. Gluhoi, E.D.L. Rienks, C.J. Weststrate, and C.P. Vinod. Chaos, oscillations and the golden future of catalysis. *Catalysis Today*, 100(1-2):49 – 54, 2005. 100th Anniversary Issue.

[62] A. Nilsson, L. G. M. Pettersson, and J. K. Nøskov, editors. *Chemical Bonding at Surfaces and Interfaces*. Elsevier, 2008.

[63] J. Nocedal. Theory of algorithms for unconstrained optimization. *Acta Numerica*, 1:199–242, 1992.

[64] J. Nocedal and S. J. Wright. *Numerical optimization*. Springer, 1999.

[65] J. K. Nørskov, T. Bligaard, B. Hvolbaek, F. Abild-Pedersen, I. Chorkendorff, and C. H. Christensen. The nature of the active site in heterogeneous metal catalysis. *Chemical Society Reviews*, 37:2163–2171, 2008.

[66] J. K. Nørskov, J. Rossmeisl, A. Logadottir, L. Lindqvist, J. R. Kitchin, T. Bligaard, and H. Jónsson. Origin of the overpotential for oxygen reduction at a fuel-cell cathode. *The Journal of Physical Chemistry B*, 108(46):17886–17892, 2004.

[67] M. Okumura, S. Nakamura, S. Tsubota, T. Nakamura, M. Azuma, and M. Haruta. Chemical vapor deposition of gold on al2o3, sio2, and tio2 for the oxidation of co and of h2. *Catalysis Letters*, 51:53–58, 1998. 10.1023/A:1019020614336.

[68] John P. Perdew, K. Burke, and M. Ernzerhof. Generalized gradient approximation made simple. *Physical Revew Letters*, 77(18):3865–3868, Oct 1996.

[69] John P. Perdew, J. A. Chevary, S. H. Vosko, Koblar A. Jackson, M. R. Pederson, D. J. Singh, and C. Fiolhais. Atoms, molecules, solids, and surfaces: Applications of the generalized gradient approximation for exchange and correlation. *Physical Review B*, 46(11):6671–6687, Sep 1992.

[70] W. H. Press, S. A. Teukolsky, W. T. Vetterling, and B. P. Flannery. *Numerical Recipes*. Cambridge Univ. Press, 1992.

[71] P. Pulay, G. Fogarasi, F. Pang, and J. E. Boggs. Systematic ab initio gradient calculation of molecular geometries, force constants, and dipole moment derivatives. *Journal of the American Chemical Society*, 101(10):2550–2560, 1979.

[72] S. N. Rashkeev, A. R. Lupini, S. H. Overbury, S. J. Pennycook, and S. T. Pantelides. Role of the nanoscale in catalytic co oxidation by supported au and pt nanostructures. *Physical Review B*, 76(3):035438, Jul 2007.

[73] D. Ricci, A. Bongiorno, G. Pacchioni, and U. Landman. Bonding trends and dimensionality crossover of gold nanoclusters on metal-supported MgO thin films. *Physical Review Letters*, 97(3), JUL 21 2006.

[74] A. V. Ruban, H. L. Skriver, and J. K. Nørskov. Surface segregation energies in transition-metal alloys. *Physical Review B*, 59(24):15990–16000, Jun 1999.

[75] A. Sanchez, S. Abbet, U. Heiz, W. D. Schneider, H. Hakkinen, R. N. Barnett, and U. Landman. When gold is not noble: Nanoscale gold catalysts. *Journal of Physical Chemistry A*, 103(48):9573–9578, DEC 2 1999.

[76] M. A. Sanchez-Castillo, C. Couto, W. B. Kim, and J. A. Dumesic. Gold-nanotube membranes for the oxidation of CO at gas-water interfaces. *Angewandte Chemie-International Edition*, 43(9):1140–1142, 2004.

[77] S. Schimpf, M. Lucas, C. Mohr, U. Rodemerck, A. Brückner, J. Radnik, H. Hofmeister, and P. Claus. Supported gold nanoparticles: in-depth catalyst characterization and application in hydrogenation and oxidation reactions. *Catalysis Today*, 72(1-2):63 – 78, 2002.

[78] H. B. Schlegel. ESTIMATING THE HESSIAN FOR GRADIENT-TYPE GEOMETRY OPTIMIZATIONS. *Theoretica Chimica Acta*, 66(5):333–340, 1984.

[79] M. M. Schubert, S. Hackenberg, A. C. van Veen, M. Muhler, V. Plzak, and R. J. Behm. Co oxidation over supported gold catalysts–"inert" and "active" support materials and their role for the oxygen supply during reaction. *Journal of Catalysis*, 197(1):113 – 122, 2001.

[80] Shaikhutdinov, Sh.K. and Meyer, R. and Naschitzki, M. and Bäumer, M. and Freund, H.-J. Size and support effects for co adsorption on gold model catalysts. *Catalysis Letters*, 86:211–219, 2003. 10.1023/A:1022616102162.

[81] P. Stoltze. *Simulation methods in atomic-scale materials physics*. Polyteknish Forlag, 1997.

[82] M. Turner, V. B. Golovko, O. P. H. Vaughan, P. Abdulkin, A. Berenguer-Murcia, M. S. Tikhov, B. F. G. Johnson, and R. M. Lambert. Selective oxidation with dioxygen by gold nanoparticle catalysts derived from 55-atom clusters. *Nature*, 454(7207):981–983, 08 2008.

[83] M. Valden, X. Lai, and D. W. Goodman. Onset of Catalytic Activity of Gold Clusters on Titania with the Appearance of Nonmetallic Properties. *Science*, 281(5383):1647–1650, 1998.

[84] D. Vanderbilt. Soft self-consistent pseudopotentials in a generalized eigenvalue formalism. *Physical Review B*, 41(11):7892–7895, Apr 1990.

[85] J. P. Wilcoxon and B. L. Abrams. Synthesis, structure and properties of metal nanoclusters. *Chemical Society Reviews*, 35(11):1162–1194, 2006.

[86] P. Wolfe. Convergence conditions for ascent methods. *SIAM Review*, 11(2):226–235, 1969.

[87] Y. Z. Yuan, K. Asakura, H. L. Wan, K. Tsai, and Y. Iwasawa. Preparation of supported gold catalysts from gold complexes and their catalytic activities for co oxidation. *Catalysis Letters*, 42:15–20, 1996. 10.1007/BF00814461.

[88] R. Zanella, S. Giorgio, C. H. Shin, C. R. Henry, and C. Louis. Characterization and reactivity in co oxidation of gold nanoparticles supported on tio2 prepared by deposition-precipitation with naoh and urea. *Journal of Catalysis*, 222(2):357 – 367, 2004.

[89] Y. Zhang and W. Yang. Comment on "generalized gradient approximation made simple". *Physical Revew Letters*, 80(4):890, Jan 1998.

VIP Gold Catalysis

DOI: 10.1002/anie.200801479

Trends in the Catalytic CO Oxidation Activity of Nanoparticles**

*Hanne Falsig, Britt Hvolbæk, Iben S. Kristensen, Tao Jiang, Thomas Bligaard, Claus H. Christensen, and Jens K. Nørskov**

Although extended gold surfaces are generally considered chemically inert[1,2] nanosized (< 5 nm) gold particles can be very effective catalysts for a number of oxidation reactions.[3–17] There are reports of similar size effects for silver catalysts.[18,19] The origin of the nanoeffects in the catalytic properties of these metals is widely debated,[15] and no consensus has been reached. Based on a set of density functional theory calculations of the full reaction pathway for CO oxidation over extended surfaces as well as over small nanoparticles of a number of metals, we show that although platinum and palladium are the most active catalysts for extended surfaces at high temperatures, gold is the most active for very small particles at low temperature. The calculations capture the special catalytic properties of nanosized particles observed experimentally, which allows the origin of the effect to be analyzed.

Herein, we focus on intrinsic metal effects; that is, we do not include additional possible effects that involve the support. It is not that such effects may not be important,[5,20,21] but it is useful to first establish the intrinsic metal effects,[15] in particular as it has been shown experimentally that nanostructured gold with no support is also catalytically active.[22,23] The key feature of our analysis is that we compare catalytic activities of different transition and noble metals for one specific reaction, the CO oxidation.

The CO oxidation reaction on close-packed fcc(111) surfaces was considered initially, which will give a dominant contribution to the total catalytic rate over large metal particles. We consider the following elementary reactions:

$$CO + * \rightleftharpoons CO* \quad (R1)$$

$$O_2 + * \rightleftharpoons O_2* \quad (R2)$$

$$O_2* + * \rightleftharpoons 2\,O* \quad (R3)$$

$$O* + CO* \rightleftharpoons CO_2 + 2* \quad (R4)$$

For the metals we consider herein, Reactions (R1) and (R2) are unactivated and fast, and we assume that these two reactions are in equilibrium. This means that we are limited to temperatures high enough that desorption is also fast. The possible formation of an oxide layer on the more reactive metals is neglected.

The forward and reverse rate constants of the Reactions (R3) and (R4) are given by $k_i = \nu_i \exp[-\Delta G_{ai}/kT] = \nu_i \exp[-(E_{ai} - T\Delta S_{ai})/kT]$, where ν_i is a prefactor, E_{ai} is the activation energy, k is the Boltzmann constant, and T is the absolute temperature. The activation energies are $E_a = \max(E_{TS} - E_{IS}, 0)$ where E_{IS} is the initial state energy and E_{TS} is the transition-state energy. ΔS_{ai} is the entropy difference between the transition state and the initial state. The entropy of adsorbed species are assumed to be zero, and the gas-phase entropies are taken from Ref. [24]. The adsorption energies of the different species E_{CO}, E_{O_2}, and E_O and the transition state energies are given with respect to the gas-phase molecules.

Assuming the prefactors and adsorption entropies are independent of the metal, there are five metal-dependent parameters determining the kinetics: E_{CO}, E_{O_2}, E_O, E_{TS3}, and E_{TS4}. The transition-state energies are, however, found to scale linearly with the adsorption energies, as shown for E_{TS3} and E_{TS4} in Figure 1a and b. Such Brønsted–Evans–Polanyi (BEP) relations are found quite generally for surface reactions.[25] Furthermore, the O_2 adsorption energy scales with the O adsorption energy (Figure 1c). This means that the adsorption energies E_{CO} and E_O can be viewed, to a first approximation, as the only independent variables characterizing the metal in the microkinetic model. Owing to the low number of elementary reactions, it is possible to find an analytical solution for this microkinetic model. Herein, we use instead the more general method of a so-called Sabatier analysis to find an upper bound to the overall reaction rate.[26]

The Sabatier rate[26] is the rate the reaction will have if all coverages are optimum for each elementary reaction step. Such conditions may not be obtainable in reality, but the Sabatier rate still provides an exact upper bound to the steady-state rate under any reaction conditions. The Sabatier rate is also an upper bound on the rate when islanding is included, as that will decrease the number of possible reaction centers to the length of the boundary between different phases.[27] The Sabatier rate thus forms a good measure of the intrinsic ability of a given metal surface to catalyze the reaction in question. The metal with the highest Sabatier rate is taken herein as being the best catalyst.

[*] Dr. B. Hvolbæk, I. S. Kristensen, T. Jiang, Dr. T. Bligaard, Prof. J. K. Nørskov
Center for Atomic-scale Materials Design, Department of Physics, Technical University of Denmark, DK-2800 Lyngby (Denmark)
Fax: (+45)4593-2399
E-mail: norskov@fysik.dtu.dk
H. Falsig, Prof. C. H. Christensen
Center for Sustainable and Green Chemistry, Department of Chemistry, Technical University of Denmark
DK-2800 Lyngby (Denmark)

[**] The Center for Sustainable and Green Chemistry is supported by the Danish National Research Foundation, and the Center for Atomic-scale Materials Design is supported by the Lundbeck Foundation. In addition we thank the Danish Research Council for the Technical Sciences and the NABIIT program for financial support, and Danish Center for Scientific Computing for computer time.

Supporting information for this article is available on the WWW under http://dx.doi.org/10.1002/anie.200801479.

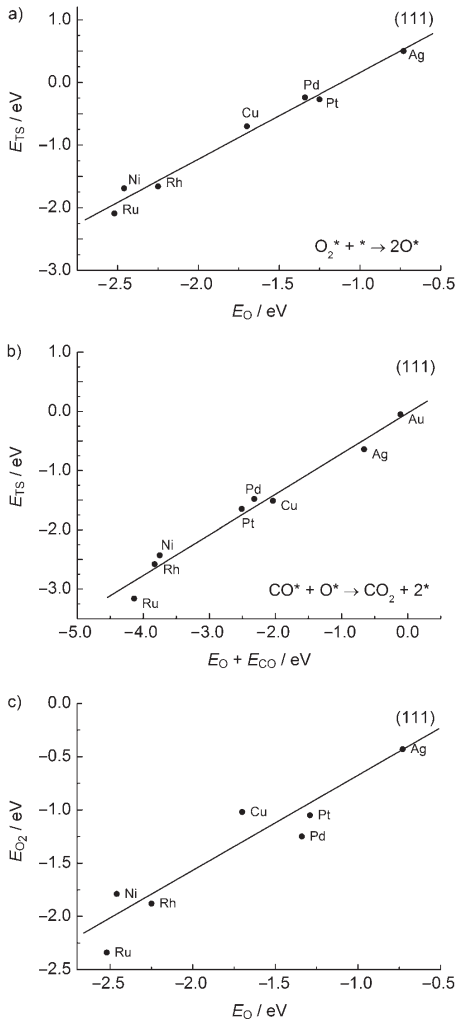

Figure 1. The BEP and scaling relations for different close-packed fcc(111)-surfaces. a) Calculated transition-state energies for O_2 dissociation (R3) as a function of oxygen adsorption energy. $E_{TS3} = 1.39\,E_O + 1.56$ eV. b) Calculated transition-state energies for adsorbed CO reacting with adsorbed O (R4) as a function of the sum of the O and CO adsorption energies. $E_{TS4} = 0.70(E_O + E_{CO}) + 0.02$ eV. c) The scaling of the O_2 adsorption energy with the oxygen adsorption energy $E_{O_2} = 0.89E_O + 0.17$ eV. For Pt(111,) the calculated reaction barrier $E_a = E_{TS} - (E_{CO} + E_O)$ for CO* + O* ⇄ CO_2 + 2* is 0.85 eV, in good agreement with calculations.[28,29]

The rate of reaction for (R3) and (R4) are maximized if the reverse reactions are neglected. The Sabatier rate is therefore calculated from the forward rates:

$$r_3^+ = \theta_{O_2}\theta_* k_3^+ = \theta_{O_2}\theta_* \nu_3 \exp[-(E_{a3} - T\,\Delta S_{a3})/k\,T] \quad (1)$$

$$r_4^+ = \theta_O\theta_{CO} k_4^+ = \theta_O\theta_{CO} \nu_4 \exp[-(E_{a4} - T\,\Delta S_{a4})/k\,T] \quad (2)$$

where θ_{O_2} is the coverage of adsorbed oxygen molecules, θ_O is the coverage of adsorbed atomic oxygen, θ_{CO} is the coverage of adsorbed CO molecules, and θ_* is the coverage of free sites of the surface. The coverages will depend on the reaction conditions, temperature, reactant pressures, and conversion.

For the present case, the optimum coverages are found by first neglecting the coverage of atomic oxygen. Still assuming that (R1) and (R2) are in equilibrium, this gives:

$$\theta_*^{max} = \frac{1}{1 + K_1\,p(CO) + K_2\,p(O_2)} \quad (3)$$

where K_1 and K_2 are the equilibrium constants for (R1) and (R2), and $p(CO)$ and $p(O_2)$ are the partial pressures of CO and O_2. The optimum coverages of CO and O_2 have similar expressions, namely $\theta_{CO}^{max} = K_1 p(CO)\theta_*$ and $\theta_{O_2}^{max} = K_2 p(O_2)\theta_*$.

The Sabatier rates of each of the Reactions (R3) and (R4) are found by using the forward rates from (1) and (2) with the coverages of θ^{max}, θ_{CO}^{max} and $\theta_{O_2}^{max}$ from (3), and the coverage of θ_O^{max} set to one.

$$r_3^{S\,max} = k_3^+ \theta_{O_2}^{max}\theta_*^{max} \quad (4)$$

$$r_4^{S\,max} = k_4^+ \theta_{CO}^{max}\theta_O^{max} = k_4^+ \theta_{CO}^{max} \quad (5)$$

The Sabatier rate of forming CO_2 is determined by the lowest of the Sabatier rates of Reaction (R3) and (R4):

$$r_S = \min\{2\,r_3^{S\,max}, r_4^{S\,max}\} \quad (6)$$

where the factor of 2 stems from the stoichiometric number for (R3).

Figure 2 shows a contour plot of the Sabatier activity over close-packed surfaces. The Sabatier rate is calculated at $T = 600$ K, $P_{O_2} = 0.33$ bar and $P_{CO} = 0.67$ bar, corresponding to high-temperature CO oxidation conditions. The two-dimensional volcano plots show that, of the elemental metals, platinum and palladium are closest to the top. This agrees well with experimental evidence.[30] Platinum and palladium are

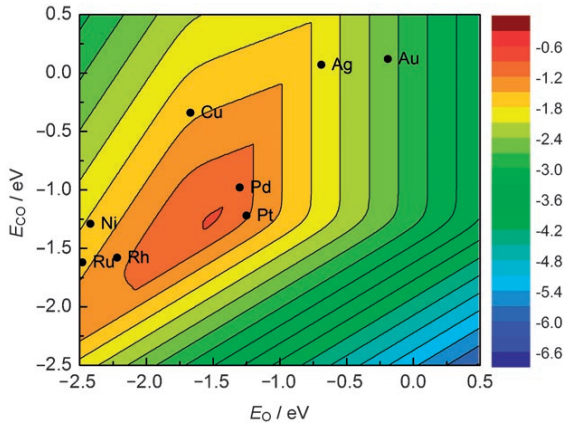

Figure 2. Contour plot of the Sabatier activity $A_S = kT\ln[r_S/\nu]$ over close-packed surfaces as a function of E_{CO} and E_O (ν is set to kT/h) under high-temperature conditions ($T = 600$ K, $P_{O_2} = 0.33$ bar, and $P_{CO} = 0.67$ bar). The values for different elemental metals can be taken from their indicated positions.

excellent CO oxidation catalysts, used for example in car exhaust after-treatment. This result is completely in line with DFT calculations and kinetic modeling by Grabow et al.[31] showing that at low temperatures, platinum without strain has a higher activity than either compressed (weaker bond energies) or expanded (stronger bond energies) platinum surfaces.

The reactivity of nanoparticles was then investigated. One important feature of nanoparticles is that the relative fraction of low-coordinate corner atoms to surface atoms is very large.[15,32] We concentrate herein on the reactivity of corner atoms, and model these by carrying out calculations for metal clusters containing twelve atoms, in the structure shown as inserts in Figure 3. All the twelve atoms in the cluster are held fixed with a lattice constant corresponding to the bulk value to mimic a geometrically constrained corner of a larger cluster, such as those in the range 2–5 nm studied experimentally. The calculations are thus more intended to model a general corner site on nanoparticles than specifically a twelve-atom cluster, as such small clusters will have much larger structural flexibility.[33]

It turns out that adsorption is considerably more exothermic on the twelve-atom clusters than on the close-packed surfaces. This makes it important to include another elementary reaction, as the coverage of molecular O_2 may be large enough such that an associative mechanism[34] may be important:

$$O_2{*} + CO{*} \rightleftharpoons CO_2 + O{*} + {*} \qquad \text{(R5)}$$

For the (111) surfaces, the weak bonding of O_2 combined with the reaction barrier for the process makes it unimportant for platinum[27] and less reactive metals.[35]

As for the fcc(111) surface, correlations between the transition state energies, E_{TS3}, E_{TS4}, and E_{TS5}, and the binding energies, E_O and E_{CO}, are found for the twelve-atom cluster. A scaling between E_{O_2} and E_O is also found. These relations are shown in Figure 3. The linear relations are similar to those of the close-packed surfaces (Figure 1), except that the adsorption energy axis has shifted. The adsorption energy of both CO and O are substantially more negative (exothermic adsorption) on the corner sites than on the close packed surfaces; compare for example, the adsorption energy of O on the (111) surfaces to those on the twelve-atom cluster: on the latter the bond is stronger by of the order 0.5 eV. The same trend is seen for molecular CO adsorption.

The expressions for the optimum coverages and the Sabatier rate for (R3) and (R4) are the same as for the fcc(111) surface. For (R5), the Sabatier rate is:

$$r_5^{S\max} = k_5^{+}\theta_{CO}^{\max}\theta_{O_2}^{\max} \qquad (7)$$

Both Reaction (R3) and (R5) dissociate O_2, and can be followed by Reaction (R4) creating CO_2. The Sabatier activity is therefore given by:

$$r_S = \max\{2\min\{r_5^{S\max}, r_4^{S\max}\}, \min\{2r_3^{S\max}, r_4^{S\max}\}\} \qquad (8)$$

Figure 4 shows the contour plot of the Sabatier activity, $A_S = kT\ln[r_S/\nu]$. In this case, gold is closest to the top, followed by palladium and silver.

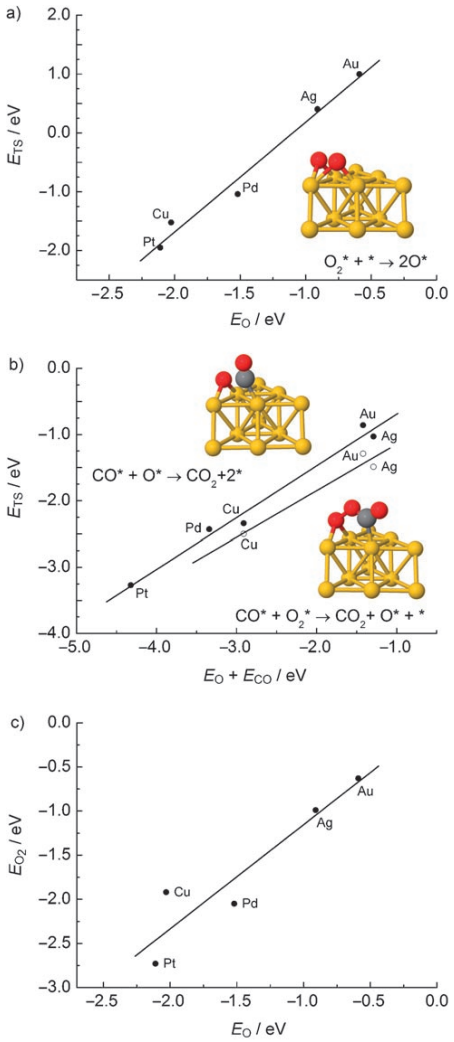

Figure 3. The BEP relations and scaling relation for different twelve-atom clusters. a) Calculated transition-state energies for O_2 dissociation (R3) as a function of oxygen adsorption energy. $E_{TS3} = 1.87\,E_O + 2.04$ eV. b) Calculated transition-state energies for adsorbed CO reacting with adsorbed O (R4) and O_2 (R5) as a function of the sum of the O and CO adsorption energies. $E_{TS4} = 0.78\text{-}(E_O + E_{CO}) + 0.09$ eV and $E_{TS5} = 0.70(E_O + E_{CO}) - 0.44$ eV. c) The scaling of the O_2 adsorption energy with the O adsorption energy $E_{O_2} = 1.18\,E_O + 0.03$ eV. Transition states for the reactions on the Au_{12} cluster are shown as inserts.

The results in Figure 2 and Figure 4 are in good agreement with available experimental observations.[3,32] It shows that the relative activities of different metals can be theoretically estimated, and it provides a clear picture of the catalyst properties determining the best catalysts in terms of the adsorption energies of the intermediates. The volcano plots of Figure 2 and Figure 4 can be viewed as an illustration of the Sabatier principle, with the important new feature that we know which adsorption energy that provides the optimum

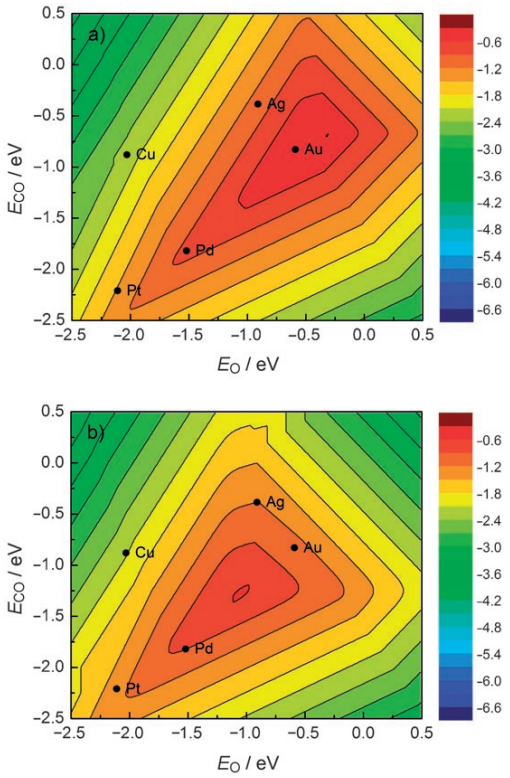

Figure 4. Contour plot of the Sabatier rate as a function of the CO and O adsorption energies on the twelve-atom clusters. The values for some elemental metals are shown. a) The activity under typical experimental conditions for CO oxidation by gold nanoparticles (T=273 K, P_{O_2}=0.21 bar, and P_{CO}=0.01) and b) the activity under high-temperature conditions (T=600 K, P_{O_2}=0.33 bar, and P_{CO}=0.67 bar).

catalyst. The position of the maximum in terms of adsorption energies depends slightly on the structure, which is related to the fact that the relationship between adsorption energy and activation energy is somewhat structure dependent. More importantly, it can be seen that the metals corresponding to a particular adsorption energy shift substantially depending on the coordination number of the metal atom. This is true for all the metals considered, and it is the dominant reason for gold becoming the best elemental catalyst for the low-coordinate sites. The shift is of the same order of magnitude as the difference between neighboring metals in the periodic table, explaining why it appears as if the top of the volcano has shifted by a little less than one place to the right in the periodic table from Figure 2 to Figure 4.

Comparing the volcanoes in Figure 2 and Figure 4, it is clear that for gold, the corner atoms will dominate over the close-packed surfaces for even quite large particles, as the value of r_S is many orders of magnitude larger in this case. For platinum, on the other hand, the difference is only about an order of magnitude. It should be noted that even for platinum, small particles could still be more active than larger ones, but only because the surface area per mass of catalyst is larger (scaling as d^{-1}).

The present analysis suggests that the more noble metals move to the maximum in the reactivity volcano when lower-coordinated metal atoms serve as active sites for the reaction. It suggests that similar results could be found for other reactions. For oxidation reactions, the best extended surface catalysts are already quite noble: platinum and palladium, and gold is the next, less reactive metal. For reactions involving less reactive molecules, such as N_2, we would expect that the best nanoparticle catalysts would not be gold but metals just to the right in the periodic table of the most active metals (ruthenium, iron) for this reaction, for example, cobalt or nickel. It is therefore possible that pronounced nanoeffects in catalysis is not restricted to gold.

In summary, we have modeled the special catalytic properties of nanosized particles observed experimentally, and analyzed the origin of the effect. The ability of the metal atoms to activate reactants change substantially as the coordination number of the active metal site is reduced at corners of metal particles. This model supports the hypothesis that part of the observed reactivity of gold nanoparticles is independent of the substrate.

Received: March 23, 2008
Published online: May 21, 2008

Keywords: carbon monoxide · density functional calculations · gold · heterogeneous catalysis · nanostructures

[1] D. T. Wickham, D. H. Parker, G. N. Kastanas, M. A. Lazaga, B. E. Koel, *Prepr. Am. Chem. Soc. Div. Pet. Chem.* **1992**, *37*, 1034.
[2] B. Hammer, J. K. Nørskov, *Nature* **1995**, *376*, 238–240.
[3] M. Haruta, T. Kobayashi, H. Sano, N. Yamada, *Chem. Lett.* **1987**, 405–408.
[4] M. Valden, X. Lai, D. W. Goodman, *Science* **1998**, *281*, 1647–1650.
[5] G. C. Bond, D. T. Thomson, *Catal. Rev. Sci. Eng.* **1999**, *41*, 319–388.
[6] M. A. P. Dekkers, M. J. Lippits, B. E. Nieuwenhuys, *Catal. Today* **1999**, *54*, 381.
[7] S. Carrettin, P. McMorn, P. Johnston, K. Griffin, G. J. Hutchings, *Chem. Commun.* **2002**, 696–697.
[8] S. Schimpf, M. Lucas, C. Mohr, U. Rodemerck, A. Brückner, J. Radnik, H. Hofmeister, P. Claus, *Catal. Today* **2002**, *72*, 63–78.
[9] S. Carrettin, P. McMorn, P. Johnston, K. Griffin, C. J. Kiely, G. A. Attard, G. J. Hutchings, *Top. Catal.* **2004**, *27*, 131–136.
[10] R. Meyer, C. Lemire, S. Shaikhutdinov, H. J. Freund, *Gold Bull.* **2004**, *37*, 72–133.
[11] A. Abad, P. Concepcion, A. Corma, H. Garcia, *Angew. Chem.* **2005**, *117*, 4134–4137; *Angew. Chem. Int. Ed.* **2005**, *44*, 4066–4069.
[12] A. C. Gluhoi, N. Bogdanchikova, B. E. Nieuwenhuys, *J. Catal.* **2005**, *229*, 154–162.
[13] M. D. Hughes et al., *Nature* **2005**, *437*, 1132–1135.
[14] T. A. Nijhuis, M. Makkee, J. A. Moulijn, B. M. Weckhuysen, *Ind. Eng. Chem. Res.* **2006**, *45*, 3447–3459.
[15] a) T. V. W. Janssens, B. S. Clausen, B. Hvolbæk, H. Falsig, C. H. Christensen, T. Bligaard, J. K. Nørskov, *Top. Catal.* **2007**, *44*, 15–26; b) N. Lopez, T. V. W. Janssens, B. S. Clausen, Y. Xu, M. Mavrikakis, T. Bligaard, J. K. Nørskov, *J. Catal.* **2004**, *223*, 232–235.
[16] C. H. Christensen, B. Jørgensen, J. Rass-Hansen, K. Egeblad, R. Madsen, S. K. Klitgaard, S. M. Hansen. M. R. Hansen, H. C.

Andersen, A. Riisager, *Angew. Chem.* **2006**, *118*, 4764 – 4767; *Angew. Chem. Int. Ed.* **2006**, *45*, 4648 – 4651.
[17] R. Burch, *Phys. Chem. Chem. Phys.* **2006**, *8*, 5483 – 5500.
[18] M. J. Lippits, A. C. Gluhoi, B. E. Nieuwenhuys, *Top. Catal.* **2007**, *44*, 159 – 165.
[19] L. Gang, B. G. Anderson, J. van Grondelle, R. A. van Santen, *Appl. Catal. B* **2003**, *40*, 101 – 110.
[20] M. Haruta, *Catal. Today* **1997**, *36*, 153 – 166.
[21] B. Hammer, *Top. Catal.* **2006**, *37*, 3 – 16.
[22] C. Xu, J. Su, X. Xu, P. Liu, H. Zhao, F. Tian, Y. Ding, *J. Am. Chem. Soc.* **2007**, *129*, 42 – 43.
[23] B. Jürgens, C. Kübel, C. Schultz, T. Nowitzki, V. Zielasek, J. Biener, M. M. Biener, A. V. Hamza, M. Bäumer, *Gold Bull.* **2007**, *40*, 142 – 148.
[24] P. Atkins, J. de Paula, *J. Physical Chemistry* , 8th ed. Oxford University Press, Oxford, **2006**.
[25] J. K. Nørskov et al., *J. Catal.* **2002**, *209*, 275 – 278.
[26] T. Bligaard, J. K. Nørskov, S. Dahl, J. Matthiesen, C. H. Christensen, J. Sehested, *J. Catal.* **2004**, *224*, 206 – 217.
[27] J. Wintterlin, S. Völkening, T. V. W. Janssens, T. Zambelli, G. Ertl, *Science* **1997**, *278*, 1931 – 1933.
[28] Z.-P. Liu, P. Hu, *Top. Catal.* **2004**, *28*, 71 – 78.
[29] A. Eichler, J. Hafner, *Surf. Sci.* **1999**, *433*, 58 – 62.
[30] B. E. Nieuwenhuys, *Surf. Rev. Lett.* **1996**, *3*, 1869 – 1888.
[31] L. Grabow, Y. Xu, M. Mavrikakis, *Phys. Chem. Chem. Phys.* **2006**, *8*, 3369 – 3374.
[32] A. Carlsson, A. Puig-Molina, T. V. W Janssens, *J. Phys. Chem. B* **2006**, *110*, 5286 – 5293.
[33] G. Mills, M. S. Gordon, H. Metiu, *J. Chem. Phys.* **2003**, *118*, 4198 – 4205.
[34] Z.-P. Liu, P. Hu, A. Alavi, *J. Am. Chem. Soc.* **2002**, *124*, 14770 – 14779.
[35] L. M. Molina, B. Hammer, *Phys. Rev. B* **2004**, *69*, 155424.

Journal of Catalysis 260 (2008) 86–92

Contents lists available at ScienceDirect

Journal of Catalysis

www.elsevier.com/locate/jcat

Oxidation of CO and H_2 by O_2 and N_2O on Au/TiO_2 catalysts in microreactors

G. Walther [a], D.J. Mowbray [a], T. Jiang [a], G. Jones [a], S. Jensen [b], U.J. Quaade [c], S. Horch [a,*]

[a] Center for Atomic-scale Materials Design (CAMD), Department of Physics, Technical University of Denmark, DK-2800 Kgs. Lyngby, Denmark
[b] Department of Micro and Nanotechnology (DTU Nanotech), Technical University of Denmark, DK-2800 Kgs. Lyngby, Denmark
[c] Center for Individual Nanoparticle Functionality (CINF), Department of Physics, Technical University of Denmark, DK-2800 Kgs. Lyngby, Denmark

ARTICLE INFO

Article history:
Received 31 July 2008
Revised 3 September 2008
Accepted 4 September 2008
Available online 1 October 2008

Keywords:
Gold
Nanoparticles
Catalysis
Microreactor
Carbon monoxide
Hydrogen
Oxygen
Nitrous oxide
Particle size
Sintering
TEM

ABSTRACT

We performed steady-state activity measurements in microreactors to obtain the reaction rates for CO and H_2 oxidation. These reactions were studied on three different gold particle sizes ($d \approx 3.6, 5.7, 16.2$ nm) using either O_2 or N_2O as oxidizing agents. From our TEM analysis, our CO oxidation rates follow the d^{-3} relationship proposed in Hvolbæk et al. [B. Hvolbæk, T.V.W. Janssens, B.S. Clausen, H. Falsig, C.H. Christensen, J.K. Nørskov, Nano Today 2 (2007) 14–18]. Density functional theory (DFT) calculations on a Au{532} surface and a Au_{12} cluster, which model corner sites, reproduced the apparent activation barriers of about 37 kJ mol^{-1} for CO oxidation on the smallest nanoparticles by both O_2 and N_2O. For all of the reactions studied, we found the overall activation barrier depended only on the size of the TiO_2 supported gold nanoparticle.

1. Introduction

In the past, gold was not thought to be catalytically active, and was even called “the noblest of all the metals” [1]. However, the discovery by Haruta et al. [2] that nanoparticulate gold is catalytically active for CO oxidation, has provoked an academic “gold rush.” This is evidenced by the exponential increase in gold catalysis publications since the early 1990s [3–6].

Many different experimental studies have been performed to understand gold’s activity for CO oxidation. These investigations considered changes of the particle’s morphology [7,8], a structure–activity relationship [9–11], the activity of unsupported nanoporous bulk gold [12,13], and the influence of the support on the activity [14]. CO oxidation has also been thoroughly studied theoretically using density functional theory (DFT) [1,6,15–19]. Besides CO oxidation, many other reactions have been studied on gold catalysts. These include the oxidation of hydrocarbons [5,20–24] and oxygen-containing hydrocarbons [3–5,21,25] as well as the catalytic hydrogenation of organic compounds [4,5,26].

In particular, CH_4 oxidation includes in the tail of its oxidation pathway CO oxidation and H_2 oxidation, since it only forms CO_2 and H_2 on gold catalysts [27]. Since there is a keen interest in converting CH_4 into more valuable monocarbon chemicals, it is necessary to first identify both the reaction pathway and active sites for CO and H_2 oxidation by different oxidizing agents.

The reason for this surprising activity is still under debate. After the pioneering work of Haruta [28], the activity of gold has been linked to several different effects. These include quantum-size effects [9], support-induced strain [15], charge transfer from the small gold particles to adsorbed O_2 [29] and the role of low-coordinated gold atoms [6,15,17–19].

It has recently been demonstrated that the CO oxidation activity of gold nanoparticles is inversely proportional to the cube of the average particle size ($\sim d^{-3}$), independent of the support material used [30]. This suggests that it is the corner sites which are the most active for CO oxidation by O_2.

The common oxidizing agent for CO oxidation, used in all the above studies was O_2. Very few studies deal with other oxidation agents, such as N_2O, and they focus on the decomposition and reduction of N_2O [31]. Since N_2O is known to readily dissociate into adsorbed atomic O and gas phase N_2 in the presence of CO, the oxidation of CO by N_2O involves atomic O. On the other hand, CO oxidation using O_2 has been shown to also occur via an alternative pathway, which does not include O_2 dissociation [16,32]. By using these two different oxidizing agents, we may experimentally

* Corresponding author.
E-mail address: horch@fysik.dtu.dk (S. Horch).

0021-9517/$ – see front matter
doi:10.1016/j.jcat.2008.09.003

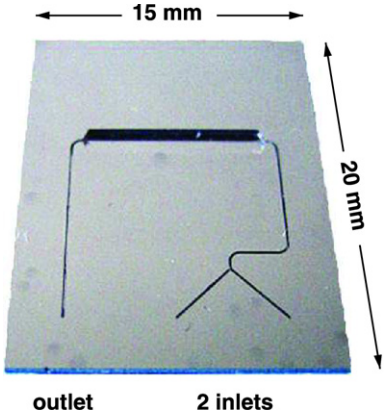

Fig. 1. Unloaded microreactor, based on silicon, with two inlets to mix gases on the chip, a (8.0 × 1.5 × 0.2) mm^3 reactor chamber and a single outlet.

compare Au nanoparticle activity for two different CO oxidation pathways.

In the present contribution, we compare the reaction rates for CO and H_2 oxidation on three different particle sizes using either O_2 or N_2O as the oxidizing agent. To corroborate our experimental findings, we also modeled the CO oxidation turnover frequency using DFT calculations on the Au{532} surface and Au_{12} cluster in a microkinetic model. Our findings suggest that such a model quantitatively describes the kinetics of CO oxidation using small Au nanoparticles ($d \lesssim 5$ nm).

2. Methods

2.1. Experimental equipment

All experiments were performed in microreactors, based on deep reactive ion-etched (DRIE) silicon wafers. Details of the fabrication process are provided in Ref. [33]. Fig. 1 illustrates the 280 μm deep capillary system that allows mixing of undiluted gases on the chip, without any danger of explosion. The dimensions of the reactor chamber are (8.0 × 1.5 × 0.2) mm^3. The whole device measures 20 mm × 15 mm × 0.35 mm and is sealed with a Viton sheet. The inlet and outlet holes are sealed with Viton O-rings to a heatable interface block that connects the external tubing to the microreactor. The temperature was measured with a K-type thermocouple and controlled using a PID-controller (Eurotherm). The gas flow was controlled by mass flow controllers (Bronkhorst), operating in the range from 0.02 to 1.00 ml min^{-1} with a precision of 0.02 ml min^{-1} at 1 bar.

The reaction products were analyzed using an Agilent gas chromatograph (3000A microGC). The GC has combined columns of 10 m molecular sieve and 3 m PLOT U with 1.0 μl back-flushing, which allows simultaneous analysis of H_2, O_2, N_2, CO, CO_2, H_2O and N_2O by a thermal conductivity detector (TCD). To avoid condensation of water, formed by the catalytic reaction of H_2, the tubing between the microreactor and the GC was kept at 100 °C, whereas the capillary of the GC itself was kept at 90 °C.

The catalysts used were 2.0 nm Au particles supported on TiO_2 (AURO*lite*™, supported by AuTEK [34]), 3.3 nm Au particles supported on TiO_2 powder (reference catalyst, supplied by the World Gold Council [35]), and 5.0 nm Au particles on TiO_2, which we shall denote as Catalysts A, B, and C, respectively. Catalysts A and B were both supported on TiO_2 P25, as stated by the suppliers.

However, Catalyst C was prepared by deposition–precipitation of unconjugated gold colloids (Ted Pella, Inc.) on anatase TiO_2 powder (Millennium Inorganic Chemicals) with an average BET area of 150–300, according to the supplier. For ease of comparison, the gold concentration of the in-house catalysts was carefully adjusted to those of the commercially available samples. The preparation was performed below 50 °C to evaporate the solvent. After the catalyst had been dried, it was calcined at 200 °C.

2.2. Catalytic reactions

We studied two different reactions on the three different gold catalysts listed above, using the two different oxidizing agents O_2 (3.5N) and N_2O (2.5N). The overall reactions and heats of formation ΔH^0 [36] are then

$$CO + N_2O \rightarrow CO_2 + N_2, \quad \Delta H^0 \approx -200.9 \text{ kJ mol}^{-1}, \tag{R1}$$

$$CO + \tfrac{1}{2}O_2 \rightarrow CO_2, \quad \Delta H^0 \approx -283.0 \text{ kJ mol}^{-1}, \tag{R2}$$

$$H_2 + N_2O \rightarrow H_2O + N_2, \quad \Delta H^0 \approx -159.8 \text{ kJ mol}^{-1}, \tag{R3}$$

$$H_2 + \tfrac{1}{2}O_2 \rightarrow H_2O, \quad \Delta H^0 \approx -241.8 \text{ kJ mol}^{-1}. \tag{R4}$$

Due to the high sensitivity of the GC to H_2, the reactants in (R4) and (R3) were diluted with 50% argon with the total flow kept constant at 1.00 ml min^{-1} for all reactions.

To minimize the contribution of self-heating of the catalyst during an exothermic reaction, all experiments were performed with a maximum of 10% conversion, except for CO oxidation where 15% was achieved at 60 °C on Catalyst A and more than 40% at 80 °C on Catalyst B. The greatest amount of heat liberated during the reactions was 26.0 mW.

To ensure reproducibility, we followed the following scheme for all measurements. First, all catalysts were activated. Catalysts B and C, containing the larger particles, were pretreated over 20 h at 80 °C to ensure steady-state activity measurements. On the other hand, due to its high activity and the possibility of sintering, Catalyst A was pretreated for 20 h at 50 °C. These pretreatments were done under stoichiometrically supplied CO and O_2, for the reaction $CO + \frac{1}{2}O_2 \rightarrow CO_2$, and a total gas flow of 1.00 ml min^{-1}. The CO conversion decreased by 33%, 17%, and 5% before stabilizing for the powder Catalysts A, B, and C, respectively. Temperature programmed activity measurements were then performed in the following sequence of reactions for each catalyst: (R2), (R1), (R3), (R4), (R2), (R1).

Since the maximum temperature reached under these reactions (120 °C on Catalyst B and 160 °C on Catalyst C) was higher than the temperature of the pretreatment (80 °C), the last two steps (remeasurement of (R2) and (R1)) were performed to ensure that the catalysts had not changed during the preceding reactions. Furthermore, to exclude any influence of the applied gases (by e.g. catalyst reduction), the reaction sequence was also conducted in reversed order—starting with (R2)—on a fresh and deactivated catalyst from the same batch. Hereby, the rate differed for each of the reactions (R1)–(R4) studied, but the proportions between (R2) and (R1), and between (R4) and (R3) were similar.

2.3. Particle analysis

Transmission electron microscopy (TEM) was used to study changes in size of the gold particles. For each catalyst, specimens were taken as the catalysts were supplied, after the pretreatment and after measurements of all four catalytic reactions. The specimens were then prepared on a carbon TEM grid by dropping a suspension of catalyst in ethanol on the grid. These were analyzed using a JEOL 3000F field emission electron microscope, which was operated at 300 kV with a LaB_6 filament as an electron source.

2.4. Theoretical methodology

All theoretical results have been obtained using the DFT code DACAPO [37]. The Kohn–Sham one-electron valence states were expanded in a plane wave basis set with a 340 eV (25 Ry) kinetic

Table 1
Activation barriers E_a and adsorption energies E_{ads} in kJ mol^{-1} for CO and H_2 oxidation by N_2O and O_2.

E (kJ mol^{-1})	Au{532} surface	Au_{12} cluster
$E_{ads}[O_2]$	−27.0	−60.8[a]
$E_{ads}[CO]$	−74.3	−91.7[a]
$E_{ads}[N_2O]$	−7.7[b]	−7.7[b]
$E_a[CO + O_2 \rightarrow CO_2 + O]$	–	27.0[a]
$E_a[CO + O \rightarrow CO_2]$	27.0	–

[a] Ref. [30].
[b] Ref. [43].

energy cutoff, and a density cutoff of 680 eV (50 Ry). The core electrons were described by Vanderbilt type ultrasoft pseudopotentials [38]. The exchange-correlation potential was described using the RPBE generalized gradient approximation self-consistently [39]. For the Au{532} surface, a $4 \times 4 \times 1$ Monkhorst–Pack **k**-point sampling was applied in the irreducible Brillouin zone. The surface was modeled by a 1×1-{532} unit cell containing 24 Au atoms with periodic boundary conditions, which corresponds to three close-packed layers. The top most layer and the adsorbents were allowed to fully relax. The O_2 adsorption energy was calculated relative to the experimentally obtained formation energy of H_2O from O_2 and H_2 [40]. This avoids difficulties associated with a DFT treatment of the O_2 triplet state in the gas phase [41].

Thermodynamic analysis was carried out using the total energies obtained from the DFT calculations. It is then possible to obtain free energies by augmenting the DFT total energies with the thermodynamics of a classical ideal gas [42]. For a gas-phase species X at temperature T and pressure p, the Gibbs free energy $G_X(p, T)$ is given by

$$G_X(p, T) = E_X + E_{ZPE} + \Delta H(T) - TS(T) + RT \ln(p/p_0), \tag{1}$$

where E_{ZPE} is the zero point energy, $\Delta H(T)$ denotes the enthalpy change due to raising the temperature from 0 K to T, $S(T)$ is the entropy at T, R is the universal gas constant, and p_0 denotes the standard pressure (taken to be 1 bar).

The potential energy of an adsorbed species X*, E_X, is given by $E_{*/X^*} - E_*$, where E_* is the energy of the clean surface and E_{*/X^*} is the energy of the adsorbate and the surface system. In order to calculate the free energy of this species, we neglect the pressure term, so that the enthalpy change is replaced by the change in internal energy. This leads to the following expression for the free energy $G_X(p, T)$:

$$G_X(p, T) = E_{X^*} + E_{ZPE} + \Delta U(T) - TS(T). \tag{2}$$

The forward rate constant for a reaction i may then be expressed in terms of the Gibb's free energies as $k_i = \nu_i \exp[-\Delta G/RT]$, where $\Delta G = \sum_{X\in\mathcal{P}} G_X - \sum_{X\in\mathcal{R}} G_X$ is the difference of the total Gibb's free energy of the products $\mathcal{P}$ and reactants $\mathcal{R}$ for reaction i, and R is the universal gas constant. The pre-exponential factor in units of s^{-1} is $\nu_i \equiv k_B T/h$, where k_B is Boltzmann's constant.

The DFT energies for the adsorbed species E_{X^*} as well as the activation barriers are given in Table 1. For the N_2O adsorption energy, we have used the experimental value given in Ref. [43].

2.5. Microkinetic model

Using the notation of Ref. [44], we may express any heterogeneous catalysis reaction in the form

$$R(g) \xrightarrow{*} P(g), \tag{R5}$$

where R(g) denotes the gas phase reactants, "*" the active sites on the catalyst, and P(g) the products in the gas phase. If we assume a Langmuir–Hinshelwood mechanism for the reaction kinetics, we may write the elementary steps in the form

$$X(g) + * \rightleftarrows X^*, \quad \forall X \in \mathcal{R}, \tag{R5a}$$

$$R^* \xrightarrow{rds} P(g) + *. \tag{R5b}$$

The turnover frequency for the rate determining step (rds) is then

$$f_{rds} \approx k^+_{rds} \prod_{X\in\mathcal{R}} \Theta_{X^*}, \tag{3}$$

where Θ_{X^*} is the fractional coverage of species X on site "*", and k^+_{rds} is the rate constant for the forward rate, which we assume dominates the total reaction rate.

Assuming the difference in zero point energies of the products and the reactants ΔE_{ZPE} is much smaller than the activation barrier E_a[rds], and the entropy of the adsorbed species is much smaller than that of the species in gas phase, $S_{X^*} \ll S_{X(g)}$, we may express the forward rate constant for the rds as

$$k^+_{rds} \approx \frac{k_B T}{h} \exp\left[-\frac{E_a[\text{rds}] - T\sum_{X\in\mathcal{P}} S_{X(g)}}{RT}\right]. \tag{4}$$

Since the adsorption steps are assumed to occur in equilibrium, the net rate

$$r_{X^*} = k^+_{X^*} p_X \Theta_* - k^-_{X^*} \Theta_{X^*} = 0, \tag{5}$$

so that

$$\Theta_{X^*} = \frac{k^+_{X^*}}{k^-_{X^*}} p_X \Theta_* = K_{X^*} p_X \Theta_*, \tag{6}$$

where p_X is the gas phase pressure of species X, while K_{X^*} is the ratio of the forward to backward rate constants. This may be expressed explicitly in terms of the adsorption energy E_{ads}[X] and gas phase entropy $S_{X(g)}$ of species X as

$$K_{X^*} \approx \exp\left[-\frac{E_{ads}[X] + TS_{X(g)}}{RT}\right], \tag{7}$$

where we again assume $S_{X^*} \ll S_X$ and ΔE_{ZPE} is much smaller than the adsorption energy of species X.

3. Results

3.1. Preliminary investigations

We shall first focus on the thermodynamically unstable N_2O, when it is applied to the catalyst and to the bare support material only. At temperatures below 160 °C no dissociation of N_2O could be measured on either Catalyst B, Catalyst C or bare TiO_2 (Degussa P25). However, in the presence of a reducing agent, e.g. H_2 or CO, N_2O could be reduced over the catalysts, but not over the bare support material [31].

Additionally, CO and O_2 were applied to bare TiO_2 in a stoichiometric ratio of 2:1 to check whether (R2) proceeds on the bare support. This was not the case.

3.2. TEM investigation on changes in particle size

Prior to discussing individual reactions, we will first analyze TEM images of the catalysts (cf. Fig. 2) to evaluate the influence of pretreatment and catalytic reactions on the gold particles. Numerical values for the change in particle size of each catalyst are summarized in Table 2.

The TEM images in Fig. 2a show typical images of Catalyst A from its state as supplied (i), its state after the pretreatment (ii)

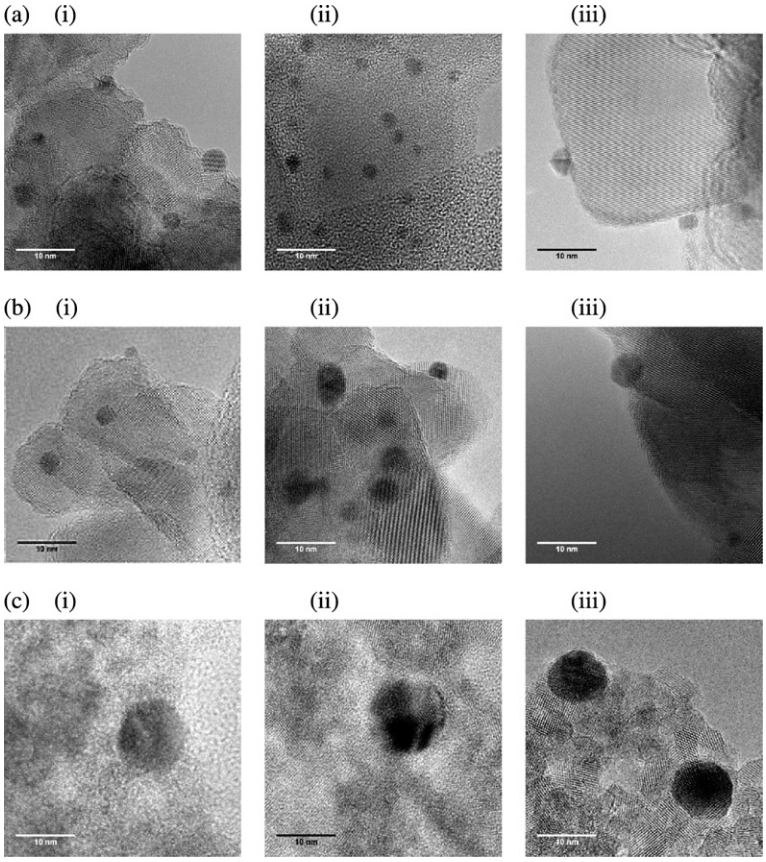

Fig. 2. Bright field TEM images of TiO_2 supported gold particles of Catalyst A (a), Catalyst B (b) and Catalyst C (c), as they were supplied/prepared (i), after the pretreatment (ii) and after catalytic reactions (iii). A summary of the change in particle size may be found in Table 2. The scale bars correspond to 10 nm in each image.

Table 2
Average TiO_2 supported gold particle size d in nm, as determined by TEM, before and after performing oxidation reactions.

d_{Au} (nm)	Gold concentration	Total gold loading	As supplied† or prepared‡	Before reaction	After reaction
Catalyst A	1.02 wt%	62.22 μg	$2.3 \pm 0.6^{\dagger}$	2.6 ± 0.6	3.6 ± 0.8
Catalyst B	1.56 wt%	63.96 μg	$3.4 \pm 0.8^{\dagger}$	3.8 ± 1.1	5.7 ± 3.4
Catalyst C	1.60 wt%	54.00 μg	$13.3 \pm 6.5^{\ddagger}$	16.2 ± 6.6	16.2 ± 6.6

and its state after catalytic reactions (iii). The particles may potentially sinter during storage. However, this was not the case, since the average of the particle size in (a) (2.3 ± 0.6 nm), based on TEM images of 97 particles, is consistent with that stated by the supplier (2.0 nm). The particles appear predominately in a truncated cuboctahedron shape. Following the pretreatment, the average particle size was determined to be 2.6 ± 0.6 nm. The particles themselves were still well dispersed on the support, as can be seen in Fig. 2a(ii). Following the catalytic reactions, the gold particles were sintered to 3.6 ± 0.8 nm.

The size of the gold particles from Catalyst B stated by the supplier (3.3 nm), was also confirmed, as may be seen in Fig. 2b(i). Fig. 2b(ii) shows the particles observed after pretreatment, which were only slightly larger. However, after reactions the gold particles' size increased significantly, cf. Fig. 2b(iii).

Fig. 2c shows Catalyst C, which was formed in-house. Already during preparation, the gold particles sintered from 5.0 nm, as supplied in solution, to 13.3 ± 6.5 nm and formed truncated cuboctahedrons. The pretreatment led to further sintering, with the average particle size becoming 16.2 ± 6.6 nm. This catalyst did not show any further changes in size after catalytic reactions.

Table 3
Apparent activation energies in kJ mol^{-1} for CO and H_2 oxidation by O_2 and N_2O, with an uncertainty of ± 2 kJ mol^{-1}.

E_a (kJ mol^{-1})	Catalyst A	Catalyst B	Catalyst C
$CO + \frac{1}{2}O_2$	36 (36.4)	38	60
$CO + N_2O$	37 (37.5)	40	60
$H_2 + \frac{1}{2}O_2$	38	38	61
$H_2 + N_2O$	39	40	60

Note. Theoretical values obtained using the microkinetic model in the low temperature regime are also provided in parentheses for Catalyst A.

3.3. Steady-state activity measurements

Fig. 3a shows Arrhenius plots for (R1)–(R4) on Catalyst A. Surprisingly, the activation energies obtained were all approximately 37 kJ mol^{-1}, as may be seen from the parallel linear fits. Table 3 summarizes these and the following activation energies. However, for CO oxidation the reaction rate differs by a factor of 2.7, when comparing the different oxidation agents with each other. For H_2 oxidation, the catalyst behaves similarly. The linear fits run parallel and the reaction rate differs by 3.2. On the Au particles of Catalyst B, which were sintered to 5.7 nm, the trend depicted on Catalyst A continues, but is even more distinct, as shown in Fig. 3b. There is approximately one order of magnitude between the rates of CO oxidation and for H_2 oxidation, using N_2O and O_2, respectively.

For CO oxidation by O_2 on Catalyst B, the reaction rate was found to reach a maximum at about 80 °C, cf. Fig. 3b. One reason for this may be that the catalyst was operated under mass-transport controlled conditions, e.g. when too little active material has been used. On the other hand, this may also be due to CO or O_2 desorption. Despite this, the parallel running fits of the

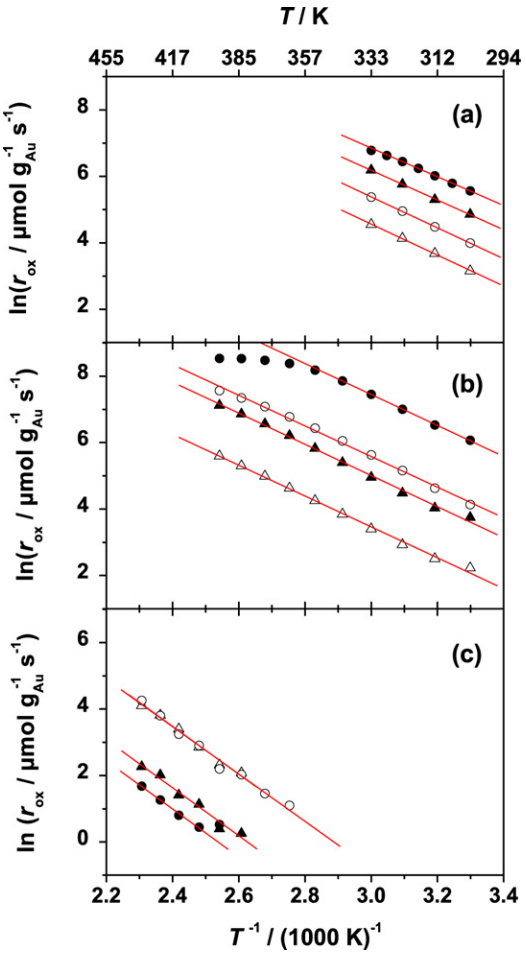

Fig. 3. Arrhenius plots of the activation energies for the four reactions on TiO_2 supported gold particles of Catalyst A (a), Catalyst B (b) and Catalyst C (c): $CO + \frac{1}{2}O_2$ (●), $CO + N_2O$ (▲), $H_2 + \frac{1}{2}O_2$ (○) and $H_2 + N_2O$ (△). An overview of the activation energies is given in Table 3.

Arrhenius plots again indicate similar activation energies around 39 kJ mol^{-1}, as shown in Table 3. These two catalysts where active even at room temperature, although O_2 was a significantly better oxidizing agent. For (R1), N_2 released from N_2O could be balanced with the CO_2 formed, indicating that the CO_2 does not originate from other sources.

Fig. 3c shows Arrhenius plots for Catalyst C and demonstrates that on this catalyst N_2O is the better oxidizing agent for CO, whereas no difference in rate could be found for H_2 oxidation. A very similar apparent activation energy of about 60 kJ mol^{-1} was again found for all the four studied reactions. On these large particles an onset of conversion could not be observed below 80 °C.

3.4. Theoretical results

It has recently been shown that for small Au nanoparticles ($d \lesssim 5$ nm) at 273 K, experimentally obtained CO oxidation rates follow a d^{-3} relationship, independent of the support material used [6,11,19]. This strongly suggests that corner sites are the active sites on small gold nanoparticles, in agreement with recent DFT studies [11,18]. By extrapolating the linear fit of our CO oxidation rate measurements for Catalyst A to 273 K, cf. Fig. 3a, we find an estimated reaction rate of approximately 66 µmol g^{-1} s^{-1} for $d \approx 3.6$ nm. This agrees well with the d^{-3} relationship of Nørskov et al. [6], where a fit to data from over 60 different sources on five different supports is presented. This is not altogether surprising, since this fit was generated by assuming the gold nanoparticle

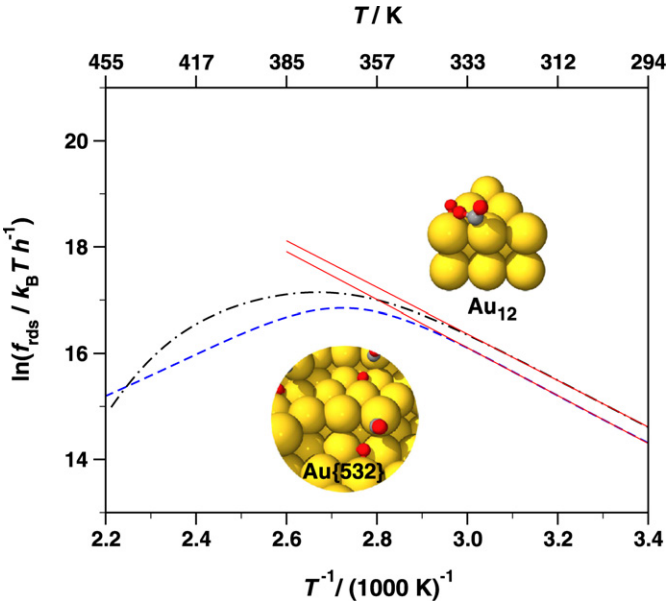

Fig. 4. Arrhenius plot of the rds turnover frequency f_{rds} in $k_BT/h \approx 10^{13}$ s^{-1} for CO oxidation by N_2O on Au{532} (blue dashed line) and by O_2 on a Au_{12} cluster (black dash-dotted line) as obtained from the microkinetic model using the DFT transition state structures depicted above [30]. The apparent activation barriers (red solid lines) in the low temperature regime ($T < 350$ K) are shown for ease of comparison with Fig. 3, and listed in Table 1.

shape is the top half of a regular cuboctahedron, as is the case for our catalysts cf. Fig. 2.

On the other hand, the reactivity of the Au–TiO_2 interface introduces a d^{-2} correction term to the reaction rate, which becomes important for larger gold nanoparticles similar to Catalyst C. However, due to the computational complexity of properly treating the Au–TiO_2 interface for large nanoparticles, we shall restrict consideration to reactions which occur on the corner sites of the Au particles.

We begin by first considering CO oxidation using N_2O. It has been generally accepted that the reaction kinetics for CO oxidation over a metal surface follow the Langmuir–Hinshelwood mechanism. According to this, the elementary steps of adsorption and desorption are in equilibrium, and (R1) may be written in terms of the following elementary steps:

$$CO(g) + {}^{*} \rightleftarrows CO^{*}, \tag{R1a}$$

$$N_2O(g) + {}^{\diamond} \rightleftarrows N_2O^{\diamond}, \tag{R1b}$$

$$CO^{*} + N_2O^{\diamond} \xrightarrow{\text{rds}} CO_2(g) + N_2(g) + {}^{*} + {}^{\diamond}. \tag{R1c}$$

Here we have assumed that CO and N_2O adsorb on different corner sites, denoted by "*" and "◇" respectively. This is clearly the case for CO oxidation, as may be seen from the transition states depicted in the insets of Fig. 4.

Since we found N_2O does not dissociate spontaneously on gold, as has also been reported by Gluhoi et al. [31], we assume this reaction requires adsorbed CO* as a reducing agent. However, the overall barrier for (R1c) should still be the same as for CO oxidation with atomic O. On the other hand, the desorption of both N_2 and CO_2 should occur spontaneously.

To model the corner sites of a gold nanoparticle for reaction (R1c), we have chosen a Au{532} surface, which consists of both B5 and kink sites. This allows atomic O to adsorb on the preferred B5 sites while CO adsorbs on the kink sites. This is depicted in the Au{532} transition state for (R1c), shown in the lower inset of Fig. 4. Since the Au_{12} cluster model of a corner site [30] does not include B5 sites for atomic O adsorption, it yields an activation

barrier for (R1c) twice that found for the Au{532} surface. For this reason, the Au_{12} model should not be used to model (R1c).

Employing the microkinetic model described above, the turnover frequency for the rate determining step (rds) f_{rds} in s^{-1}, may then be approximated by

$$f_{rds} \approx \frac{k_B T}{h} \frac{K_{CO^*} K_{N_2O^\circledast} p_{CO} p_{N_2O}}{(1 + K_{CO^*} p_{CO})(1 + K_{N_2O^\circledast} p_{N_2O})} \times \exp\left[-\frac{E_a[\text{rds}] - T(S_{CO_2(g)} + S_{N_2(g)})}{RT} \right], \quad (8)$$

where K_{CO^*} and $K_{N_2O^\circledast}$ are given in (7). The required activation and adsorption energies for the Au{532} surface are provided in Table 1 and the temperature dependent gas phase entropies are interpolated using data from Ref. [36].

Fig. 4 shows the temperature dependence of the turnover frequency f_{rds}, for the rds of CO oxidation by N_2O on Au{532}. We found f_{rds} follows an Arrhenius-like behavior in the low temperature regime ($T < 350$ K). However, at higher temperatures the turnover frequency decreases with increasing temperature, with an apex at $T \approx 360$ K.

When using O_2 instead of N_2O to oxidize CO, we may again assume a Langmuir–Hinshelwood mechanism, so that the elementary steps for (R2) may be written as

$$CO(g) + {}^* \rightleftarrows CO^*, \quad (R2a)$$

$$O_2(g) + {}^\circledast \rightleftarrows O_2^\circledast, \quad (R2b)$$

$$CO^* + O_2^\circledast \xrightarrow{\text{rds}} CO_2^* + O^\circledast, \quad (R2c)$$

$$CO^* + O^\circledast \Rightarrow CO_2(g) + {}^* + {}^\circledast, \quad (R2d)$$

where "*" and "$^\circledast$" denote active sites for CO and O_2 respectively, on the Au particle.

Since O_2 is known not to dissociate spontaneously on gold nanoparticles [45], we assume CO is oxidized directly by O_2 (R2c), as discussed in Refs. [30,46]. We further assume (R2c) is the rate determining step, so that (R2d) occurs relatively quickly. This is justified in the case of high CO coverages, since CO_2 will quickly desorb from the surface.

To model the gold nanoparticle corner sites for reaction (R2c), we have used the Au_{12} cluster model described in Ref. [30]. As seen in Table 1, such a model yields much higher adsorption energies, particularly for O_2. This is necessary to correctly model (R2c) on gold nanoparticles. As shown in the upper inset of Fig. 4, the transition state for (R2d) on the Au_{12} cluster model has the O_2 molecule strongly adsorbed on the corner site, while CO is adsorbed on the edge.

Again employing our microkinetic model, f_{rds} for (R2) may be approximated by

$$f_{rds} \approx \frac{k_B T}{h} \frac{K_{O_2^\circledast} K_{CO^*} p_{O_2} p_{CO}}{(1 + K_{O_2^\circledast} p_{O_2})(1 + K_{CO^*} p_{CO})} \times \exp\left[-\frac{E_a[\text{rds}] - T S_{CO_2(g)}}{RT} \right], \quad (9)$$

where K_{CO^*} and $K_{O_2^\circledast}$ are given in (7). The necessary activation and adsorption energies for the Au_{12} cluster model are provided in Table 1 and the temperature dependent gas phase entropies are interpolated using data from Ref. [36].

The temperature dependence of f_{rds} for CO oxidation by O_2 on Au_{12} is shown in Fig. 4. We again found f_{rds} has an Arrhenius behavior in the low temperature regime ($T < 350$ K). As with N_2O, we found at higher temperatures the turnover frequency decreases with increasing temperature, with an apex at $T \approx 370$ K.

4. Discussion

Table 3 shows the overall trend in apparent activation energies for the reactions measured on Catalysts A, B and C. First, there is a clear size dependence trend from large gold particles with less reactivity to the significantly more reactive smaller ones for all the reactions studied. Second, there is very little difference in the apparent overall activation barrier for CO or H_2 oxidation, irrespective of the oxidizing agent used. This is seen for both experimental and theoretical apparent activation barriers, which are in quantitative agreement for Catalyst A ($d \lesssim 5$ nm), in the low temperature regime ($T < 350$ K), as shown in Table 3. However, there is little correlation between the experimental reaction rate and theoretical turnover frequency for the larger Catalyst C. This may be expected, as for larger Au nanoparticles ($d \gtrsim 10$ nm), the bulk gold properties may begin to dominate, so that a cluster-based theoretical model is no longer applicable.

Clearly it would be desirable to get a direct comparison between measured rates and calculated turnover frequencies. However, such a comparison requires atomic resolution characterization of the particles in question. Given the large dispersity in particle size for our catalysts we are unable to provide such experimental detail. However, it should be born in mind that the trends for the theoretical turnover frequency should match those of the experimental rate, as shown in Table 3.

We shall first focus on CO oxidation using N_2O according to (R1). From the preliminary investigations it may be concluded that in the absence of a reducing agent, the dissociation of N_2O is inhibited. This may be accounted for by the very weak Au–N_2O bond which leads to rapid desorption of N_2O [31]. However, this reaction changes the overall entropy of the system only slightly, since one diatomic and one triatomic species both adsorb and desorb from the surface in (R1). This means that although there is only a small N_2O coverage, for high CO coverage experiments the reaction rate should be significant. On the other hand, as seen in Fig. 4, at higher temperatures ($T > 350$ K) CO begins to desorb from the surface and the turnover frequency begins to decrease at higher temperatures ($T > 360$ K). We were unable to verify this experimentally since we found gold particle sintering began to occur in this temperature range, as shall be discussed later.

For the case of CO oxidation by O_2 according to (R2), there is a significant loss of entropy in the overall reaction, as three diatomic species adsorb, but two triatomic species desorb. Thus a high O_2 adsorption energy is required for the reaction rate to be significant. As this is the case for small gold nanoparticles and the Au_{12} cluster model for a corner site, we employ this model for (R2). Even so, we find at higher temperatures ($T > 370$ K) the reaction rate decreases significantly as both O_2 and CO begin to desorb from the gold nanoparticle. This may be seen in the reaction rate plots for CO oxidation by O_2 on Catalyst B, shown in Fig. 3. Here, the reaction rate begins to flatten at about 370 K, in agreement with the theoretical turnover frequency shown in Fig. 4.

Besides the activity, stability is the next most important property of an industrial catalyst. With a view on the gold loading of the catalysts used, noted in Table 2, it seems clear that small particles with a high loading are more likely to sinter than with lower loadings. One reason for this is that due to the low melting point of gold [47,48] or quasi-melting [49], gold particles already become mobile at only slightly elevated temperatures. The larger the particles at a constant loading are, the fewer particles are on the support, and the larger is the distance to their nearest neighbor.

Fig. 2 illustrates the sintering for different gold particle sizes during the pretreatment, when comparing image (i) with image (ii), as well as during the activity measurements. Since the activity measurements were performed in a sequence (as described above),

the change in particle size may be related to 40 °C more in heat applied than for the catalytic reactions driven on Catalyst B.

Catalyst A was not heated more than the pretreatment required. This means that the sintering on this catalyst is related only to how the reactions proceeded. Across the general observations published regarding CO oxidation on TiO_2 supported gold using O_2 as an oxidizing agent, sintering of nanoparticulate gold has not been reported. Gold nanoparticles have also been found to be a stable catalyst in the presence of H_2 and H_2O [50]. This suggests that the sintering observed on Catalyst A is related to the supply of N_2O. In contrast, the particles of Catalyst C did not significantly sinter, even though the maximum temperature was 80 °C higher than the temperature of the pretreatment.

5. Conclusions

We have investigated two different reactions on three TiO_2 supported gold catalysts with two different oxidizing agents. Experimental results for CO oxidation on Catalysts A and B agree with both our theoretical model and the literature, following the d^{-3} trend advocated by Nørskov et al. [6]. However, for Catalyst C we found more bulk-like behavior.

Based on our theoretical model, we find oxidizing CO by N_2O involves a CO–O transition state, with atomic O adsorbed on the gold B5 sites and CO on the corners. On the other hand, CO oxidation by molecular O_2 occurs via a different reaction pathway, which instead involves a meta-stable intermediate CO–O_2. In this case, O_2 is strongly adsorbed on gold corner sites while CO is adsorbed on the nearby edge sites (cf. Fig. 2).

However, although the two oxidizing agents used proceeded via *different* reaction pathways on *different* active sites, the apparent overall activation barriers obtained from both theory and experiment were found to be the *same*. From experiment, we found that H_2 and CO oxidation proceed similarly, with common activation barriers and rate enhancements when comparing oxidizing agents.

Additionally, from our TEM analysis we conclude that N_2O oxidation may promote sintering of Au nanoparticles on TiO_2, since significant sintering has not been found for CO and H_2 oxidation on gold nanoparticles using O_2 [27,50].

Acknowledgments

The authors gratefully acknowledge support in the form of catalysts provided by Project AuTEK. We also thank F.B. Grumsen for assistance with taking TEM images, and T. Bligaard for useful discussions. G. Walther and D.J. Mowbray also acknowledge financial support from NABIIT. The Center for Atomic-scale Materials Design is funded by the Lundbeck Foundation. The authors also acknowledge support from the Danish Center for Scientific Computing through grant HDW-1103-06.

References

[1] B. Hammer, J.K. Nørskov, Nature 376 (1995) 238–240.
[2] M. Haruta, T. Kobayashi, H. Sano, N. Yamada, Chem. Lett. (1987) 405–408.
[3] A.S.K. Hashmi, G.J. Hutchings, Angew. Chem. 45 (2006) 7896.
[4] G.C. Bond, D.T. Thompson, Catal. Rev. Sci. Eng. 41 (1999) 319–388.
[5] G.C. Bond, C. Louis, D.T. Thompson, Catalysis by Gold, first ed., Imperial College Press, London, 2006.
[6] B. Hvolbæk, T.V.W. Janssens, B.S. Clausen, H. Falsig, C.H. Christensen, J.K. Nørskov, Nano Today 2 (2007) 14–18.
[7] D.E. Starr, S.K. Shaikhutdinov, H.-J. Freund, Top. Catal. 36 (2005) 33–41.
[8] H.-J. Freund, Catal. Today 117 (2006) 6–17.
[9] M. Valden, X. Lai, D.W. Goodman, Science 281 (1998) 1647–1649.
[10] M.S. Chen, D.W. Goodman, Science 306 (2004) 252–255.
[11] T.V.W. Janssens, A. Carlsson, A. Puig-Molina, B.S. Clausen, J. Catal. 240 (2006) 108–113.
[12] C. Xu, J. Su, X. Xu, P. Liu, H. Zhao, F. Tian, Y. Ding, J. Am. Chem. Soc. 129 (2007) 42–43.
[13] C. Xu, X. Xu, J. Su, Y. Ding, J. Catal. 252 (2007) 243–248.
[14] R.J.H. Grisel, B.E. Nieuwenhuys, Catal. Today 64 (2001) 69–81.
[15] M. Mavrikakis, P. Stoltze, J.K. Nørskov, Catal. Lett. 64 (2000) 101–106.
[16] Z.-P. Liu, P. Hu, A. Alavi, J. Am. Chem. Soc. 124 (2002) 14770–14779.
[17] N. Lopez, J.K. Nørskov, J. Am. Chem. Soc. 124 (2002) 11262–11263.
[18] N. Lopez, T.V.W. Janssens, B.S. Clausen, Y. Xu, M. Mavrikakis, T. Bligaard, J.K. Nørskov, J. Catal. 223 (2004) 232–235.
[19] T.V.W. Janssens, B.S. Clausen, B. Hvolbæk, H. Falsig, C.H. Christensen, T. Bligaard, J.K. Nørskov, Top. Catal. 44 (2007) 15–26.
[20] B.E. Solsona, T. Garcia, C. Jones, S.H. Taylor, A.F. Carley, G.J. Hutchings, Appl. Catal. A Gen. 312 (2006) 67–76.
[21] D.T. Thompson, Top. Catal. 38 (2006) 231–240.
[22] R.D. Waters, J.J. Weimer, J.E. Smith, Catal. Lett. 30 (1994) 181–188.
[23] S. Ivanova, C. Petit, V. Pitchon, Appl. Catal. A Gen. 267 (2004) 191–201.
[24] S. Ivanova, C. Petit, V. Pitchon, Gold Bull. 39 (2006) 3–8.
[25] C.H. Christensen, B. Jorgensen, J. Rass-Hansen, K. Egeblad, R. Madsen, S.K. Klitgaard, S.M. Hansen, M.R. Hansen, H.C. Andersen, A. Riisager, Angew. Chem. 45 (2006) 4648–4651.
[26] M.-C. Daniel, D. Astruc, Chem. Rev. 104 (2004) 293–346.
[27] G. Walther, G. Jones, S. Jensen, U.J. Quaade, S. Horch, Catal. Today, in press.
[28] M. Haruta, Catal. Today 36 (1997) 153–166.
[29] J.A. van Bokhoven, C. Louis, J.T. Miller, M. Tromp, O.V. Safonova, P. Glatzel, Angew. Chem. Ger. Ed. 118 (2006) 4767–4770.
[30] H. Falsig, B. Hvolbæk, I.S. Kristensen, T. Jiang, T. Bligaard, C.H. Christensen, J.K. Nørskov, Angew. Chem. 47 (2008) 4835–4839.
[31] A.C. Gluhoi, M.A.P. Dekkers, B.E. Nieuwenhuys, J. Catal. 219 (2003) 197–205.
[32] L.M. Molina, B. Hammer, Phys. Rev. B 69 (2004) 155424.
[33] U.J. Quaade, S. Jensen, O. Hansen, J. Appl. Phys. 97 (2005) 44906.
[34] http://www.mintek.co.za.
[35] http://www.gold.org.
[36] D.R. Lide, Handbook of Chemistry and Physics, 87th ed., CRC Press, Boca Raton, 2006–2007.
[37] http://wiki.fysik.dtu.dk/dacapo.
[38] D. Vanderbilt, Phys. Rev. B 41 (1990) 7892–7895.
[39] B. Hammer, L.B. Hansen, J.K. Nørskov, Phys. Rev. B 59 (1999) 7413–7421.
[40] J.K. Nørskov, J. Rossmeisl, A. Logadottir, L. Lindqvist, J.R. Kitchin, T. Bligaard, H. Jonsson, J. Phys. Chem. B 108 (2004) 17886–17892.
[41] S. Kurth, J.P. Perdew, P. Blaha, Int. J. Quant. Chem. 75 (1999) 889–909.
[42] J.H. Noggle, Physical Chemistry, third ed., Harper Collins, New York, 1996.
[43] B.E. Nieuwenhuys, A.C. Gluhoi, E.D.L. Rienks, C.J. Weststrate, C.P. Vinod, Catal. Today 100 (2005) 49–54.
[44] M. Boudart, G. Djéga-Mariadassou, Kinetics of Heterogeneous Catalytic Reactions, Princeton University Press, Princeton, NJ, 1984.
[45] J.K. Nørskov, T. Bligaard, A. Logadottir, S. Bahn, L.B. Hansen, M. Bollinger, H. Bengaard, B. Hammer, Z. Sljivancanin, M. Mavrikakis, Y. Xu, S. Dahl, C.J.H. Jacobsen, J. Catal. 209 (2002) 275–278.
[46] L.M. Molina, B. Hammer, Appl. Catal. A Gen. 291 (2005) 21–31.
[47] P. Buffat, J.P. Borel, Phys. Rev. A 13 (1976) 2287–2298.
[48] H. Sykes, E. Charles, F.J. Williams, M.S. Tikhov, R.M. Lambert, J. Phys. Chem. B 106 (2002) 5390–5394.
[49] P.M. Ajayan, D.L. Marks, Phys. Rev. Lett. 60 (1988) 585–587.
[50] P. Landon, J. Ferguson, B.E. Solsona, T. Garcia, S. Al-Sayari, A.F. Carley, A.A. Herzing, C.J. Kiely, M. Makkee, J.A. Moulijn, A. Overweg, S.E. Golunski, G.J. Hutchings, J. Mater. Chem. 16 (2006) 199–208.

Trends in CO Oxidation Rates for Metal Nanoparticles and Close-Packed, Stepped, and Kinked Surfaces

T. Jiang, D. J. Mowbray, S. Dobrin, H. Falsig, B. Hvolbæk, T. Bligaard, and J. K. Nørskov*

Center for Atomic-Scale Materials Design, Department of Physics, Technical University of Denmark, DK-2800 Kgs. Lyngby, Denmark

Received: December 18, 2008; Revised Manuscript Received: April 15, 2009

Using density functional theory calculations, we study trends in the CO oxidation activity for different metals and surfaces. Specifically, we show how the activity of (111) close-packed surfaces, (211) stepped surfaces, (532) kinked surfaces, 55 atom cuboctahedral clusters, and 12 atom cluster models changes with the coordination number of atoms at the active sites. This effect is shown to be electronic in nature, as low coordinated metal atoms, which bind reactants most strongly, have the highest energy metal d states.

Introduction

The CO oxidation reaction, $CO + {}^1/_2O_2 \rightarrow CO_2$, often serves as a prototypical reaction in heterogeneous catalysis. Its importance is exemplified by its use to remove toxic CO from the exhaust of motor vehicles, where Pt, Pd, and Rh are the catalysts of choice.[1,2] Yet the reaction is relatively simple, with only two reactants and one product. For these reasons it is very well studied, both experimentally[3–13] and theoretically.[14–18] The CO oxidation reaction has also served as a test reaction in the recent exploration of the catalytic activity of nanoparticle Au.[8,9,18–31] Interestingly, small Au nanoparticles ($d \lesssim 5$ nm) were found to be catalytically active, whereas larger Au particles and close-packed extended surfaces are much less so. This has been variously attributed to quantum size effects,[8] support interactions,[22,23,32] charge transfer,[24,25,33] and the role of low-coordinated sites.[14,17,26–30,34]

Unlike most previous studies of the CO oxidation reaction, we will concentrate in the present paper on the broad trends in reactivity. We will use density functional theory (DFT) calculations to describe the variation of bond energies and activation energies with metal and surface structures. As we are interested in broader trends, we have chosen not to consider coverage dependence or surface oxidation at certain conditions.[1] Instead, we will compare metals under idealized conditions where the surface coverages are optimal. While these conditions may not be realizable in practice, the present work may be viewed as a comparison of the intrinsic catalytic activity of different metals (in their metallic states) and different surface structures.

We begin with a short description of the structure models and calculation method used. This is followed by an introduction to the microkinetic model and Sabatier analysis used to compare reaction rates for different metals. We will show that to a first approximation the rate is a volcano-shaped function of the adsorption energy of O and CO. In so doing, we extend and elaborate on the work started in ref 35. By calculating the volcano function for various stepped and kinked surfaces as well as for nanoparticles, we show that the peak location does not depend strongly on the surface geometry. However, the rate itself is strongly dependent on the geometry. This is because the adsorption energies, and hence the activation energies, are geometry dependent. It spite of its simplicity, this analysis yields results in qualitative agreement with available experimental data, including the special catalytic activity of Au nanoparticles. This model also provides a simple picture of geometrical effects in the CO oxidation reaction. Finally, we use these calculations to identify the electronic origin of the structure dependence of the chemical activity.

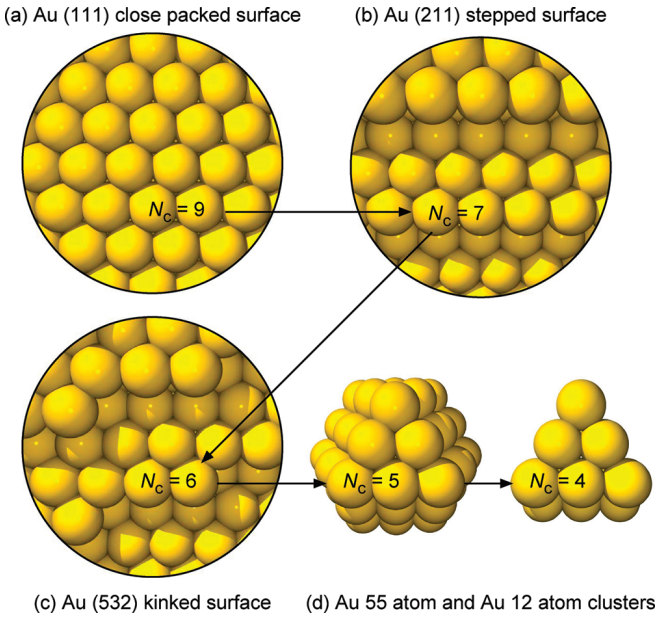

Figure 1. Structural schematics and lowest coordination number N_C for the (a) Au (111) close-packed surface, (b) Au (211) stepped surface, (c) Au (532) kinked surface, and (d) Au 55 atom cuboctahedral cluster and Au 12 atom cluster corner model.

Method

Surface Structures. Surface geometry is known to play an important role in the catalytic properties of metals. Here we compare the catalytic activity of the five different surface structures shown in Figure 1a−d. We begin by studying the activity of a close-packed surface (111), a stepped surface (211), and a surface with both steps and kinks (532). To better describe highly under-coordinated surface structures, we also study a 12 atom cluster chosen to model a sharp corner on a large nanoparticle with the metal atoms kept fixed at the bulk lattice

* To whom correspondence should be addressed. E-mail: norskov@fysik.dtu.dk.

10.1021/jp811185g CCC: $40.75
Published on Web 05/21/2009

constant values (M12). Further, to describe the influence of decreasing size on adsorption energies we have used a "magic size" 55 atom cuboctahedral cluster model. Although not necessarily the most stable structure, cuboctahedral Au and Pt clusters have been found experimentally.[36–38] Also, unlike other cluster types, such as icosahedral, cuboctahedral clusters have a bulk fcc structure. This aids in the comparison of energies and occupation sites with those for bulk surface structures.

Calculation Method. Adsorption, transition state, and gas phase energies are calculated using the plane wave DFT code DACAPO.[39] Kohn−Sham one-electron valence states are expanded in a basis of plane waves with kinetic energies up to 30 Ry. Vanderbilt nonlocal ultrasoft pseudopotentials are used to describe the core electrons. The exchange-correlation (xc)-energy is described employing the RPBE generalized gradient correction self-consistently.[39]

For all surfaces, a $6 \times 6 \times 1$ Monkhorst-Pack **k**-point sampling in the irreducible Brillouin zone was used. The occupation of the one electron states was calculated at a temperature of $k_BT = 0.1$ eV, and all energies were extrapolated to $T = 0$ K. Lattice constants have been determined by separate calculations on the bulk metals. The (111) surfaces were modeled by (2×2) surface unit cells with slab thicknesses of four layers and the two topmost layers were allowed to fully relax. The (211) and (532) surfaces were modeled by (2×1) and (1×1) surface unit cells, respectively, with three close packed layer slabs, where only the topmost layer was allowed to relax. For all types of surfaces, the neighboring slabs are separated by more than 10 Å of vacuum. For both cluster structures, Γ point calculations were performed within unit cells with ≳10 Å of vacuum between structures, with a Fermi temperature of $k_BT = 0.01$ eV. All of the atoms in the 12 atom clusters were kept fixed in order to mimic the geometrically constrained corner of a larger particle, with a lattice constant corresponding to the bulk value. On the other hand, the M55 cluster has a realistic nanoparticle structure,[36–38] so all atomic positions were relaxed.

We have included energy corrections for the adsorption of CO to avoid the overbinding of CO by DFT, which yields lower binding energies on bridge sites than atop sites, in contradiction to experiment.[40] Oxygen adsorption energies are calculated relative to the O_2 energy from H_2O splitting using the experimental reaction energy and that for H_2 and H_2O in the gas phase.[41] This avoids difficulties associated with a DFT treatment of the triplet state of gas phase O_2.[42]

Microkinetic Modeling. In order to link the calculated adsorption energies and activation energies with catalytic activity, we will employ a simplified microkinetic model, built on the analysis presented in ref 35. Such a model, based on adsorption energies and activation barriers for Au corner sites, has recently been shown to quantitatively reproduce the temperature dependent reactivity of Au nanoparticles.[31]

A simplified kinetic treatment, termed the "Sabatier analysis", is used to estimate reaction rates.[43] In this analysis, the coverages of free sites and adsorbed species are assumed optimal for each reaction step. Although this may not be realizable under experimental conditions, the Sabatier rate yields an exact upper bound so long as the state of the surface does not change due to oxidation or reconstruction. The Sabatier analysis thus provides a measure of the intrinsic ability of a metal surface to catalyze a given reaction.

We begin by assuming a Langmuir−Hinshelwood type mechanism for CO oxidation, so that the reaction may be described using the following elementary steps:

$$CO + * \leftrightarrow CO* \quad \text{(R1)}$$

$$O_2 + * \leftrightarrow O_2* \quad \text{(R2)}$$

$$O_2* + * \leftrightarrow 2O* \quad \text{(R3)}$$

$$CO* + O* \leftrightarrow CO_2 + 2* \quad \text{(R4)}$$

$$CO* + O_2* \leftrightarrow CO_2 + O* + * \quad \text{(R5)}$$

Here we have assumed that reactions R1 and R2 have reached equilibrium, so that the net rates $r_1 \approx r_2 \approx 0$. Overall, the Sabatier rate for CO_2 production is the sum of the rates for reactions R4 and R5. However reaction R4 is limited if no atomic oxygen is present from reactions R3 or R5. On the other hand, reaction R5 will be limited by a poisoning by atomic oxygen of the catalyst, and can therefore not be faster than reaction R4. Hence the overall reaction rate according to the Sabatier analysis is then

$$r_S = \max\{2\min\{r_5^+, r_4^+\}, \min\{2r_3^+, r_4^+\}\}$$

since the rates for reactions R3−R5 will be maximized if we consider only the forward rates r_i^+.

Following the procedure outlined in ref 35, the forward rates are given by

$$r_3^+ = \theta_{O_2}\theta_* k_3^+$$
$$r_4^+ = \theta_O\theta_{CO}k_4^+ \approx \theta_{CO}k_4^+$$
$$r_5^+ = \theta_{O_2}\theta_{CO}k_5^+$$

where θ_{CO}, θ_{O_2}, θ_O, and θ_* are the coverages of CO, O_2, O, and unoccupied sites respectively. Note that we have assumed the rate for (R4) is independent of the O coverage, which was shown to give a good approximation to the fully self-consistently solved microkinetic model in ref 35. The rate constant k_i for the elementary reaction step, i, is given by

$$k_i = \nu_i \exp\left[\frac{-\Delta G_{ai}}{k_BT}\right] = \nu_i \exp\left[\frac{-(E_{ai} + \Delta ZPE_{ai} - T\Delta S_{ai})}{k_BT}\right]$$

where ν_i is the prefactor, E_{ai} is the activation barrier for the reaction, ΔZPE_{ai} is the zero-point energy change, ΔS_{ai} is the entropy change, k_B is the Boltzmann constant, and T is the temperature. We assume the prefactors are metal independent, so that $\nu_i = k_BT/h$, and that the change in zero-point energy is negligible compared to the activation barrier ($\Delta ZPE_{ai} \ll E_{ai}$). Further, we assume the entropy of adsorbed species is much smaller than that in the gas phase ($S_{ads} \ll S_{gas}$), so that $\Delta S_{ai} \approx \mp S_{gas}$ for adsorption/desorption, where gas phase entropies are taken from ref 44. Activation barriers are found as the energy difference between the transition and initial state, ($E_a = \max(E_{TS} - E_{IS}, 0)$).

Since reaction steps R1 and R2 are assumed to be in equilibrium, the coverages of CO and O_2 satisfy $\theta_{CO} = K_1 p_{CO}\theta_*$ and $\theta_{O_2} = K_2 p_{O_2}\theta_*$. The coverage of unoccupied adsorption sites

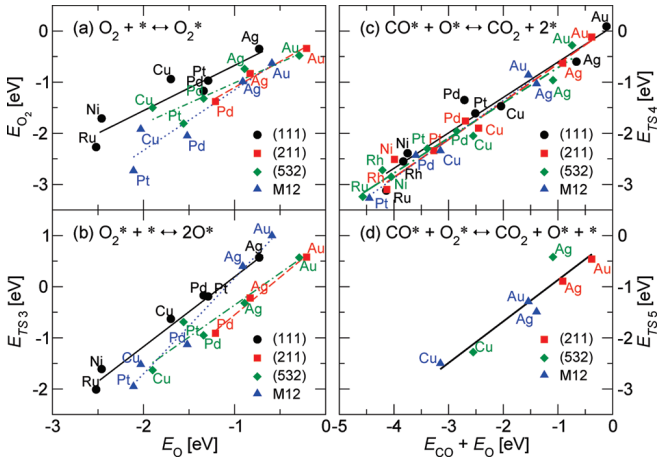

Figure 2. The scaling and BEP relations for (111) surfaces (●, — [black]), (211) surfaces (■, - - - [red]), (532) surfaces (◆, -•- [green]), and M12 clusters (▲, ••• [blue]). (a) The scaling of the O_2 adsorption energy E_{O_2} with the O adsorption energy E_O. (b) Calculated transition state energies for O_2 dissociation E_{TS3} (R3) as a function of O adsorption energy E_O. (c) Calculated transition state energies for adsorbed CO reacting with adsorbed O E_{TS4} (R4) as a function of the sum of the O and CO adsorption energies, $E_O + E_{CO}$. (d) Calculated transition state energies for adsorbed CO reacting with adsorbed O_2 E_{TS5} (R5) as a function of the sum of the O and CO adsorption energies, $E_O + E_{CO}$, with surface averaged BEP relation (—).

is then

$$\theta_*^{\max} \approx \frac{1}{1 + K_1 p_{CO} + K_2 p_{O_2}}$$

where we have assumed $\theta_O \ll \theta_{CO}$, θ_{O_2}, and θ_*, which provides upper bounds for the respective coverages. Here p_{CO} and p_{O_2} are the partial pressures of O_2 and CO in the gas phase, and the equilibrium constants $K_i = k_i^+/k_i^-$ are determined from $K_i = \exp(-(\Delta E_i - TS_i)/(k_B T))$, where ΔE_i is the chemisorption energy of CO, O_2, and O respectively.

Results and Discussion

Scaling Relations. Our goal is to use the calculated adsorption energies and activation energies to study trends in catalytic rates. Therefore we begin by studying trends in these energies. We will show how scaling relations between different adsorption energies and between activation energies and adsorption energies (Brønsted−Evans−Polanyi (BEP) relations) limit the number of independent variables characterizing a particular metal and structure.[45]

In Figure 2a−d, scaling relations obtained for the CO oxidation reaction on the different surface structures of transition and noble metals are shown. In Figure 2a, we present the linear scaling between the adsorption energy of O_2 and atomic oxygen, O. Further, we obtain BEP relations in Figure 2b−d showing a linear scaling between the adsorption energies of CO and O, E_{CO} and E_O, and the transition state energy for reactions R3−R5. In general, the data falls into families of linear relations, with one approximately linear relation for each structure of the catalyst. The differences in the lines reflect the structure-dependence of the different adsorption energies and reaction barriers. For the CO + O and CO + O_2 reactions the different BEP lines are nearly indistinguishable. This implies that geometrical effects may be neglected. Note that even if there is only one BEP line for a particular elementary reaction for all structures, there are still large differences in the adsorption and hence the activation energy for a given metal from one structure to the next. For instance, for Au the CO adsorption energy varies by ≈1.0 eV from the (111) surface to the M12 cluster.

The linear relations shown in Figure 2 mean that of the original six metal-dependent variables (E_{CO}, E_{O_2}, E_O, E_{TS3}, E_{TS4}, and E_{TS5}) only two are independent. We choose for these two independent variables E_{CO} and E_O. We may thus calculate the Sabatier rate for CO oxidation as a function of these two parameters alone for each of the structures studied. This means that we rely on the linear relations in Figure 2 in the kinetics. These relations are not exact, but they clearly describe the trends for metals and structures quite well. We suggest that this provides a good basis for a study of trends in the catalytic activity.

Volcanoes. Figure 3a−d shows the Sabatier activity $A_S = k_B T \ln(r_S/k_B T h^{-1})$ as a function of the adsorption energies of CO and O for the close-packed (111), stepped (211), and step-kinked (532) surfaces as well as for the M12 cluster. A 2D volcano results with a maximum for a particular value of E_{CO} and E_O, which represents the adsorption properties of the best catalyst. Note that the CO adsorption energy on Pd(111) has been corrected from the value reported in ref 35. An important observation is that in spite of the differences in the scaling relations in Figure 2, the volcanoes are all very similar for a given temperature. In particular, the position of the maximum in terms of E_{CO} and E_O hardly changes from one structure to the next. One reason for this structure independence is related to the relevant energy scale. It may be seen in Figure 3 that the maxima are quite broad. The width of the maximum, defined as the width of the contour where the rate is 1 order of magnitude lower than the maximum, is on the order of 0.5 eV. This gives a certain insensitivity of the results to the details of the energetics.

For each structure we have shown in Figure 3, the position of the different metals is defined by their (E_{CO}, E_O) coordinate. It should be observed that the Au point moves closer to the maximum in the order (111) → (211) → (532) • • (M12), while the Pt and Pd points move away in the same order. This is made even clearer in Figure 4, where we show how the (E_{CO}, E_O) points for different structures wander on an average of the different volcanoes. Here we have also added the points (E_{CO}, E_O) for the Pt55 and Au55 clusters. They clearly adhere very well to the same trends.

There are two main conclusions from this analysis. First, the rate of CO oxidation (under the idealized conditions considered here) is a clear function of the local geometry. At the low temperature conditions considered in Figure 3, Au steps, kinks, and small particles have a higher calculated rate than the close-packed surface.[14] This is in good agreement with experimental observations.[31] We note here that additional effects due to supports may also contribute to the enhanced catalytic activity of small Au particles. The present calculations suggest that there is also an intrinsic size dependence relating to the availability of the most reactive structures involving low-coordinated Au atoms. For the other metals there is also a dependence on size. At low temperature it is quite weak for Cu and Ag, and stronger for Pd and Pt. For the latter two metals the trend is that the intrinsic activity decreases with decreasing particle size. At higher temperatures the CO oxidation rate is largest on these metals. The increased temperature shifts the top of the volcano to stronger adsorption energies, hence in the direction of the platinum metals. Such effects have been observed both experimentally and theoretically.[46−49] This effect on the reactivity is,

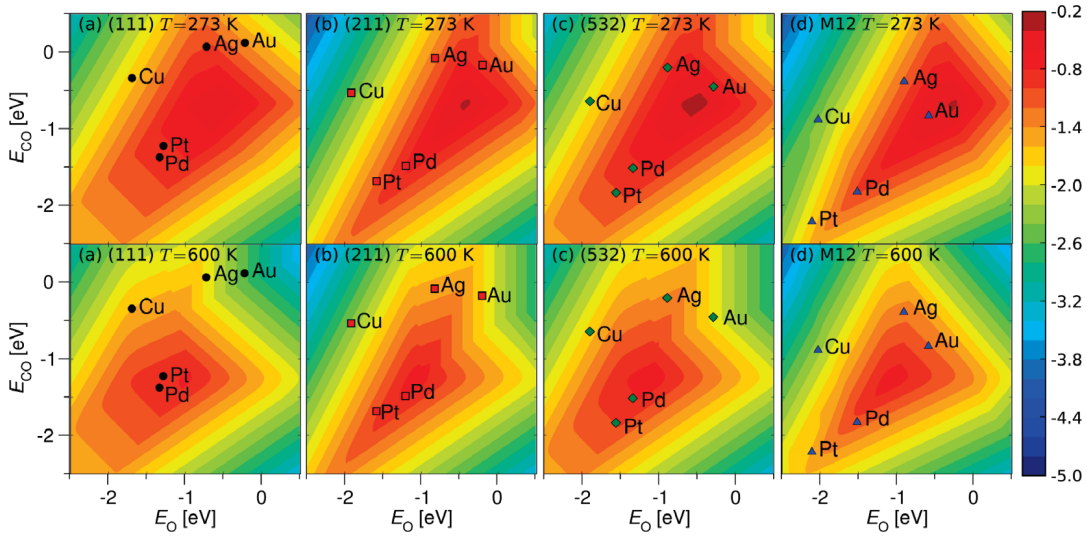

Figure 3. Contour plot of the Sabatier activity $A_S = k_B T \ln(r_S/k_B T h^{-1})$ in eV at (top) low temperature ($T = 273$, $p_{O_2} = 0.21$ bar, $p_{CO} = 0.01$ bar) and (bottom) high temperature ($T = 600$ K, $p_{O_2} = 0.33$ bar, $p_{CO} = 0.67$ bar), as a function of the CO and O adsorption energies on the (a) (111) surfaces (●, black), (b) (211) surfaces (■, red), (c) (532) surfaces (♦, green), and (d) M12 clusters (▲, blue). The values for several elemental metals are shown. The activity is calculated under typical experimental conditions for gold nanoparticles.

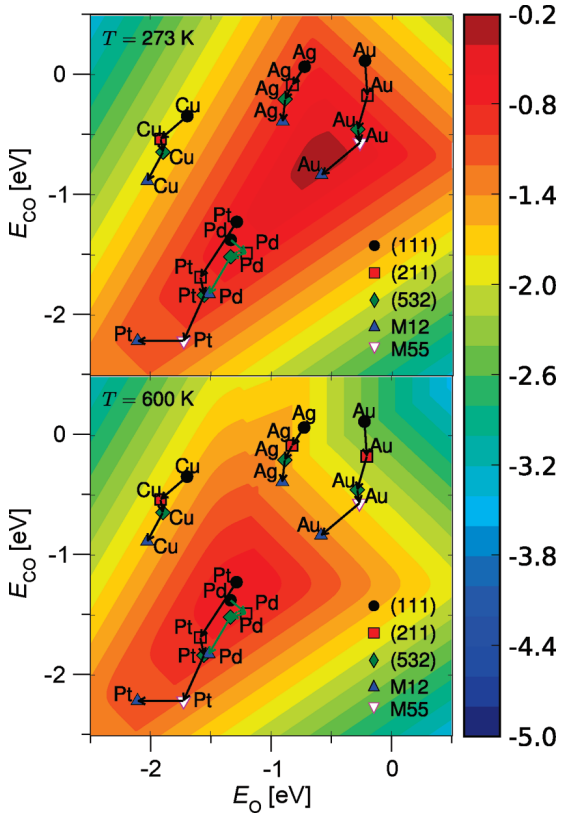

Figure 4. Contour plot of the "average" Sabatier activity $A_S = k_B T \ln(r_S/k_B T h^{-1})$ in eV at (top) low temperature ($T = 273$ K, $p_{O_2} = 0.21$ bar, $p_{CO} = 0.01$ bar) and (bottom) high temperature ($T = 600$ K, $p_{O_2} = 0.33$ bar, $p_{CO} = 0.67$ bar) from Figure 3 as a function of the CO and O adsorption energies on (111) surfaces (●, black), (211) surfaces (■, red), (532) surfaces (♦, green), M12-clusters (▲, blue), and M55-clusters (▽, magenta). The values for several elemental metals are shown. The activity is calculated under typical experimental conditions for gold nanoparticles.

however, quite weak. For platinum metals, the reaction rate for small nanoparticles may still be higher due to a significantly larger surface area per unit mass of catalyst. Additionally, mass and heat transfer could play an important role.

The other conclusion is that the main effect behind the structure variation is related to the strength of the adsorbate-

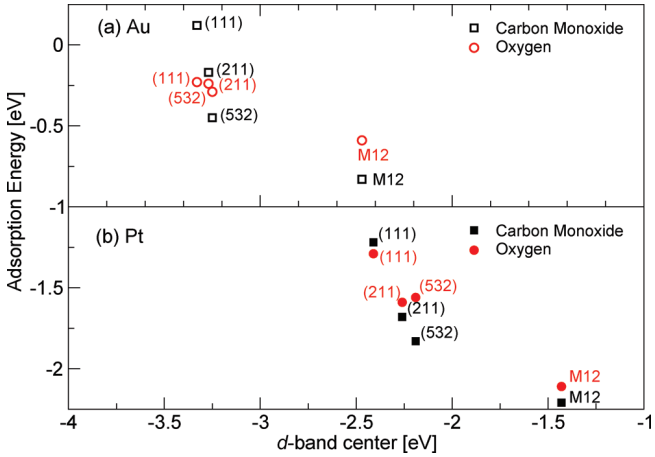

Figure 5. Adsorption energy E_{CO} and E_O versus d-band center for (111) surfaces, (211) surfaces, (532) surfaces, and M12 clusters of (a) Au (open black square, open red circle) and (b) Pt (solid black square, solid red circle).

metal bond at different structures. This effect is not geometrical, since the volcanoes for different structures are not very different. Rather it is connected to the variation in the bond strength of the different adsorbates as the structure is changed.

Electronic Effects. It was shown above that the structure-induced change in the intrinsic catalytic activity for CO oxidation on a number of metals is determined by the structure dependence in the adsorbate−surface interactions. We will now discuss the electronic origin of this effect.

In Figure 5 we show the variation in the adsorption energy of O and CO with the d-band center of the surface atoms. The d-band center is the average energy of the d states. Here it is defined as the density of states of the metal atoms to which CO and O bind, projected onto the d states of these metal atoms. The energy is taken relative to the Fermi energy. According to the d-band model[50] the strength of the adsorption bond should increase as the d states are shifted up in energy. This is also what is observed in Figure 5, for both the Pt and the Au clusters. The effect is stronger for Pt, since here the d states are higher up in energy and the bond strength is larger. The results illustrate the simple rule of thumb that the lower the metal coordination

number, the higher the d states are in energy, and the stronger they interact with adsorbates.

Conclusion

The main conclusions of the present computational study are the following. For the CO oxidation reaction over a range of metal surfaces, we have shown that the scaling relations between different adsorption energies and between activation energies and adsorption energies are structure dependent. By studying different close-packed, stepped and kinked surfaces as well as very small clusters, we have shown that the main difference in catalytic activity between different surface geometries is related to the "openness" of the surface. More precisely, the coordination number of metal atoms at active sites provides this structure dependence. By including the stepped and kinked surfaces, we have filled the gap between close packed surfaces and nanoparticles discussed in ref 35. Further, the activity is found to be a quasicontinuous function of the openness of the surface. We have also provided detailed evidence that this effect is electronic in nature: the low coordinated metal atoms that bind the reactants most strongly have the highest energy metal d states.

The present analysis has been explicitly aimed at understanding trends in reactivity for different metals and surface structures. As such, we have not included coverage effects, particularly the effects of high oxygen coverage and oxidation. Only the intrinsic metal activity has been studied.

The results of the present analysis may be used to understand structural effects in supported catalysts. Since the number of low coordinated metal sites is a strong function of particle size, the geometrical effects studied here will translate directly into particle size effects for supported catalysts. The finding that the catalytic activity of Au atoms increases strongly as the metal coordination number of the Au atoms decreases may provide part of the explanation for the unusually high catalytic activity of Au nanoparticles. Since the number of low-coordinated Au atoms should scale with particle size, d, as d^{-2} (edges) or d^{-3} (corners), our analysis explains why such scaling has been found experimentally.[18,46]

In supported catalysts one effect of the support is to determine the particle size for a given catalyst preparation and a given set of reaction conditions. As discussed above, this will determine the activity of the catalyst. The support may also affect the shape of the active metal catalysts. This can also change the number of most active sites. The support may also interact so strongly with the catalysts that the most reactive sites are covered by it. This can decrease the number of low-coordinated sites. Finally, the support may play an active role by activating some of the reactants or by providing new sites at the perimeter between the metal and the support. While all these effects may contribute, the present analysis has identified the intrinsic geometrical effect associated with the metal for the CO oxidation reaction. This effect will always be present, but may be further augmented by additional effects.

Acknowledgment. The Center for Sustainable and Green Chemistry is supported by the Danish National Research Foundation and the Center for Atomic-Scale Materials Design is supported by the Lundbeck Foundation. In addition we thank the Danish Research Council for the Technical Sciences and the NABIIT program for financial support, and the Danish Center for Scientific Computing for computer time.

References and Notes

(1) Chen, M. S.; Cai, Y.; Yan, Z.; Gath, K. K.; Axnanda, S.; Goodman, D. W. *Surf. Sci.* **2007**, *601*, 5326–5331.
(2) Nieuwenhuys, B. E. *Surf. Rev. Lett.* **1996**, *3*, 1869–1888.
(3) Engel, T.; Ertl, G. *Adv. Catal.* **1979**, *28*, 1.
(4) Campbell, C. T.; Ertl, G.; Kuipers, H.; Segner, J. *J. Chem. Phys.* **1980**, *73*, 5862.
(5) Goodman, D. W.; Peden, C. H. F. *J. Phys. Chem.* **1986**, *90*, 4839.
(6) Xu, J. Z.; Yates, J. T. *J. Chem. Phys.* **1993**, *99*, 725.
(7) Szanyi, J.; Goodman, D. W. *J. Chem. Phys.* **2001**, *114*, 6382.
(8) Valden, M.; Lai, X.; Goodman, D. W. *Science* **1998**, *281*, 1647–1649.
(9) Chen, M.; Goodman, D. *Science* **2004**, *306*, 252–255.
(10) Janssens, T. V. W.; Carlsson, A.; Puig-Molina, A.; Clausen, B. *J. Catal.* **2006**, *240*, 108–113.
(11) Xu, C.; Su, J.; Xu, X.; Liu, P.; Zhao, H.; Tian, F.; Ding, Y. *J. Am. Chem. Soc.* **2007**, *129*, 42–43.
(12) Xu, C.; Xu, X.; Su, J.; Ding, Y. *J. Catal.* **2007**, *252*, 243–248.
(13) Grisel, R.; Weststrate, K.-J.; Gluhoi, A.; Nieuwenhuys, B. E. *Gold Bull.* **2002**, *35*, 39–45.
(14) Mavrikakis, M.; Stoltze, P.; Nørskov, J. K. *Catal. Lett.* **2000**, *64*, 101–106.
(15) Reuter, K.; Scheffler, M. *Phys. Rev. B* **2002**, *65*, 035406.
(16) Liu, Z.-P.; Hu, P.; Alavi, A. *J. Am. Chem. Soc.* **2002**, *124*, 14770–14779.
(17) Lopez, N.; Janssens, T. V. W.; Clausen, B. S.; Xu, Y.; Mavrikakis, M.; Bligaard, T.; Nørskov, J. K. *J. Catal.* **2004**, *223*, 232–235.
(18) Janssens, T. V. W.; Clausen, B. S.; Hvolbæk, B.; Falsig, H.; Christensen, C. H.; Bligaard, T.; Nørskov, J. K. *Top. Catal.* **2007**, *44*, 15–26.
(19) Haruta, M.; Kobayashi, T.; Sano, H.; Yamada, N. *Chem. Lett.* **1987**, 405–408.
(20) Bond, G. C.; Thompson, D. T. *Catal. Rev.* **1999**, *41*, 319–388.
(21) Wickham, D. T.; Parker, D. H.; Kastanas, G. N.; Lazaga, M. A.; Koel, B. E. *Prepr. Am. Chem. Soc. Div. Pet. Chem* **1992**, *37*, 1034.
(22) Bond, G. C.; Thompson, D. T. *Gold Bull.* **2000**, *33*, 41–51.
(23) Bond, G. C.; Louis, C.; Thompson, D. T. *Catalysis by Gold*, 1st ed.; Imperial College Press: London, 2006.
(24) Ricci, D.; Bongiorno, A.; Pacchioni, G.; Landman, U. *Phys. Rev. Lett.* **2006**, *97*, 036106.
(25) van Bokhoven, J.; Louis, C.; Miller, J.; Tromp, M.; Safonova, O.; Glatzel, P. *Angew. Chem., Int. Ed.* **2006**, *45*, 4651–4654.
(26) Grunwaldt, J.-D.; Kiener, C. W.; Baiker, A. *J. Catal.* **1999**, *181*, 223–232.
(27) Shaikhutdinov, S.; Meyer, R.; Naschitzki, M.; Baumer, M.; Freund, H.-J. *Catal. Lett.* **2003**, *86*, 211–219.
(28) Lemire, C.; Meyer, R.; Shaikhutdinov, S.; Freund, H.-J. *Angew. Chem., Int. Ed.* **2004**, *43*, 118–121.
(29) Zanella, R.; Giorgio, S.; Shin, C.; Henry, C.; Louis, C. *J. Catal.* **2004**, *222*, 357–367.
(30) Deng, X.; Min, B.; Guloy, A.; Friend, C. *J. Am. Chem. Soc.* **2005**, *127*, 9267–9270.
(31) Walther, G.; Mowbray, D. J.; Jiang, T.; Jones, G.; Jensen, S.; Quaade, U.; Horch, S. *J. Catal.* **2008**, *280*, 86–92.
(32) Haruta, M. *Catal. Today* **1997**, *36*, 153–166.
(33) Sanchez, A.; Abbet, S.; Heiz, U.; Schneider, W.; Hakkinen, H.; Barnett, R.; Landman, U. *J. Phys. Chem. A.* **1999**, *103*, 9573–9578.
(34) Mills, G.; Gordon, M.; Metiu, H. *J. Chem. Phys.* **2003**, *118*, 4198–4205.
(35) Falsig, H.; Hvolbæk, B.; Kristensen, I. S.; Jiang, T.; Bligaard, T.; Christensen, C. H.; Nørskov, J. K. *Angew. Chem., Int. Ed.* **2008**, *47*, 4835–4839.
(36) Abrams, B. L.; Wilcoxon, J. P. *Crit. Rev. Solid State Mater. Sci.* **2005**, *30*, 153–182.
(37) Wilcoxon, J. P.; Abrams, B. L. *Chem. Soc. Rev.* **2006**, *35*, 1162–1194.
(38) Turner, M.; Golovko, V. B.; Vaughan, O. P. H.; Abdulkin, P.; Berenguer-Murcia, A.; Tikhov, M. S.; Johnson, B. F. G.; Lambert, R. M. *Nature* **2008**, *454*, 981.
(39) Hammer, B.; Hansen, L. B.; Nørskov, J. K. *Phys. Rev. B* **1999**, *59*, 7413–7421.
(40) Abild-Pedersen, F.; Andersson, M. P. *Surf. Sci.* **2007**, *601*, 1747–1753.
(41) Nørskov, J. K.; Rossmeisl, J.; Logadottir, A.; Lindqvist, L.; Kitchin, J. R.; Bligaard, T.; Jonsson, H. *J. Phys. Chem. B* **2004**, *108*, 17886–17892.
(42) Kurth, S.; Perdew, J. P.; Blaha, P. *Int. J. Quantum Chem.* **1999**, *75*, 889–909.
(43) Bligaard, T.; Nørskov, J. K.; Dahl, S.; Matthiesen, J.; Christensen, C. H.; Sehested, J. *J. Catal.* **2004**, *224*, 206–217.
(44) Atkins, P.; de Paula, J. *Physical Chemistry*, 8th ed.; Oxford University Press: Oxford, 2006.

(45) Nørskov, J. K.; Bligaard, T.; Logadottir, A.; Bahn, S.; Hansen, L. B.; Bollinger, M.; Bengaard, H.; Hammer, B.; Sljivancanin, Z.; Mavrikakis, M.; Xu, Y.; Dahl, S.; Jacobsen, C. J. H. *J. Catal.* **2002**, *209*, 275–278.

(46) Rashkeev, S. N.; Lupini, A. R.; Overbury, S. H.; Pennycook, S. J.; Pantelides, S. T. *Phys. Rev. B* **2007**, *76*, 035438.

(47) Becker, C.; Henry, C. R. *Surf. Sci.* **1996**, *352*−*354*, 457–462.

(48) Guerin, S.; Hayden, B. E.; Lee, C. E.; Mormiche, C.; Owen, J. R.; Russel, A. E. D.; Thomsett, B. T. *J. Comb. Chem.* **2004**, *6*, 149.

(49) Hayden, B. E.; Pletcher, D.; Suchsland, J.-P.; Williams, L. J. *Phys. Chem. Chem. Phys.* **2009**, *11*, 1564.

(50) Hammer, B.; Nørskov, J. K. *Surf. Sci.* **1995**, *343*, 211–220.

JP811185G

Tuning Au Surface Chemistry with Heterometals: A Computational Study

Bert D. Chandler[1,2,*], Frank Abild-Pederson[2], Tao Jiang[2], Jens K. Nørskov[2,*]

[1]*Department of Chemistry, Trinity University, 1 Trinity Place, San Antonio, TX, 78212 and* [2]*Center for Atomic Scale Materials Design, Department of Physics, Technical University of Denmark, DK-2800 Lyngby, Denmark*

RECEIVED DATE (automatically inserted by publisher); bert.chandler@trinity.edu

Gold nanoparticles (NPs) are now well established as important nanoscale building blocks and are being examined for a wide variety of applications in nanotechnology and nanomedicine.[1] Au NPs have also been shown to have outstanding catalytic activity and selectivity for several oxidation reactions.[2,3] Given the broad, general interest in Au NPs, there is a substantial need for fundamental studies to expand and tune Au chemistry for new applications.

One important yet largely unexplored means of tuning Au involves incorporating other metals into Au-based bimetallic NPs. However, most transition metals are insoluble in bulk gold at room temperature (Cu, Ag, and Pd are notable exceptions).[4] Although NPs can be prepared within bulk miscibility gaps,[5,6] substantial synthetic efforts are required to develop preparation methods for individual metal compositions. A number of important questions quickly arise: Is the potential for tuning Au chemistry large enough to justify the synthetic efforts? What compositions might have particularly interesting properties? How might heterometals addition affect Au NP chemistry?

Density functional theory (DFT) calculations on Au-M metal slabs may provide insight into these questions and guide the efforts of synthetic chemists. Accordingly, we investigated a series of Au(111) surfaces where the subsurface monolayer is replaced with another metal. The strong surface segregation energies calculated for Au-M binary mixtures indicate a strong thermodynamic driving force for moving Au to the surface of such materials,[7] which makes the calculated structures reasonable models for nanoscale materials. This approach probes electronic effects without inducing structural effects (lattice expansion/ compression, surface roughening) which can mask the nascent electronic influences of the hetrometal.[6,8] Accordingly, the top three layers of Au-M-Au(111) slabs, where M = 3d, 4d, or 5d transition metal, were allowed to relax in an energy minimization calculation (details in Supporting Information). Adsorption energies were then calculated for a variety of molecules interacting with the optimized slabs.

Figure 1A shows calculated adsorption energies for CO and O (the product of dissociative O_2 chemisorption) on the 3d and 5d sub surface monolayer slabs (data for 4d slabs are omitted for clarity). Reported energies are relative to that species on the pure Au(111) surface. The adsorption energies for CO and O show periodic trends based on the heterometals, with earlier transition metals inducing stronger adsorption on the Au surface. Further, 5d metals (filled symbols) more effectively increase the strength of the Au – adsorbate interaction than 3d metals (open symbols). These changes can be large, with Re and W increasing Au-O interaction by nearly 1 eV relative to pure Au. These results are in stark contrast to previous computational and experimental work on Pt-M-Pt(111) surfaces, where incorporating earlier transition metals results in weaker substrate binding.[9,10]

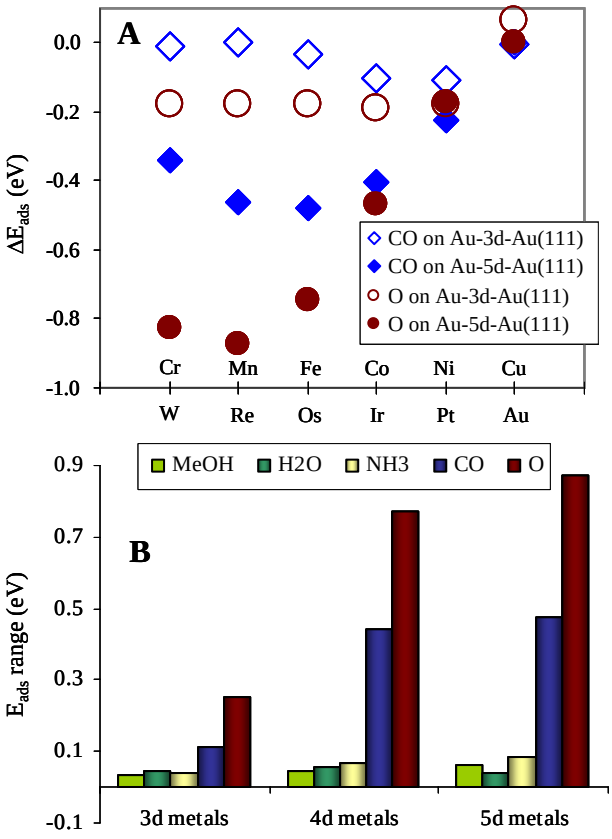

Figure 1. Adsorption data for Au-M-Au(111) slabs. (A) Adsorption energies for CO and O, relative to pure Au(111). (B) Adsorption energy ranges (sensitivity) for CH_3OH, H_2O, NH_3, CO, and O. The sensitivity represents the range in adsorption energies of each adsorbate for each series of heterometals in the 2nd layer. For water and methanol, no clear trend was observed, so the standard deviation is reported.

Figure 1A also shows that the 2nd layer metal impacts O adsorption more strongly than CO adsorption. We therefore investigated several other representative adsorbates. To facilitate comparing the adsorption energy sensitivity to the 2nd layer, the range of adsorption energies for each adsorbate and heterometal period are shown in Figure 1B.

The first clear trend is that the heterometal period affects the adsorption energies, with 5d > 4d > 3d metals. This is perhaps not surprising as elements of the same row have similar frontier orbital energies and sizes are therefore more likely to interact more strongly. The second trend of note is that electron withdrawing adsorbates (CO, O) show much greater sensitivity to the 2nd layer than does NH_3, a more traditional electron donating adsorbate / ligand. Adsorption by the common solvents water and methanol is essentially insensitive to the 2nd layer. It is also

noteworthy that the adsorption sensitivity does not correlate with adsorption strength: within a relatively small variance (± 0.08 eV), water, methanol, ammonia, and atomic O have roughly the same adsorption energy on Au(111) while CO adsorbs about 0.4 eV stronger.

A primary goal of this study was to evaluate the potential to tune gold chemistry through doping with other transition metals, and the results have important implications for Au NP chemists. First, the stronger binding of electron withdrawing adsorbates suggests it may be possible to alter the surface chemistry of Au by doping with appropriate heterometals. If appropriate nanostructures can be prepared, this may aid in imparting substrate specificity. Additionally, the calculations suggest that employing some colloid stabilizers with electron withdrawing properties may help to stabilize new bimetallic Au-based NPs.

The results also have obvious implications for CO oxidation catalysis. Recent computational studies have suggested that CO oxidation rates over a variety of metals can be described in terms of CO and O adsorption energies.[8,11] Figure 2, which has been adapted from reference 7 and expanded to include the current data, shows a plot of the DFT predicted CO oxidation activation barrier as a function of CO and O adsorption energies. Most of the bimetallic combinations increase the Sabatier activity of Au surfaces, and several approach the activity of the Au(532) surface. The various bimetallic combinations also cover a fairly large section of the volcano plot, suggesting that further tuning might be possible. Although real supported catalysts are almost certainly more complicated than the computational models, recent experimental studies support these general conclusions from these computational studies. For example, both supported Ni-Au NP catalysts[6] and Au/Ni(111) surfaces[12] show increased low temperature CO oxidation activity relative to pure Au.

The weak binding of O_2 to Au NPs[13] limits a number of potential applications, particularly in oxidations employing O_2 as the terminal oxidant.[2,3] Given that heterometal incorporation induces stronger O binding and faster Sabatier CO oxidation rates, other Au catalyzed oxidations may be similarly affected. Further, since O_2 is more sensitive to the 2nd layer than other adsorbates, it may be possible to increase O_2 binding relative to oxidizable substrates and solvents, potentially reducing unwanted side reactions.

In summary, DFT calculations on bimetallic Au-M-Au(111) slabs suggest that there is a large potential for tuning Au chemistry by incorporating other transition metals. Adsorption by electron withdrawing substrates is sensitive to the heterometals, with more electron rich earlier transition metals giving rise to stronger adsorption of O and CO on the Au surface. This trend is in stark contrast to Pt based alloys,[9,10] which show weaker adsorption with heterometals incorporation.[14] The results indicate that there may be substantial opportunities to tune Au based oxidation catalysts. Further, the results may provide some guidance to synthetic chemists as they suggest that moderately electron withdrawing stabilizers may assist in preparing new Au-based bimetallic NPs.

Acknowledgement The authors gratefully acknowledge the Robert A. Welch Foundation (Grant number W-1552) and the U.S. National Science Foundation (Grant number CHE-0449549) for financial support of our work. BDC thanks the donors of the Petroleum Research Fund for a UFS grant to support academic leave at the Center for Atomic-Scale Materials Design, which is supported by the Lundbeck Foundation. The authors also thank the Danish Center for Scientific Computing for computer time.

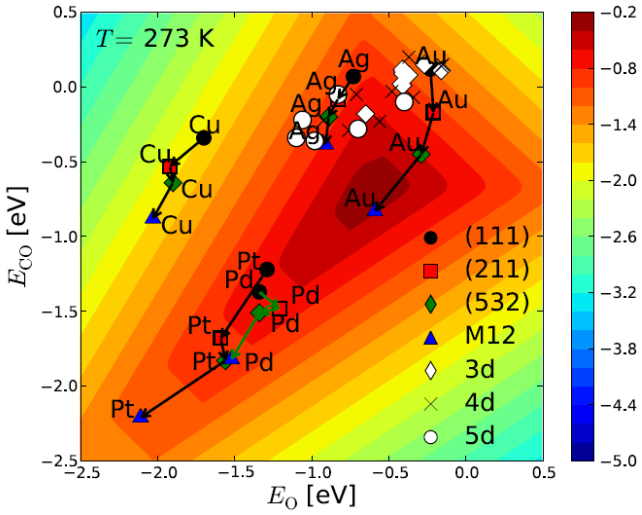

Figure 2. Contour plot of the Sabatier activity in eV as a function of CO and O adsorption energies at T = 273, P_{O2} = 0.21 bar, P_{CO} = 0.01 bar. Activities for several pure metals (Au, Ag, Cu, Pt, Pd), various surfaces ((111), (211), (532)), and a 12-atom cluster (M12) are presented in filled symbols. Activities for the Au-M-Au(111) slabs are presented with open symbols and show the calculated changes in CO oxidation activity relative to the pure Au(111). Data for the contour plot were extracted from reference 8.

References

(1) Boisselier, E.; Astruc, D. *Chemical Society Reviews* **2009**, *38*, 1759-1782.
(2) Hashmi, S. K.; Hutchings Graham, J. *Angewandte Chemie (International ed. in English)* **2006**, *45*, 7896-7936.
(3) Corma, A.; Garcia, H. *Chemical Society Reviews* **2008**, *37*, 2096-2126.
(4) Ferro, R.; Saccone, A.; Maccio, D.; Delfino, S. *Gold Bulletin* **2003**, *36*, 39-50.
(5) Lang, H.; Maldonado, S.; Stevenson, K. J.; Chandler, B. D. *J. Am. Chem. Soc.* **2004**, *126*, 12949-12956.
(6) Chandler, B. D.; Long, C. G.; Gilbertson, J. D.; Pursell, C. J.; Vijayaraghavan, G.; Stevenson, K. J. *J. Phys Chem C.*, submitted.
(7) Ruban, A. V.; Skriver, H. L.; Norskov, J. K. *Physical Review B: Condensed Matter and Materials Physics* **1999**, *59*, 15990-16000.
(8) Jiang, T.; Mowbray, D. J.; Dobrin, S.; Falsig, H.; Hvolbaek, B.; Bligaard, T.; Noerskov, J. K. *Journal of Physical Chemistry C* **2009**, *113*, 10548-10553.
(9) Kitchin, J. R.; Norskov, J. K.; Barteau, M. A.; Chen, J. G. *Journal of Chemical Physics* **2004**, *120*, 10240-10246.
(10) Chen, J. G.; Menning, C. A.; Zellner, M. B. *Surface Science Reports* **2008**, *63*, 201-254.
(11) Falsig, H.; Hvolboek, B.; Kristensen, I. S.; Jiang, T.; Bligaard, T.; Christensen, C. H.; Noerskov, J. K. *Angewandte Chemie, International Edition* **2008**, *47*, 4835-4839.
(12) Lahr, D. L.; Ceyer, S. T. *Journal of the American Chemical Society* **2006**, *128*, 1800-1801.
(13) Long, C. G.; Gilbertson, J. D.; Vijayaraghavan, G.; Stevenson, K. J.; Pursell, C. J.; Chandler, B. D. *Journal of the American Chemical Society* **2008**, *130*, 10103-10115.
(14) The details of the differences between Au and Pt alloys will be addressed in a forthcoming manuscript.

Supporting Information Available: Computational Methods. This information is available free of charge via the internet at http://pubs.acs.org.

TOC Graphic

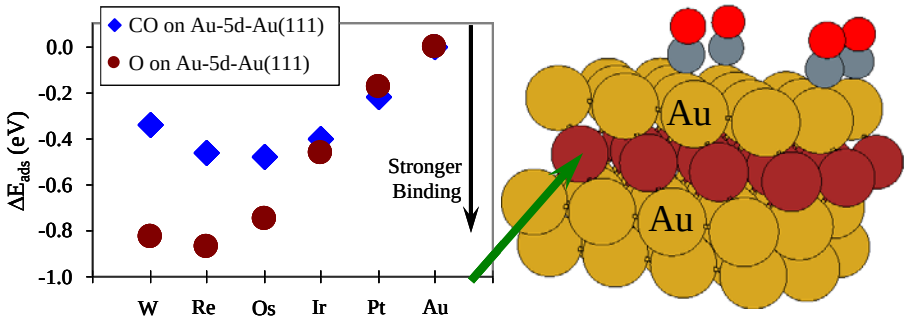
CO on Au-5d-Au(111)
O on Au-5d-Au(111)
0.0
-0.2
-0.4
-0.6
-0.8
-1.0
ΔE_ads (eV)
W
Re
Os
Ir
Pt
Au
Stronger
Binding
Au
Au